

Report No. UT-14.09

## **SEISMIC EVALUATION OF GROUTED SPLICE SLEEVE CONNECTIONS FOR PRECAST RC BRIDGE PIERS IN ABC**

### **Prepared For:**

Utah Department of Transportation  
Research Division

### **Submitted By:**

University of Utah  
Department of Civil and Environmental  
Engineering

### **Authored By:**

Chris P. Pantelides  
M.J. Ameli  
Joel E. Parks  
Dylan N. Brown

**Final Report  
October 2014**

## **DISCLAIMER**

The authors alone are responsible for the preparation and accuracy of the information, data, analysis, discussions, recommendations, and conclusions presented herein. The contents do not necessarily reflect the views, opinions, endorsements, or policies of the Utah Department of Transportation or the U.S. Department of Transportation. The Utah Department of Transportation makes no representation or warranty of any kind, and assumes no liability therefore.

## **ACKNOWLEDGMENTS**

The authors acknowledge the financial support provided by the Utah Department of Transportation, the New York State Department of Transportation and the Texas Department of Transportation through the Pooled Fund Study Program. The authors also acknowledge the financial support provided through the Mountain Plains Consortium through project MPC392.

The authors acknowledge the Utah Department of Transportation (UDOT) for funding this research, and Carmen Swanwick and Joshua Sletten who served on UDOT's Technical Advisory Committee for helping to guide the research. In addition they appreciate the advice of Harry White, New York State Department of Transportation.

The authors would also like to acknowledge the assistance of Mark Bryant, Zant Doty, Trevor Nye, and Wade Stinson of the University of Utah for their assistance in the experiments.

The following companies made in-kind donations for this project and the authors are grateful to them: Splice Sleeve North America, Inc., ERICO, and Hanson Structural Precast.

## TECHNICAL REPORT ABSTRACT

1. Report No. UT- 14.09		2. Government Accession No. N/A		3. Recipient's Catalog No. N/A	
4. Title and Subtitle SEISMIC EVALUATION OF GROUTED SPLICE SLEEVE CONNECTIONS FOR PRECAST RC BRIDGE PIERS IN ABC				5. Report Date June 2014	
				6. Performing Organization Code	
7. Author(s) Chris P. Pantelides, M. J. Ameli, Joel E. Parks, and Dylan N. Brown				8. Performing Organization Report No.	
9. Performing Organization Name and Address University of Utah Department of Civil and Environmental Engineering 110 S. Central Campus Dr., Room 2115 Salt Lake City, Utah 84112				10. Work Unit No. 5H072048	
				11. Contract or Grant No. 12-8775	
12. Sponsoring Agency Name and Address Utah Department of Transportation 4501 South 2700 West P.O. Box 148410 Salt Lake City, UT 84114-8410				13. Type of Report & Period Covered FINAL	
				14. Sponsoring Agency Code UT 11.502	
15. Supplementary Notes Pooled Fund Study prepared in cooperation with the Utah Department of Transportation, New York State Department of Transportation and Texas Department of Transportation.					
16. Abstract Connections between precast concrete elements must be able to withstand significant stresses and deformations in earthquakes. The Grouted Splice Sleeve (GSS) connection is being considered for connecting such elements in Accelerated Bridge Construction (ABC). There is limited data for use of this connection in bridges located in moderate-to-high seismic regions. This report describes a research program conducted to evaluate the GSS connections experimentally. Cyclic quasi-static loading was applied to four column-to-footing and four column-to-cap beam half-scale test specimens. The column-to-footing connections incorporated one type of GSS where the bars were grouted at both ends (GGSS); the column-to-cap beam connections used a different GSS type where one bar was threaded into one end and the other bar was grouted into the opposite end (FGSS). Experimental results showed that the performance of all test specimens was satisfactory and the connections were viable. Improved seismic response was observed when the sleeves were located inside the footing and the cap beam rather than the corresponding column end. A debonded rebar zone was considered to further improve the displacement ductility capacity of the components. This technique was found to be highly effective for the column-to-footing connections.					
17. Key Words ABC, bridges, connections, cyclic performance, earthquakes, grouted splice sleeves, joints,			18. Distribution Statement Not restricted. Available through: UDOT Research Division 4501 South 2700 West P.O. Box 148410 Salt Lake City, UT 84114-8410 <a href="http://www.udot.utah.gov/go/research">www.udot.utah.gov/go/research</a>		23. Registrant's Seal N/A
19. Security Classification (of this report)  Unclassified	20. Security Classification (of this page)  Unclassified	21. No. of Pages  168	22. Price  N/A		

## TABLE OF CONTENTS

LIST OF TABLES .....	v
LIST OF FIGURES .....	vi
LIST OF ACRONYMS .....	xi
EXECUTIVE SUMMARY .....	1
1.0 INTRODUCTION .....	2
1.1 Previous Research.....	4
1.2 Research Objectives.....	9
1.3 Outline of Report .....	12
2.0 DESIGN AND CONSTRUCTION OF TEST SPECIMENS.....	13
2.1 Design of Test Specimens.....	13
2.1.1 AASHTO-Seismic Provisions .....	15
2.2 Column-to-Footing Connections .....	20
2.2.1 GGSS-1 .....	21
2.2.2 GGSS-2 .....	26
2.2.3 GGSS-3 .....	31
2.2.4 GGSS-CIP.....	37
2.3 Column-to-Cap Beam Connections .....	42
2.3.1 FGSS-1.....	42
2.3.2 FGSS-2.....	48
2.3.3 FGSS-3.....	53
2.3.4 FGSS-CIP .....	58
3.0 TEST PROCEDURE .....	62
3.1 Instrumentation .....	62
3.1.1 Strain Gauges .....	62
3.1.2 String Potentiometers.....	66
3.1.3 Linear Variable Differential Transformers .....	67
3.2 Test Setup .....	70
3.3 Displacement History .....	73
4.0 TEST RESULTS.....	74

4.1 Analysis of the Response .....	75
4.1.1 Experimental Observations and Damage States .....	75
4.1.2 Displacement Ductility Capacity and Plastic Rotation Capacity.....	75
4.1.3 Cumulative Energy Dissipation .....	76
4.1.4 Column Curvature Profile.....	76
4.2 Response of Column-to-Footing Connections.....	78
4.2.1 GGSS-1 Results .....	78
4.2.2 GGSS-2 Results .....	84
4.2.3 GGSS-3 Results .....	91
4.2.4 GGSS-CIP Results .....	99
4.2.5 Comparative Study of Column-to-Footing Connections .....	106
4.3 Response of Column-to-Cap beam Connections .....	112
4.3.1 FGSS-1 Results .....	112
4.3.2 FGSS-2 Results .....	117
4.3.3 FGSS-3 Results .....	124
4.3.4 FGSS-CIP Results.....	133
4.3.5 Comparative Study of Column-to-Cap Beam Connections.....	140
5.0 CONCLUSIONS.....	146
5.1 Summary.....	146
5.2 Findings .....	147
5.2.1 Column-to-Footing Connections .....	147
5.2.2 Column-to-Cap Beam Connections .....	149
5.3 Future Research .....	151
6.0 DESIGN RECOMMENDATIONS .....	152
REFERENCES .....	154

**LIST OF TABLES**

Table 1-1. Test matrix.....11

Table 2-1. AASHTO-Seismic provisions pertinent to design and datsailing of test specimens....17

Table 4-1. Rebar properties for column-to-footing test specimens. ....106

Table 4-2. Concrete and grout properties for column-to-footing test specimens. ....107

Table 4-3. Effective yield properties and displacement ductility for column-to-footing test  
specimens.....107

Table 4-4. Rebar properties for column-to-cap beam test specimens.....140

Table 4-5. Concrete and grout properties for column-to-cap beam test specimens.....141

Table 4-6. Effective yield properties and displacement ductility for column-to-cap beam test  
specimens.....141

## LIST OF FIGURES

Figure 1-1. Typical application of a bar coupler [3].	4
Figure 1-2. Two types of Coupler used in the research [7].	6
Figure 1-3. ISR method for precast reinforced concrete members [13].	7
Figure 1-4. Damage state for two test specimens at failure [15].	8
Figure 1-5. Two types of GSS incorporated in this research.	9
Figure 1-6. FGSS vs GGSS connections.	10
Figure 1-7. Configuration of test specimen alternatives.	11
Figure 2-1. Prototype bridge with highlighted portions representing specimen design.	14
Figure 2-2. Preliminary pushover analysis on monolithic test specimen (prediction).	15
Figure 2-3. General design and detailing of joint region for both categories of specimens.	16
Figure 2-4. GGSS-1 precast components under construction.	21
Figure 2-5. GGSS-1 specimen details and rebar cages.	23
Figure 2-6. GGSS-1 precast components inside concrete forms.	24
Figure 2-7. Grouting operation for GGSS-1.	25
Figure 2-8. GGSS-1 in the final position.	25
Figure 2-9. GGSS-2 precast components under construction.	26
Figure 2-10. GGSS-2 precast footing core rebar cage.	27
Figure 2-11. Details of GGSS-2.	28
Figure 2-12. GGSS-2 rebar cages.	29
Figure 2-13. GGSS-2 precast components inside concrete forms.	29
Figure 2-14. Grouting operation for GGSS-2.	30
Figure 2-15. GGSS-2 in final position.	31
Figure 2-16. Debonded region of the dowel bars for GGSS-3.	32
Figure 2-17. GGSS-3 precast components under construction.	33
Figure 2-18. Details of GGSS-3.	34
Figure 2-19. GGSS-3 rebar cages.	35
Figure 2-20. GGSS-3 precast components inside concrete forms.	36
Figure 2-21. Grouting operation for GGSS-3.	36
Figure 2-22. GGSS-3 in final position.	37
Figure 2-23. Construction of GGSS-CIP.	38

Figure 2-24. GGSS-CIP specimen details and rebar cage. ....	40
Figure 2-25. GGSS-CIP rebar cage inside concrete form.....	41
Figure 2-26. GGSS-CIP in final position.....	41
Figure 2-27. FGSS-1 precast components under construction. ....	43
Figure 2-28. Details of FGSS-1. ....	43
Figure 2-29. FGSS-1 rebar cage. ....	44
Figure 2-30. FGSS-1 precast components inside concrete forms.....	45
Figure 2-31. Grouting operation for FGSS-1.....	46
Figure 2-32. FGSS-1 (far behind) in final position.....	47
Figure 2-33. FGSS-2 precast components under construction. ....	49
Figure 2-34. Details of FGSS-2. ....	49
Figure 2-35. FGSS-2 rebar cages.....	50
Figure 2-36. FGSS-2 precast components inside concrete forms.....	51
Figure 2-37. Grouting operation for FGSS-2.....	52
Figure 2-38. FGSS-2 in final position.....	52
Figure 2-39. Debonded region of the dowel bars for FGSS-3.....	53
Figure 2-40. FGSS-3 precast components under construction. ....	55
Figure 2-41. Details of FGSS-3 ....	55
Figure 2-42. FGSS-3 rebar cages.....	56
Figure 2-43. FGSS-3 precast components inside concrete forms.....	56
Figure 2-44. FGSS-3 precast column before grouting operation.....	57
Figure 2-45. FGSS-3 in the final position.....	57
Figure 2-46. FGSS-CIP joint area.....	59
Figure 2-47. FGSS-CIP specimen detail and rebar cage. ....	60
Figure 2-48. FGSS-CIP rebar cage inside concrete form. ....	61
Figure 2-49. FGSS-CIP in final position. ....	61
Figure 3-1. Strain gauge layout for GGSS-3. ....	64
Figure 3-2. Strain gauges on GGSS-3.....	65
Figure 3-3. Strain gauges on FGSS-3. ....	65
Figure 3-4. String potentiometer on west side of specimen GGSS-3.....	66
Figure 3-5. LVDT configuration for column-to-footing connections .....	67

Figure 3-6. LVDTs for curvature analysis.....	68
Figure 3-7. Experimental configuration of column-to-footing test specimens.....	71
Figure 3-8. Experimental configuration of column-to-cap beam test specimens. ....	72
Figure 3-9. Displacement history.....	73
Figure 4-1. Curvature parameters for one curvature segment. ....	77
Figure 4-2. Hysteresis response of GGSS-1 with damage states.....	78
Figure 4-3. GGSS-1 visual observations. ....	80
Figure 4-4. Average backbone curve and displacement ductility for GGSS-1.....	81
Figure 4-5. Plastic rotation capacity for GGSS-1. ....	82
Figure 4-6. Energy dissipation capacity of GGSS-1.....	83
Figure 4-7. Normalized curvature distribution for GGSS-1. ....	83
Figure 4-8. Hysteresis response of GGSS-2 with damage states.....	84
Figure 4-9. GGSS-2 at maximum displacement during the 3% drift ratio—Largest crack. ....	85
Figure 4-10. GGSS-2 visual observations. ....	87
Figure 4-11. Average backbone curve and displacement ductility of GGSS-2.....	88
Figure 4-12. Plastic rotation capacity for GGSS-2. ....	89
Figure 4-13. Energy dissipation capacity of GGSS-2.....	90
Figure 4-14. Normalized curvature distribution for GGSS-2. ....	91
Figure 4-15. Hysteresis response of GGSS-3 with damage states.....	92
Figure 4-16. GGSS-3 visual observations. ....	94
Figure 4-17. GGSS-3 footing dowel became visible at the 7% drift ratio.....	95
Figure 4-18. Average backbone curve and displacement ductility of GGSS-3.....	96
Figure 4-19. Plastic rotation capacity for GGSS-3. ....	97
Figure 4-20. Energy dissipation capacity of GGSS-3.....	98
Figure 4-21. Normalized curvature distribution for GGSS-3. ....	99
Figure 4-22. Hysteresis response of GGSS-CIP with damage states.....	100
Figure 4-23. GGSS-CIP visual observations. ....	102
Figure 4-24. Average backbone curve and displacement ductility of GGSS-CIP.....	103
Figure 4-25. Plastic rotation capacity for GGSS-CIP.....	104
Figure 4-26. Energy dissipation capacity for GGSS-CIP. ....	105
Figure 4-27. Normalized curvature distribution for GGSS-CIP. ....	106

Figure 4-28. Force-displacement response of column-to-footing test specimens. ....	108
Figure 4-29. Stiffness degradation for column-to-footing test specimens.....	110
Figure 4-30. Cumulative hysteretic energy for column-to-footing test specimens. ....	111
Figure 4-31. Equivalent viscous damping for column-to-footing test specimens. ....	111
Figure 4-32. Hysteresis response of FGSS-1 with damage states. ....	113
Figure 4-33. FGSS-1 visual observations. ....	114
Figure 4-34. Average backbone curve and displacement ductility for FGSS-1. ....	115
Figure 4-35. Plastic rotation capacity for FGSS-1.....	115
Figure 4-36. Energy dissipation capacity of FGSS-1. ....	116
Figure 4-37. Normalized curvature distribution for FGSS-1.....	117
Figure 4-38. Hysteresis response of FGSS-2 with damage states. ....	118
Figure 4-39. FGSS-2 visual observations. ....	120
Figure 4-40. Average backbone curve and displacement ductility of FGSS-2.....	121
Figure 4-41. Plastic rotation capacity for FGSS-2.....	121
Figure 4-42. Energy dissipation capacity of FGSS-2. ....	123
Figure 4-43. Normalized curvature distribution for FGSS-2.....	123
Figure 4-44. Pre-test condition of FGSS-3. ....	124
Figure 4-45. Hysteresis response of FGSS-3 with damage states. ....	125
Figure 4-46. Damage state for FGSS-3 at 4% drift ratio. ....	126
Figure 4-47. FGSS-3 cap beam dowel pull-out at 8% drift ratio.....	128
Figure 4-48. Damage state for FGSS-3 at end of test: cracks and spalling, permanent gap.....	129
Figure 4-49. Average backbone curve and displacement ductility of FGSS-3.....	130
Figure 4-50. Plastic rotation capacity for FGSS-3.....	130
Figure 4-51. Energy dissipation capacity for FGSS-3.....	131
Figure 4-52. Normalized curvature distribution for FGSS-3.....	132
Figure 4-53. Hysteresis response of FGSS-CIP with damage states. ....	133
Figure 4-54. Damage state for FGSS-CIP at 3% drift ratio.....	134
Figure 4-55. FGSS-CIP at peak displacement during 4% drift ratio; largest three cracks. ....	135
Figure 4-56. Damage state for FGSS-CIP at 6% drift ratio: cracks and spalling, yield penetration.	136
Figure 4-57. Damage state for FGSS-CIP at end of test: cracks and spalling, rebar buckling and fracture. ....	137

Figure 4-58. Average backbone curve and displacement ductility of FGSS-CIP. ....	138
Figure 4-59. Plastic rotation capacity for FGSS-CIP.....	138
Figure 4-60. Energy dissipation capacity for FGSS-CIP.....	139
Figure 4-61. Normalized curvature distribution for FGSS-CIP.....	140
Figure 4-62. Force-displacement response of column-to-cap beam test specimens.....	142
Figure 4-63. Stiffness degradation for column-to-cap beam test specimens. ....	143
Figure 4-64. Cumulative hysteretic energy for column-to-cap beam test specimens.....	144
Figure 4-65. Equivalent viscous damping for column-to-cap beam test specimens.....	145

## **LIST OF ACRONYMS**

AASHTO	American Association of State Highway and Transportation Officials
ACI	American Concrete Institute
GSS	Grouted Splice Sleeve
LVDT	Linear Variable Differential Transformer
SDC	Seismic Design Category
SDC	Seismic Design Criteria
UDOT	Utah Department of Transportation

## **EXECUTIVE SUMMARY**

In recent years, Accelerated Bridge Construction (ABC) has gained attention within regions of moderate-to-high seismicity. Prefabrication of bridge structural components is a highly effective method in this process and is one of the ABC methods under the category of Prefabricated Bridge Elements and Systems (PBES) promoted by the Federal Highway Administration. Connections between such precast components play an important part in the overall seismic performance of bridges. This report describes a research study developed to investigate a potential ABC connection for joints of bridges located in high-seismic regions. This connection type, referred to as Grouted Splice Sleeve (GSS) Connection, is studied for column-to-footing and column-to-cap beam connections. Half-scale test models were designed and constructed based on typical reinforced concrete bridges in the State of Utah. Cyclic quasi-static loading was applied to four column-to-footing and four column-to-cap beam half-scale test specimens. The column-to-footing connections incorporated one type of GSS where the bars were grouted at both ends (GGSS); the column-to-cap beam connections used a different GSS type where one bar was threaded into one end and the other bar was grouted into the opposite end (FGSS). Experimental results showed that the performance of all test specimens was satisfactory and the connections were viable. The report compares the performance of the precast connections to monolithic joints for both the GGSS and FGSS categories. Improved seismic response was observed when the sleeves were located inside the footing and the cap beam rather than the corresponding column end. A debonded rebar zone was considered to further improve the displacement ductility capacity of the components. This technique was found to be highly effective for the column-to-footing connections. The report concludes with design recommendations.

## **1.0 INTRODUCTION**

Accelerated Bridge Construction (ABC) refers to a bridge construction type that incorporates innovative techniques, methodologies, and materials to efficiently reduce the construction time and traffic disruption. It also provides a higher level of work-zone safety for workers and commuters, and improves environmental-friendly activities. Prefabrication of bridge structural components is a highly effective method in this process and is one of the ABC methods under the category of Prefabricated Bridge Elements and Systems (PBES) promoted by the Federal Highway Administration.

Many bridges have been built or rehabilitated following ABC standards. Local examples include the I-15 CORE Provo Center Street Interchange, the Riverdale Road over I-84 Bridge, and the I-15 South Layton Interchange. Precast concrete deck panels, substructures, and superstructures have been frequently utilized as effective ABC methods. Connections between such precast elements are among the most critical components in the whole structure. Researchers are in the process of investigating the suitability of various connection configurations, especially in moderate-to-high seismic regions. These connections, not only have to conform to ABC standards in terms of the overall construction delivery time, but must also resist high levels of earthquake-induced deformations and stresses. Lateral load capacity, ductility levels, and reparability are three significant acceptance criteria for any connection considered in earthquake-prone regions.

The *Grouted Duct Connection* has been introduced as a viable ABC technique for both column-to-footing and column-to-cap beam connections [1, 2]. In this method corrugated steel ducts are accommodated in a footing or cap beam, and column reinforcement dowels are inserted and grouted inside the ducts.

The *Pocket Connection* was studied and implemented to connect bridge columns to cap beams [3]. It is constructed by placing a circular corrugated steel duct inside the cap beam. Projected column bars are inserted into the pocket that is filled with concrete at the end.

The *Socket Connection* is another type of ABC connection that has recently become more popular. A socket foundation was studied at the University of Washington and later used to

connect columns to spread footings in a bridge constructed in the State of Washington over I-5 [4]. In this method, the bottom end of the precast column is roughened and embedded in the footing which is commonly cast-in-place, after which, the footing concrete is cast around the column base.

Prestressing has been incorporated in many bridge columns to improve their seismic performance by providing self-centering characteristics. This connection type is identified as a *Hybrid Connection* because both prestressing and mild steel are utilized. Research studies show that residual displacements and overall damage are reduced compared to non-prestressed connections [5].

Innovative techniques have been studied in order to achieve superior performance during a seismic event. One of the most recent studies investigated the application of *Shape Memory Alloys* (SMA) in the connection of bridge sub-assemblies [6]. Headed SMA bars were used in a bridge column-to-footing connection together with a grouted duct connection that was incorporated in the footing to facilitate the application of such a system in ABC.

The *Grouted Splice Sleeve Connection* and other types of rebar splicing devices are considered as another effective connection type for ABC. Such connections have been frequently used, specifically in non-seismic regions, because they offer ease of construction and speed up construction. In this connection type each individual rebar in connecting precast components is spliced by means of a mechanical coupler which is readily located within one of the components, normally the precast component that is built at the precast plant. The response of such connections to a seismic event was recently studied to investigate the performance in high seismic areas [6, 7]. Among all ABC connections, Grouted Splice Sleeve Connections require more profound investigation and research as there have been very few comprehensive experimental or analytical studies in the United States, especially with detailing typical of bridge structural elements. There is a need for more technical documentation on the performance of the Grouted Splice Sleeve Connections before they can be used for bridges in moderate-to-high seismic region using ABC.

## 1.1 Previous Research

The evaluation of several ABC connections in moderate-to-high seismic regions was conducted and summarized in NCHRP Report 698 [3]. Verified connection types include bar couplers, grouted ducts, pocket connections, socket connections, hybrid connections, integral connections, and emerging technologies, such as shape memory alloys and elastomeric bearings. These connections were either utilized in actual practice, or were being developed in research studies. The aforementioned ABC connections were then ranked according to technology readiness, performance, and time savings potential, relative to cast-in-place construction for the same connection type. One of the significant outcomes of this synthesis study was the prioritization of more research studies essential for each connection type in order to fully understand their behavior under seismic actions.

A bar coupler was defined as a mechanical coupler used to splice two bars together. This synthesis report addressed several types of couplers, such as threaded sleeves, headed bars with separate sleeves, external clamping screws, and grouted sleeves. Application of the grouted sleeve, which is typically used in bridges, provides the benefit of larger tolerances in comparison with other types of couplers, as shown in **Figure 1-1** [3].

Despite extensive use of such connections in regions of moderate seismicity, in-depth knowledge of their inelastic behavior has not been achieved, necessitating more research and experimental verification. The need for further studies discussed in NCHRP Report 698 was

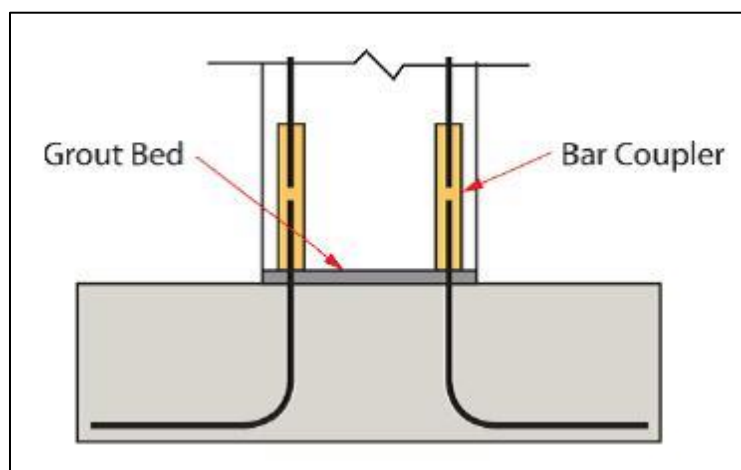


Figure 1-1. Typical application of a bar coupler [3].

based on the urgency level of the unknown aspects of this connection type. First priority was given to the cyclic performance of the couplers with the bars in their plastic range of stress, and strain distribution for the bars being spliced; second priority studies included the investigation of the strength details, such as magnitude of stress that each bar can develop, together with verification of bar coupler placement. The latter refers to the proper location of the coupler (e.g., in the column or footing), so it does not affect the overall response to earthquake loads, but could still be a constructible detail. The effect of surrounding concrete and level of provided confinement on the coupler is the third category of priorities, as the last necessary study to be conducted on this type of ABC connection.

As part of a comprehensive research study on the seismic performance of next generation bridge components for ABC, the University of Nevada, Reno, has been investigating the behavior of four column-to-footing connections under cyclic lateral loading, utilizing two different proprietary couplers [7]. The research program also considered a cast-in-place specimen as the control test. NMB Splice Sleeves and HRC 500 Up-Set Headed Couplers were used to connect the longitudinal reinforcement in the column and footing as shown in **Figure 1-2**. For each coupler, two test specimens were constructed and tested under cyclic quasi-static loading. A precast pedestal was incorporated in one specimen for each category to reduce the moment demand over the coupler region. Considering the hysteretic behavior of all specimens, it was noted that the HC connection showed a similar response to the cast-in-place detail and withstood a relatively large amount of drift. In spite of the ease of construction achieved by incorporating the grouted couplers, their ductility capacity was found to be less than both the cast-in-place and the HC connection specimens. Comparing the results of the cyclic tests, it was noted that all specimens exhibited similar performance in terms of ultimate load capacity and energy dissipation, but the ductility capacity was different. Tazarv et al. (2014) described a remedial procedure to improve the ductility capacity of the columns with the grouted couplers embedded in the pedestal. The footing dowel bars were debonded within the pedestal to allow for a better spread of plasticity along the bars and ultimately postpone the rebar fracture.

Haber et al. (2013) described a package of air tests on the two aforementioned splicing systems [8]. These tests were conducted to obtain results necessary for numerical modeling focusing on the coupler region. To study the stress-strain behavior of that region, strain gages

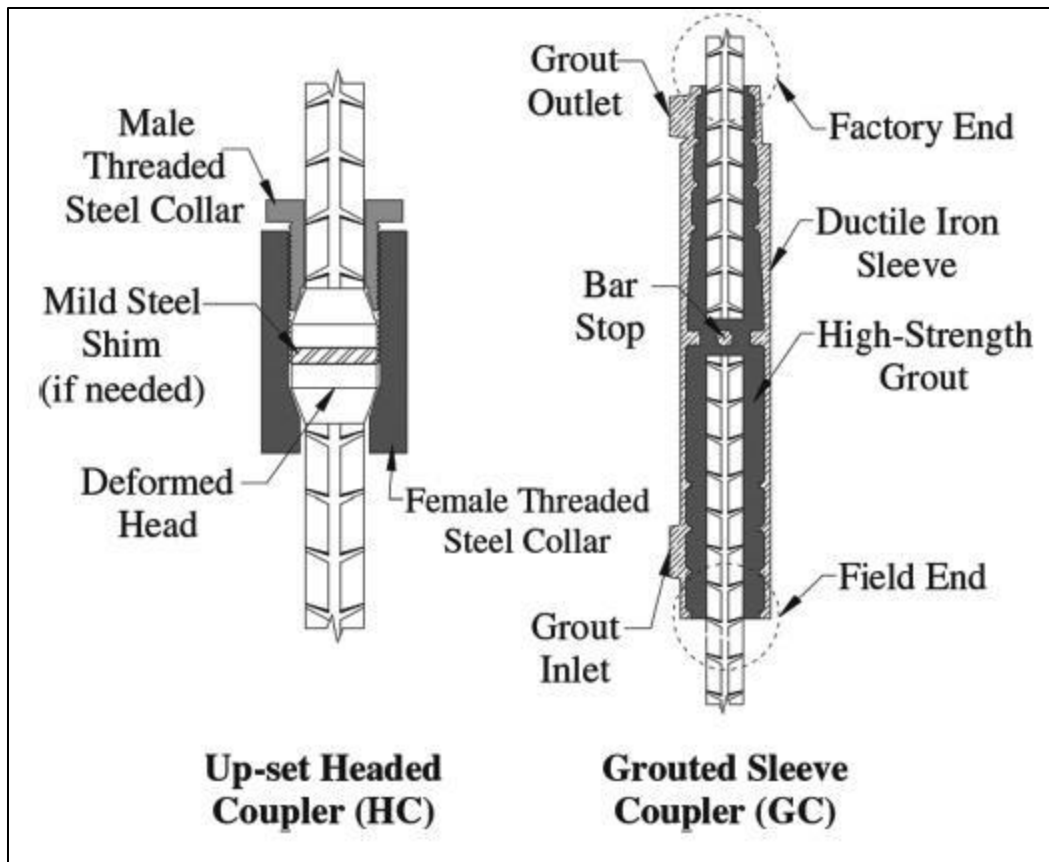


Figure 1-2. Two types of Coupler used in the research [7].

were used on the spliced bars, mid-section of the coupler, and within the coupler (on the rebar inside the coupler). Results from these tests showed that the imposed displacement rate made a slight difference in the overall performance of the systems. Results also showed that the bar fractured away from the coupler region.

An experimental study was carried out on grout-filled sleeves in air, as opposed to a grout-filled sleeve inside a concrete member [9]. One such study is a comprehensive investigation of two commercially available grout-filled sleeves (NMB Splice Sleeve and Lenton Interlok) under slip, fatigue, ultimate load, and creep. As a result of this study, both sleeves were approved for bridge applications in the State of Michigan, as they met the requirements set by the AASHTO LRFD Bridge Design Specifications [10]. Also, results showed that they both conformed to the Type 2 connection requirements of the ACI-550 Code,

enabling their application even in the plastic hinge regions of building elements in Michigan [11].

Aida et al. (2005) reported on experimental testing of three  $\frac{3}{4}$ -scale specimens in Japan, two of which used NMB Splice Sleeves to connect columns to footings [12]. The specimens, representing railroad bridge column to footing connections, were heavily reinforced and tested under cyclic loading to investigate their inelastic performance. Specimens with NMB Splice Sleeves showed acceptable inelastic behavior under cyclic loads compared to cast-in-place specimens. The maximum load resisted by the two specimens with the NMB Splice Sleeves was 7% to 11% greater than that for the cast-in-place specimen.

Yoshino et al. (1996) had proposed an innovative shear reinforcing configuration called the Intensive Shear Reinforcing (ISR) method, for precast concrete elements connected by means of NMB Splice Sleeves [13]. Transverse reinforcement in this configuration was concentrated at both ends of the sleeves, contrary to the conventional method in which hoops are placed at a particular spacing everywhere along the member. The ISR method offers the advantage of better constructability as shown in **Figure 1-3**. According to results from the experimental phase of the study, including monotonic and cyclic loading of both systems, the ISR method is comparable with the conventional detail. A strut-and-tie model was also developed in the analytical phase of the study, depicting the load transfer in the sleeve zone. This patented technique is used in building construction in Japan.

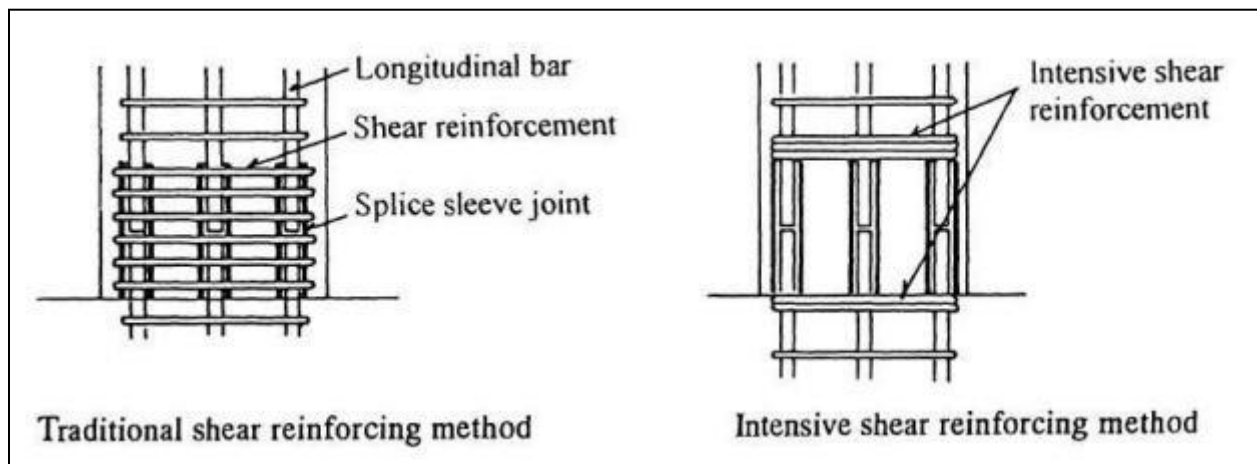


Figure 1-3. ISR method for precast reinforced concrete members [13].

The Splice Sleeve Company carried out cyclic tests on building column specimens that incorporated NMB Splice Sleeves to connect the longitudinal column bars [14]. Different levels of axial load, shear reinforcement, existence of shear keys, and ultimately the location of Splice Sleeves, were considered as test variables and investigated in this experimental study that included a total number of nine test specimens. A comparison between the results of the monolithic specimen with the other specimens indicated acceptable performance of the splice sleeves in terms of both strength and ductility properties. It was, however, observed that both the test setup and test specimens were not typical of bridges.

Matsuzaki et al. (1987) conducted research studies on individual NMB Splice Sleeves as well as test specimens connected by means of such devices [15]. He presented the results of monotonic and cyclic tests on various sleeve sizes connecting different size steel bars. A significant contribution of this investigation was the characterization of slip and pull-out properties of the system, in addition to illustration of the stress transfer between bars and the cast iron sleeve. The result of this study was then utilized in an analytical effort to replicate the response of precast components connected by means of such devices, under reversed cyclic slow loading history. **Figure 1-4** shows the result of the aforementioned test on a spliced sleeve connection (NO2) versus another specimen with typical connection details (NO1), at failure. The overall performance of all test specimens implies a similar response under the applied loading protocol, in terms of strength and displacement capacity; however, these results may not apply to

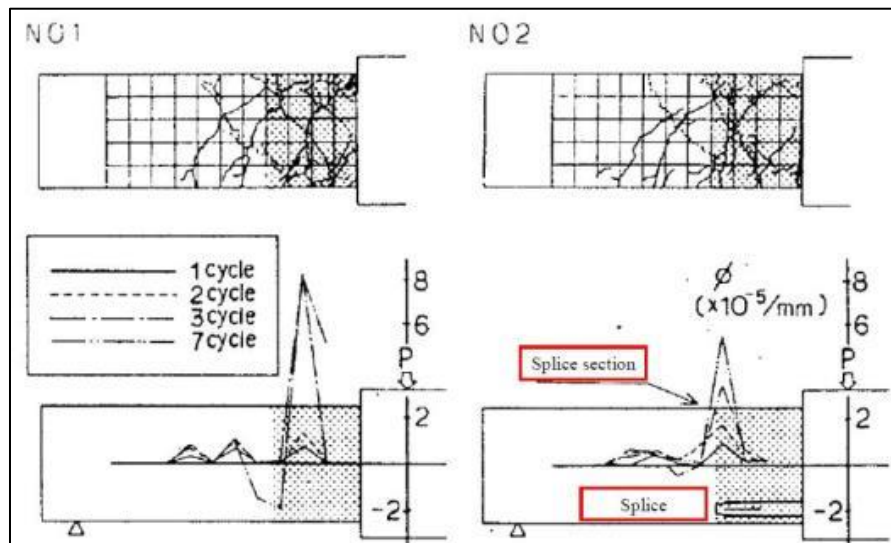


Figure 1-4. Damage state for two test specimens at failure [15].

precast reinforced concrete bridge columns, as there is apparently no axial load exerted on the specimens.

## 1.2 Research Objectives

This report describes a research program conducted to evaluate Grouted Splice Sleeve connections experimentally.

Grouted Splice Sleeves (GSS), alternatively called mechanical rebar splices or grout-filled steel sleeves, are hollow steel cylinders made of ductile iron. **Figure 1-5** shows two types of GSS utilized in this research project. Steel bars from two reinforced concrete components that are to be connected to each other are grouted at both sleeve ends for the longer GSS, or threaded into one end and grouted at the opposite end in the other type, as shown in **Figure 1-6**.

The shorter GSS is referred to as FGSS in which the threaded factory dowel is fastened to one end while the field dowel is grouted in the other end of the sleeve. This GSS is a product of Erico®, commercially available under Lenton® Interlok.

The longer alternative is referred to as GGSS indicating that rebar is grouted at both ends

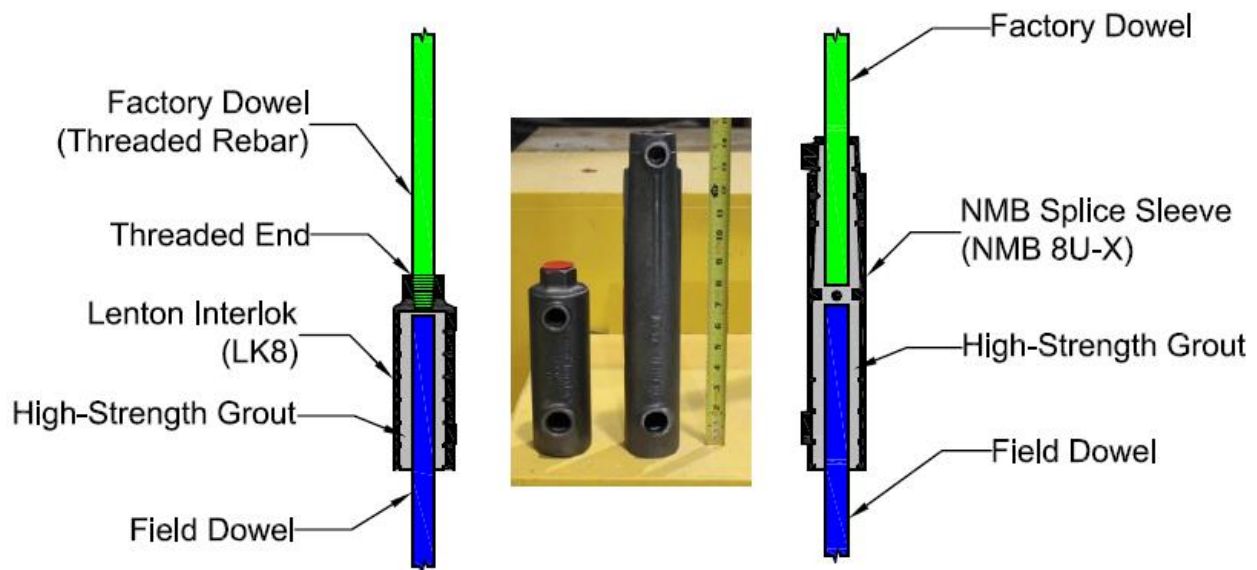


Figure 1-5. Two types of GSS incorporated in this research.

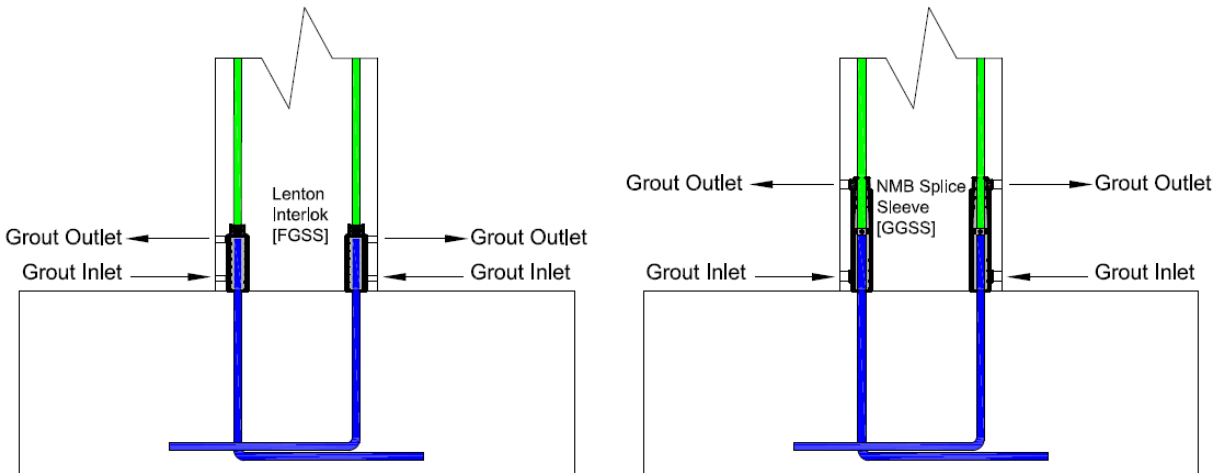


Figure 1-6. FGSS vs GGSS connections.

of the sleeve. This GSS is a product of Splice Sleeve North America and commercially available under the name of NMB Splice-Sleeve®.

This research was geared towards conducting reversed cyclic tests on half-scale specimens connected by two different GSS, to investigate their seismic performance in comparison to conventional cast-in-place bridge construction.

Two main categories were specified for this experimental program, based on the type of precast reinforced concrete components and sleeve type. Category-I specimens were column-to-footing connections in which GGSS were incorporated either in the column end or close to the top of the footing. Category-II specimens were column-to-cap beam connections by means of FGSS located in the column end or near the bottom of the cap beam. A control specimen was constructed in each category representing common cast-in-place design of reinforced concrete components. The performance of all GGSS and FGSS specimens is compared to that of the control specimens. The test matrix is shown in **Table 1-1**. GSS were placed inside the column end for the first set of specimens in each category. In the second set, GSS were embedded in the footing or cap beam. For the third set of specimens in each category, GSS were located inside the column end and debonding of dowel bars was implemented along the rebar length into the footing or cap beam. A more detailed discussion on fundamental differences between the test specimens in each category is provided in later chapters. **Figure 1-7** presents the configuration alternatives in both categories of test specimens.

Table 1-1. Test matrix.

	Test ID	Connection Type	Designation	Sleeve Type	Sleeve Location	Other
Category I	1	Column-Footing	GGSS-1	NMB-8UX	In Column	
	2	Column-Footing	GGSS-2	NMB-8UX	In Footing	
	3	Column-Footing	GGSS-3	NMB-8UX	In Column	Unbonded rebar in footing
	4	Column-Footing	GGSS-CIP	NA	NA	Cast-In-Place
Category II	5	Column-Cap Beam	FGSS-1	LK-8	In Column	
	6	Column-Cap Beam	FGSS-2	LK-8	In Cap beam	
	7	Column-Cap Beam	FGSS-3	LK-8	In Column	Unbonded rebar in cap beam
	8	Column-Cap Beam	FGSS-CIP	NA	NA	Cast-In-Place

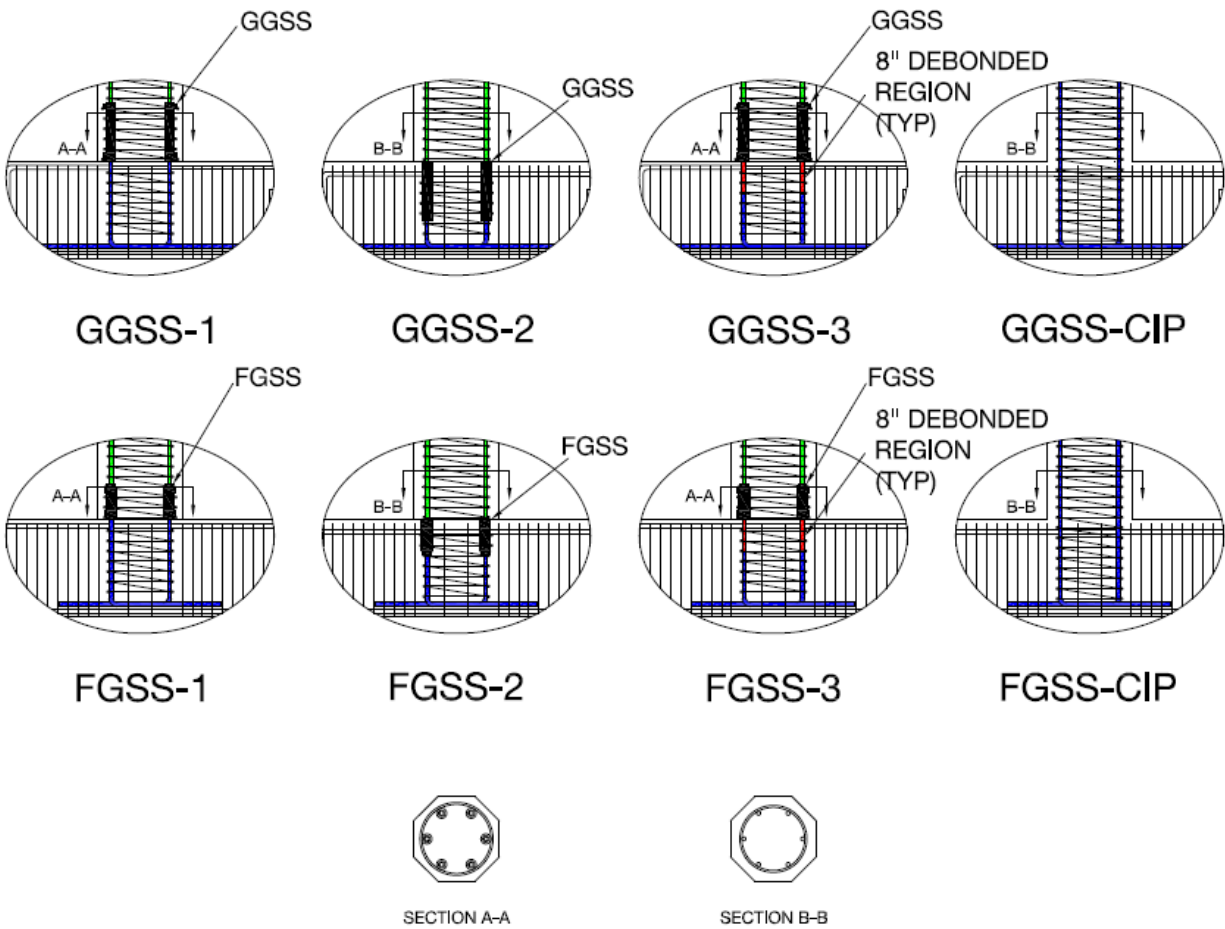


Figure 1-7. Configuration of test specimen alternatives.

The main objective of conducting this research was to gain more knowledge about GSS connections and their properties, understand their seismic performance, and compare the performance of such connections and common monolithic connections. Finally, the ultimate goal would be to translate the findings of this research into design recommendations.

### **1.3 Outline of Report**

This report was compiled in such a way as to clearly describe the sequence of tasks accomplished to carry out the research. Chapter 2 provides background information on the design, detailing, and construction of the test specimens. Step-by-step construction procedures undertaken for each specimen are shown at the end of the chapter.

Chapter 3 is focused on the test procedure including instrumentation and test setup. Various types of instrumentation used to collect data are described together with the quantity and location of each device. The test fixtures, data acquisition system, and loading protocol are discussed in depth before proceeding to the test results in Chapter 4. Test results are presented in depth for each test, accompanied by pertinent discussions on the specific criteria. Furthermore, characteristic results are presented in a comparative fashion within each category to offer a more profound understanding.

Chapter 5 includes the summary of the report together with the most significant findings. Design recommendations are described in Chapter 6.

## **2.0 DESIGN AND CONSTRUCTION OF TEST SPECIMENS**

### **2.1 Design of Test Specimens**

The specimens were designed and detailed to simulate typical prototype bridges constructed in the State of Utah, following the AASHTO LRFD Bridge Design Specifications (2012), and the AASHTO Guide Specifications for LRFD Seismic Bridge Design (2011), in accordance with capacity-based design procedures [10, 16]. A circular configuration of column longitudinal bars and an octagonal column cross section were adopted to facilitate the process of pre-casting the columns, since this is the method of choice in the State of Utah. Currently, the aforementioned design codes in addition to the Caltrans Seismic Design Criteria (SDC) inhibit the splicing of rebar, including mechanical anchorage devices, in the plastic hinge region of ductile members, for bridges located in moderate-to-high seismic areas [17]. In the AASHTO Guide Specifications for LRFD Seismic Bridge Design (2011), this would apply to Seismic Design Categories (SDCs) C and D. Thus, the preliminary design and detailing was developed for test specimens without any type of GSS, i.e. cast-in-place specimens for each category. The design was then adjusted to accommodate the GSS within the precast specimens as needed, and essential modifications were considered accordingly.

The test specimens were half-scale models of common prototype highway bridges in the state of Utah. In order to achieve an acceptable test model, many multi-column bent cap systems were studied, including the Riverdale Road Bridge over I-84. The column dimensions, main longitudinal bars and configuration, and footing or cap beam dimensions were acquired by considering approximately 50 percent of the actual properties. **Figure 2-1** depicts a sample prototype bent-cap system in which areas of interest for this research are shown.

The final column height for all specimens was selected to be 8 ft-6 in. with a 21-in. square column head in the top 1 ft-6 in. portion. The lateral load, however, was intended to be applied at a height of 8 ft from the column end. The cross section changed to an octagon along the remainder of column height to facilitate casting of concrete. Six No. 8 bars in a circular arrangement, in addition to a No. 4 spiral with a pitch of 2½ in., made up the column cage. The longitudinal and volumetric transverse reinforcement ratios were 1.3% and 1.9% respectively.

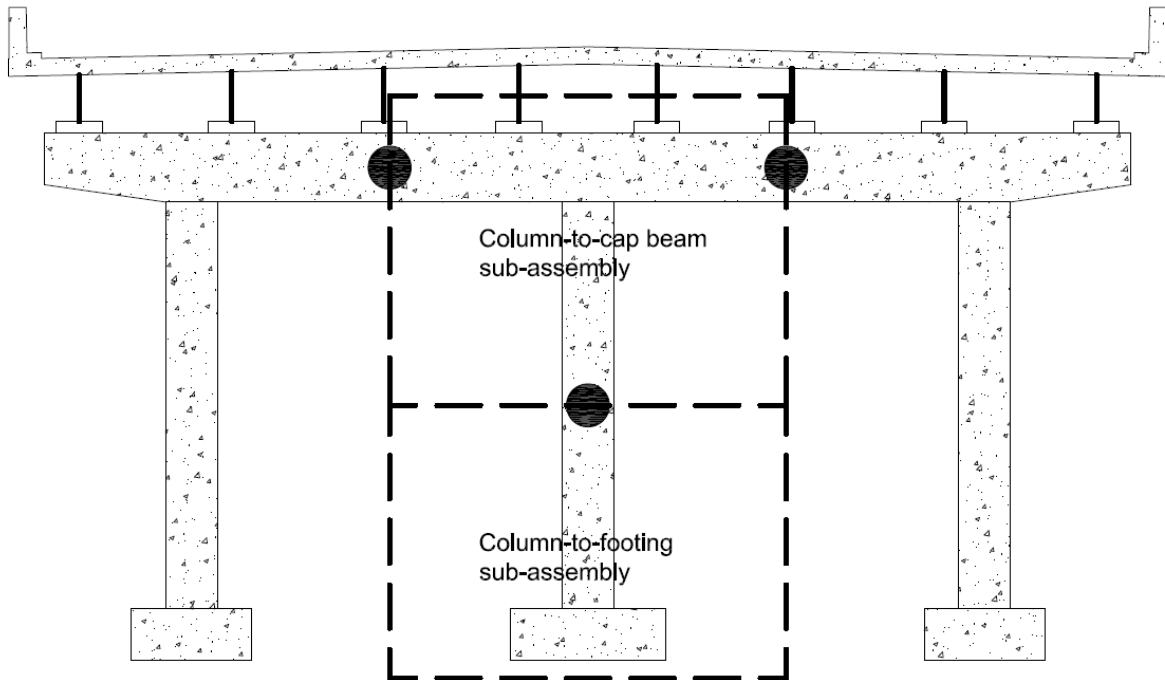


Figure 2-1. Prototype bridge with highlighted portions representing specimen design.

A series of sectional analyses were carried out to design the footing and cap beam. The results from such analyses were also used in the determination of proper instrumentation devices. For instance, the ultimate curvature values, obtained from a moment-curvature analysis, were used to select Linear Variable Differential Transformers (LVDT), with a desirable maximum stroke. A preliminary nonlinear static analysis was performed to predict the maximum lateral load and displacement. The footing and cap beam were designed so as not to be severely damaged under that maximum predicted load. Probable material properties for a grade 60 steel and concrete were assumed in this preliminary study. **Figure 2-2** presents one such analysis with 28-day concrete strength of 6 ksi, steel yield strength of 68 ksi, and an axial load corresponding to 9% of the axial compression capacity of the column.

The footing was designed as a 6-ft long x 3-ft wide x 2-ft deep precast concrete element and consisted of No. 8 longitudinal bars enclosed by No. 4 double hoops. The cap beam was designed as a 9-ft long x 2-ft wide x 2-ft deep precast pier cap; it had the same rebar size and arrangement as the footing. The footing and pier cap were designed to remain linearly elastic and not undergo plastic deformations. The design inhibits shear failure from occurring in the

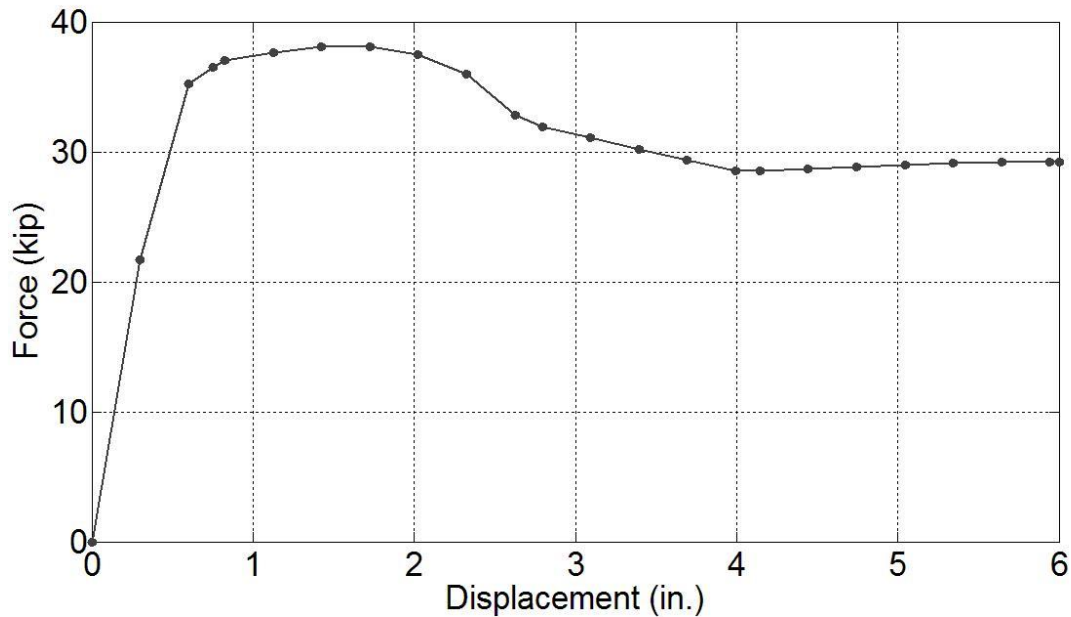


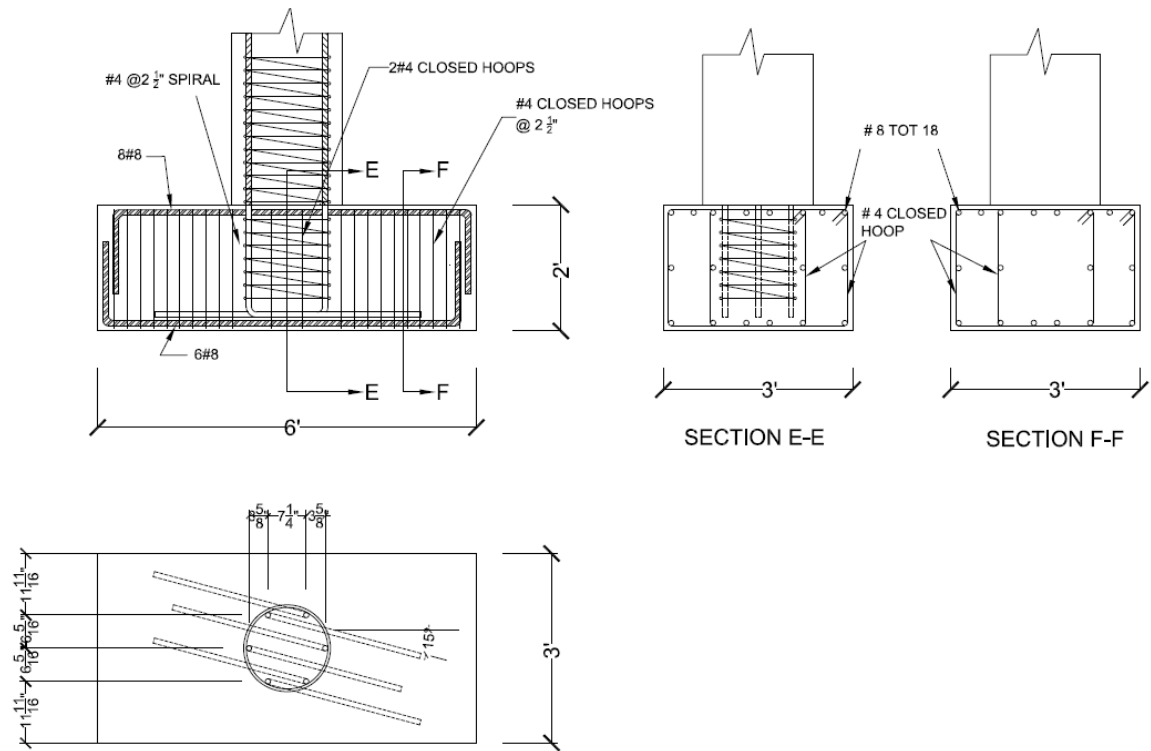
Figure 2-2. Preliminary pushover analysis on monolithic test specimen (prediction).

column; the desirable column failure mode is set to either be flexural or splice failure.

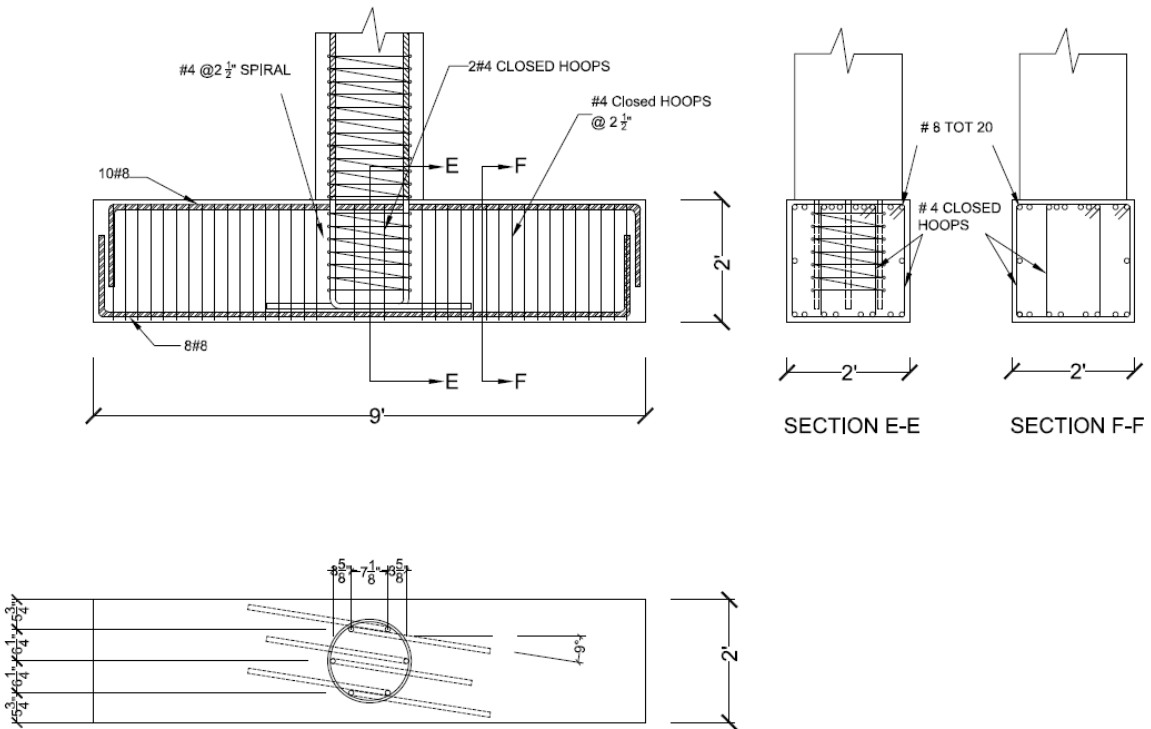
**Figure 2-3** shows the dimensions and details of the reinforcement, with a focus on the joint region, for both categories of specimens without the presence of the GSS. This could be considered as the monolithic construction commonly followed in cast-in-place construction. The design detail for each test specimen is summarized in the next section. Dowel bar tails were bent inward to achieve a better performance under lateral cyclic loads. This is a required provision for SDC D in accordance with AASHTO [16].

### 2.1.1 AASHTO-Seismic Provisions

A summary of AASHTO-Seismic provisions pertinent to design and detailing of test specimens is provided in **Table 2-1**. All provisions stated herein are associated with reinforced concrete components which are addressed in Chapter 8 of the seismic code [16]. Article number, equation, and comments on each particular item are presented in a table format including the definition of relevant parameters.



(a) Column-to-Footing joint detailing.



(b) Column-to-Cap beam joint detailing.

Figure 2-3. General design and detailing of joint region for both categories of specimens.

Table 2-1. AASHTO-Seismic provisions pertinent to design and detailing of test specimens.

Article Number	Subject	Equation	Parameters	Remarks
8.4.1	Rebar type	NA	NA	ASTM A 706 rebar was used
8.4.2	Stress properties of rebar	NA	NA	Proper rebar properties used in design process
8.4.4	Concrete properties	$f'_{ce} \geq 1.3f'_c$ $\epsilon_{cu} = 0.005$	$f'_c$ = 28-day concrete compressive strength $f'_{ce}$ = Expected concrete compressive strength $\epsilon_{cu}$ = Ultimate compressive strain	Used in modeling confined and unconfined concrete
8.5	Column moment capacity	$M_{po} = \lambda_{mo} M_p$ $\lambda_{mo} = 1.2$	$M_p$ = Plastic moment capacity $M_{po}$ = Overstrength plastic moment capacity $\lambda_{mo}$ = Overstrength magnifier	For ASTM A 706 rebar
8.6.2	Concrete shear capacity	$v_c = \alpha' \left(1 + \frac{P_u}{2A_g}\right) \sqrt{f'_c}$ $\alpha' = \frac{0.03}{\mu_D} \rho_s f_{yh}$ $\rho_s = \frac{4A_{sp}}{sD'}$	$v_c$ = Concrete shear capacity $P_u$ = Ultimate compressive force $A_g$ = Gross area of member $\mu_D$ = Maximum local displacement ductility	Used to compute shear capacity of column

			$f_{yh}$ = nominal yield strength of transverse rebar $A_{sp}$ = area of transverse rebar $s$ = Transverse rebar spacing or pitch $D'$ = Diameter of hoop or spiral	
8.6.3	Rebar shear capacity	$V_s = \frac{\pi}{2} \left( \frac{nA_{sp}f_{yh}D'}{s} \right)$	$n$ = Number of spiral or hoop core sections	Used to compute shear capacity of column
C8.6.3	Longitudinal rebar spacing	NA	NA	Maximum spacing of column longitudinal bars was limited to 8 in.
8.6.5	Minimum shear reinforcement	$\rho_s \geq 0.005$		Holds true for test specimens
8.7.1	Minimum lateral strength	$M_{ne} \geq 0.1P_{trib} \left( \frac{H_h + 0.5D_s}{\Lambda} \right)$	$M_{ne}$ = Nominal moment capacity $P_{trib}$ = Greater of dead load or force associated with tributary seismic mass $H_h$ = Column height $D_s$ = Depth of superstructure $\Lambda$ = Fixity factor per 4.8.1 [16]	
8.7.2	Maximum axial load	$P_u \leq 0.2f'_c A_g$		Axial load level kept below this value for all test models
8.8.1	Maximum column longitudinal rebar	$A_l \leq 0.04A_g$	$A_l$ = Area of longitudinal reinforcement	Actual rebar ratio provided is 0.013
8.8.2	Minimum column longitudinal	$A_l \geq 0.01A_g$		Actual rebar ratio provided is 0.013

	rebar			
8.8.3	No splicing of rebar in plastic hinge zone of ductile members	NA	NA	No splicing of column bar in monolithic specimens
8.8.4	Anchorage length	$l_{ac} \geq \frac{0.79d_{bl}f_{ye}}{\sqrt{f'_c}}$	$l_{ac}$ = Anchorage length $d_{bl}$ = diameter of longitudinal column bar $f_{ye}$ = Expected yield strength of longitudinal column bar	Accommodated in monolithic specimens. Tails should be pointed inward for SDC D.
8.8.6	Maximum bar diameter	$d_{bl} \leq \frac{0.79\sqrt{f'_c}(L - D_c)}{f_{ye}}$	$D_c$ = Column depth	
8.8.7	Lateral reinforcement inside plastic hinge region	NA	NA	At spiral discontinuities, spiral shall terminate with one extra turn plus a tail equal to cage diameter. For all precast test specimens, two extra turns were provided.
8.8.8	Lateral reinforcement outside plastic hinge region	NA	NA	Provide 50% of required lateral reinforcement in plastic hinge region. Same lateral rebar ratio (1.9%) in plastic hinge region was provided for all specimens.
8.8.9	Lateral reinforcement detailing	NA	NA	Seismic hooks consist of a 135° bend, plus an extension of not less than the larger of 6 bar diameters or 3 in.

8.13.2	Joint proportioning	$p_c \leq 0.25 f'_c$ $p_t \leq 0.38 \sqrt{f'_c}$	$p_c$ = Principal compressive stress $p_t$ = Principal tensile stress	All test specimens conformed to this provision.
8.13.3	Minimum joint shear reinforcement	$\rho_s = \frac{0.4 A_{st}}{l_{ac}^2}$	$A_{st}$ = Total area of column reinforcement anchored in the joint	Actual value for test specimens exceeded this limit.
8.13.4.1.2a	Vertical stirrups	$A_s^{jv} \geq 0.2 A_{st}$	$A_s^{jv}$ = Vertical stirrup area	Vertical stirrups distributed over Dc/2 on each side of joint region.
8.13.4.1.2b	Horizontal stirrups	$A_s^{jh} \geq 0.1 A_{st}$	$A_s^{jh}$ = Horizontal stirrup area	Maximum vertical spacing of these bars shall be 18 in.
8.13.4.1.2b	Horizontal side reinforcement	$A_s^{sf} \geq \text{Max}\{0.1 A_{Cap}^{Top}, 0.1 A_{Cap}^{Bot}\}$	$A_s^{sf}$ = Horizontal side reinforcement $A_{Cap}^{Top}$ = Area of cap beam top flexural rebar $A_{Cap}^{Bot}$ = Area of cap beam bottom flexural rebar	Side bars were provided to conform to this article.

## 2.2 Column-to-Footing Connections

All four specimens in this category had identical geometric properties and similar reinforcement details in the plastic hinge region. Differences included alterations in GGSS location, either inside the column or inside the footing, in addition to debonded length of rebar that was only present in the third set of specimens, i.e. GGSS-3. The last specimen—GGSS-CIP— simply did not have any GGSS, for it served as the control test specimen.

### 2.2.1 GGSS-1

The first specimen in this category was comprised of a precast column with GGSS embedded in the column end, and a precast footing with projected dowel bars for a length of 7 in. Rebar cages were constructed in the Structures Laboratory at the Department of Civil and Environmental Engineering of the University of Utah. The precast column was first built by fastening the GGSS to a wooden template by means of pin setters. Column longitudinal bars were then inserted inside the GGSS, which was confined by a closely-spaced steel spiral. The spiral used over the GGSS region had a 1 ¾-in. larger diameter than the spiral for the remaining portion of the column, due to a larger diameter of the GGSS compared to column longitudinal rebar. This resulted in an overlapping spiral region right above the GGSS. Beginning with dowel bars, the precast footing was then constructed by arranging the footing core rebar cage in a circular configuration along with staggering inward angled tails. The dowel bar tails measured 2 ft-6 in. to extend out from the core and provide a stable base for the dowel rebar cage. **Figure 2-4** shows the precast components under construction.

Longitudinal and transverse bars were tied at every bar intersection to achieve a robust rebar cage. This was significant because cages had to be transported to the precast plant for casting concrete. **Figure 2-5** shows the details of GGSS-1 and the rebar cages that formed the test model. Wooden templates, as shown, were utilized in the construction process to prevent mismatch of the precast components.

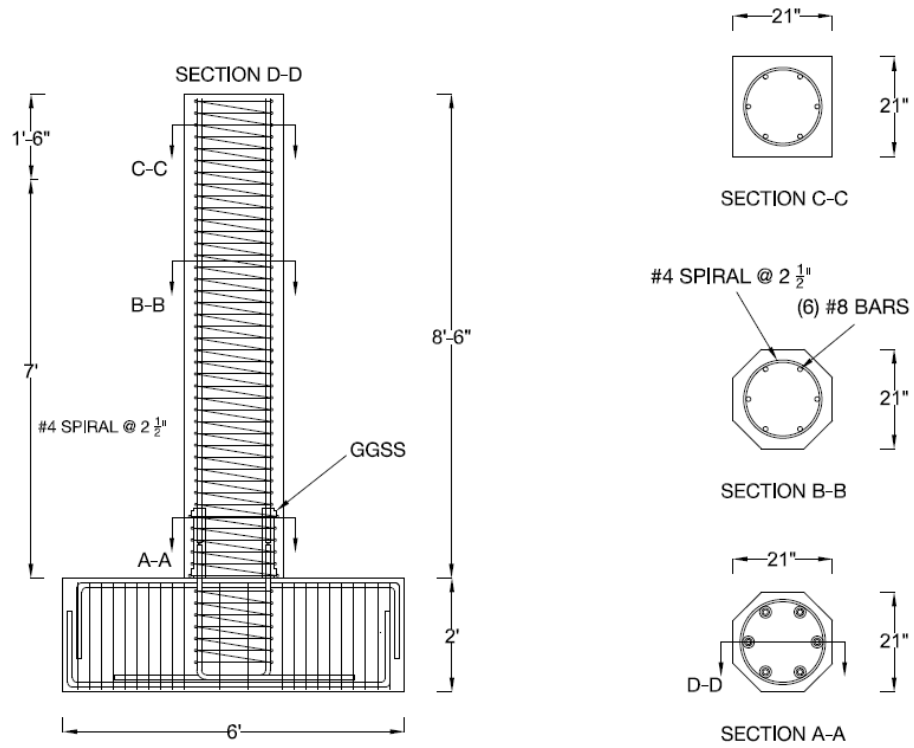


(a) Column end GGSS and overlapping spiral. (b) Footing dowel bars with inward tails.

Figure 2-4. GGSS-1 precast components under construction.

**Figure 2-6** shows the GGSS-1 column and footing reinforcement inside the forms at the precast plant. Concrete casting was performed with great care to avoid damage to instrumentation wires. 4 in. x 8 in. cylinders were made according to ASTM C39 [18], to perform compression tests before removing the specimens from the forms, at 28 days after casting, and on test day. 1 ½” PVC pipes were inserted inside the footing cage to provide room for anchors that would clamp the specimen down to the testing frame. The average concrete compressive strength at 28 days for this specimen was 5.3 ksi.

The precast components were taken out of the forms when concrete strength reached 3 ksi. A step-by-step procedure was carried out for the grouting operation, in which the grout was pumped into the sleeves, when connecting the precast components. A proprietary non-metallic, non-shrink, early high strength grout, particularly developed for this type of GSS was used in accordance with manufacturer instructions. One 55-lb bag of grout gradually mixed with 0.98 gallons of water was sufficient to fill all six GGSS and cast the bed grout at the interface of the two components. An electric mixer with a Jiffler paddle was used to mix the grout with water, continuously for 2 ½ minutes. A grout flow test indicated that the grout was in satisfactory condition with an acceptable puddle diameter of 6.5 in. A Kenrich GP-2HD hand pump was utilized to pump the grout into the GGSS by inserting the nozzle into the bottom port. Following the ASTM C109 instructions, several 2-in. cubes were made to obtain the 28-day and test-day compressive strength of the grout [19].



(a) Details of GGSS-1.



(b) Column and footing rebar cages.

Figure 2-5. GGSS-1 specimen details and rebar cages.



Figure 2-6. GGSS-1 precast components inside concrete forms.

A ¼-in. bed grout was incorporated at the column-to-footing interface by placing proper size spacers at the interface of the column and footing. A square wooden frame was made to pour the bed grout, as demonstrated in **Figure 2-7**. The column was lowered slowly, making sure that it rested plumb and level on the footing.

This specimen remained attached to the testing frame for a minimum of 28 days before testing, for the grout to cure completely. In the meantime, test preparation and external instrumentation were carried out. The average compressive strength of the grout at 28 days was found to be 14.4 ksi. **Figure 2-8** displays specimen GGSS-1 in the final testing position, at the end of the grouting operation.



Figure 2-7. Grouting operation for GGSS-1.



Figure 2-8. GGSS-1 in the final position.

### 2.2.2 GGSS-2

The second alternative in the column-to-footing connection category was to change the location of the GGSS from column end to the top of the footing. In other words, dowels protruded 7 in. from the column end. This option was investigated primarily because the AASHTO-Seismic Code [16] does not prohibit such an application currently, as the GGSS would be outside the column plastic hinge region; however, the response of such a connection under simulated ground motions has not been well documented. This particular configuration was implemented in the Provo to Salt Lake Frontrunner rail bridge project in which both column-to-footing and column-to-cap beam connections incorporated GGSS outside the piers. On the other hand, a less severe disruption of the commonly adopted column plastic hinge region, located at the column end was anticipated, by shifting the GGSS location from the column to the footing.

In the construction phase, the column was built first because there was no special consideration, due to the GGSS not being located in the column and thus easier to build. Therefore, 6 No. 8 bars were arranged in a circular configuration using a wooden template. Next, a No. 4 spiral was wrapped around the column main bars. The GGSSs were fastened to a wooden template by means of pin setters to be placed in the top portion of the footing. **Figure 2-9** shows the precast components under construction. **Figure 2-10** displays the footing core rebar cage placed on the footing main bottom bars and tied firmly to the rest of the



(a) Column cage with projecting bars.



(b) GGSS fastened to template for the footing.

Figure 2-9. GGSS-2 precast components under construction.

reinforcement; the core was plumbed and level in all directions. Construction of the precast footing was carried out with some level of practical difficulty because of a highly congested rebar zone within the joint area. This issue made other phases relatively more complicated too, such as instrumentation and casting of concrete. The tails shown in this figure had a length of 2 ft-4 in. and were oriented inward parallel to other rebar tails, in a plane intersecting the plane of the main footing bars.

The rebar cages became sturdy by tying the longitudinal bars to the transverse bars at all corners, in order for the cages not to get distorted while transporting them to the precast plant, where concrete would be cast. The details of the GGSS-2 specimen are presented in **Figure 2-11** and rebar cages that formed the test model are presented in **Figure 2-12**.

Concrete was cast under a highly supervised condition to avoid damage to instrumentation wires. 4 in. x 8 in. concrete cylinders were made to carry out compression tests before removing specimens from the forms, at 28 days after casting, and on test day. 1 ½" PVC pipes were placed inside the footing where the support bolts would be inserted to attach the



Figure 2-10. GGSS-2 precast footing core rebar cage.

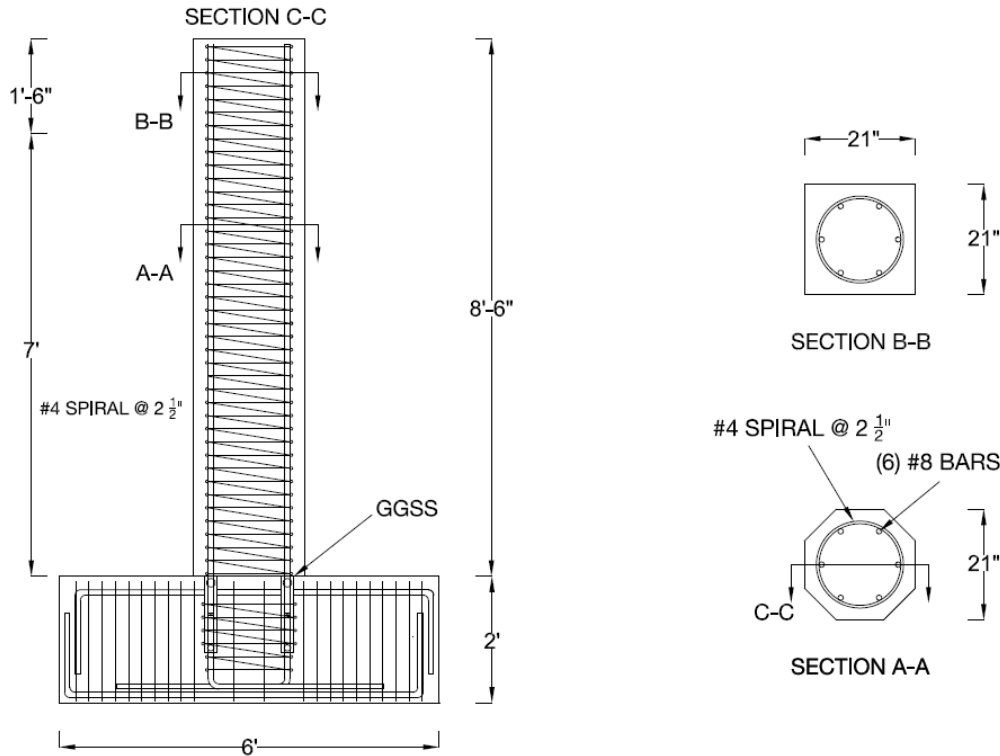
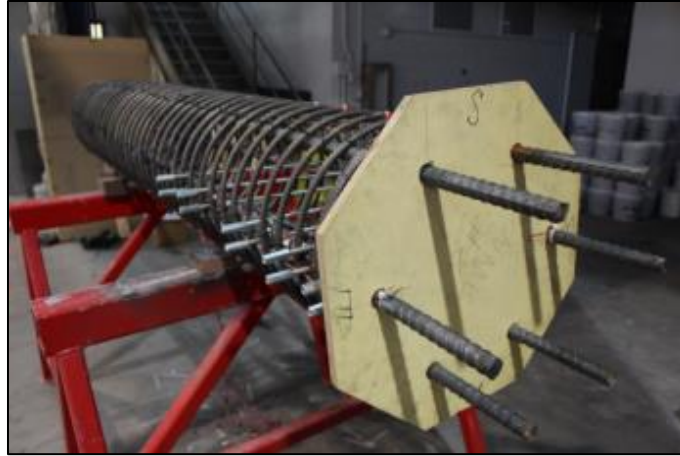


Figure 2-11. Details of GGSS-2.

specimen to the test frame. **Figure 2-13** shows the GGSS-2 precast components in concrete forms, right before concrete was cast. The average compressive strength of the concrete for specimen GGSS-2 was 3.9 ksi at 28 days.

The precast pieces were removed from the forms when concrete had a compressive strength of 3 ksi. A step-by-step grouting operation procedure was followed in accordance with the manufacturer instructions as described in **Section 2.2.1** for GGSS-1. In contrast to the grouting operation for GGSS-1, a pre-grout installation technique was adopted to facilitate the erection process. In this process, plastic plugs were used to seal the GGSS inlet and outlet, before casting concrete. During the installation, all of the GGSS were first filled with grout from the wide end opening. A Kenrich GP-2HD hand pump was utilized to pump the grout into the GGSS by inserting the nozzle into the wide end of the GGSS.

A ¼-in. bed grout was incorporated at the column-to-footing interface by placing proper size spacers at the interface between the column and footing. A square wooden dam was made to



(a) Column rebar cage.



(b) Footing rebar cage.

Figure 2-12. GGSS-2 rebar cages.

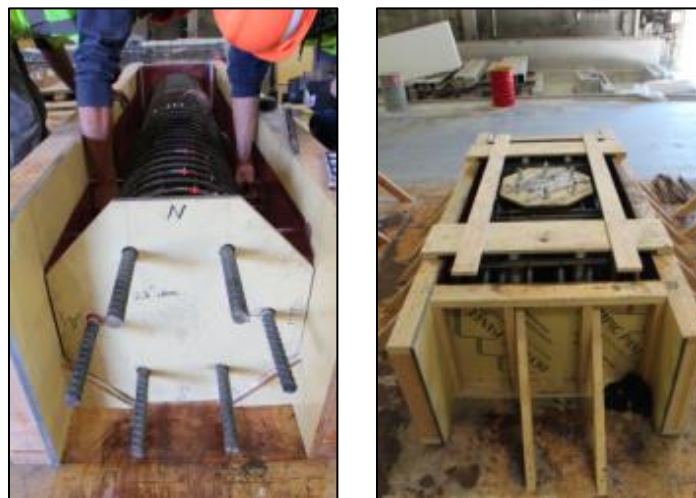


Figure 2-13. GGSS-2 precast components inside concrete forms.

pour the bed grout, as demonstrated in **Figure 2-14**. The column was lowered into position gradually and slowly, making sure that it rested plumb and level on the footing.

Temporary wood bracing was used to prevent movement of the GGSS-2 column until the grout developed sufficient strength. This specimen remained attached to the testing frame for a minimum of 28 days before testing, for the grout to cure completely. In the meantime, test preparation and external instrumentation were carried out. The average compressive strength of the grout at 28 days was found to be 11.1 ksi. **Figure 2-15** displays specimen GGSS-2 in the final testing position, at the end of the grouting operation.



Figure 2-14. Grouting operation for GGSS-2.



Figure 2-15. GGSS-2 in final position.

### 2.2.3 GGSS-3

This specimen had nearly the same characteristics as GGSS-1 in terms of dimensions, steel reinforcement configuration, and location of the GGSS. The key difference between the two specimens was only a deliberate and localized debonding implemented on an 8-in. portion of the footing dowel bars right below the column-to-footing interface. Two layers of duct tape were wrapped around the designated rebar region to ensure there was no bond between the rebar and concrete, as shown in **Figure 2-16**.

The main objective of the intentional debonding of rebar was to provide a better strain distribution along the critical region of the steel bars which was outside the GGSS, within the footing. This would reduce the strain concentration over the short length around the column-to-footing interface and hence, any premature rebar fracture would be delayed.



Figure 2-16. Debonded region of the dowel bars for GGSS-3.

The 8-in. debonding length was obtained by subtracting the required development length of a hooked rebar from the available depth in the footing. This was carried out in accordance with the AASHTO LRFD Bridge Design Specifications, although the AASHTO-Seismic Code inhibits a reduced anchorage length even if standard hooks are incorporated [10, 16]. The basic development length requirement was used, as shown in Equation (1), along with pertinent modification factors.

$$l_{dh} = \frac{38.0d_b}{\sqrt{f'_c}} \quad (1)$$

where,  $l_{dh}$  is the basic development length of a standard hook in tension,  $d_b$  is the bar diameter, and  $f'_c$  is the specified compressive strength of concrete at 28 days.

Similar to the GGSS-1 specimen, the GGSS were placed in the column end and 7-in. dowel bars projected out from the precast footing. Column longitudinal bars were then inserted into the factory dowel end of the GGSS and consequently tied to a No. 4 spiral with a pitch of 2.5 in. The section right above the GGSS in the column had overlapping confinement steel because of a larger diameter spiral utilized over the GGSS length. Next, the footing was built including the partially debonded bars extending out from the top of the footing cage. The hooked bar tails measured 2 ft-6 in., and extended into the core to provide a sturdy base for dowel bars. **Figure 2-17** shows the precast components under construction.

All bars were tied at every corner to achieve a robust rebar cage that would not become distorted during transportation for concrete casting. The details of the test specimen GGSS-3 are illustrated in **Figure 2-18** and the rebar cages for the precast components are presented in **Figure 2-19**. The dowel bar length shown in this figure was left considerably larger than needed before casting the concrete in order to keep the footing rebar core as sturdy as possible. All dowel bars were cut to length by a grinder right before grouting operation.

Concrete was cast into the forms smoothly to ensure the congested joint area was filled completely, without introducing damage to instrumentation. Several 4 in. x 8 in. cylinders were made following ASTM C39, for future investigation on the compressive strength of the concrete. Eight 1 ½” PVC pipes were positioned inside the footing rebar cage to accommodate the interior support rods and eventually fasten the test specimen to the test frame. **Figure 2-20** shows



(a) Column end GGSS and overlapping spiral. (b) Footing dowel bars tied to rebar cage.

Figure 2-17. GGSS-3 precast components under construction.

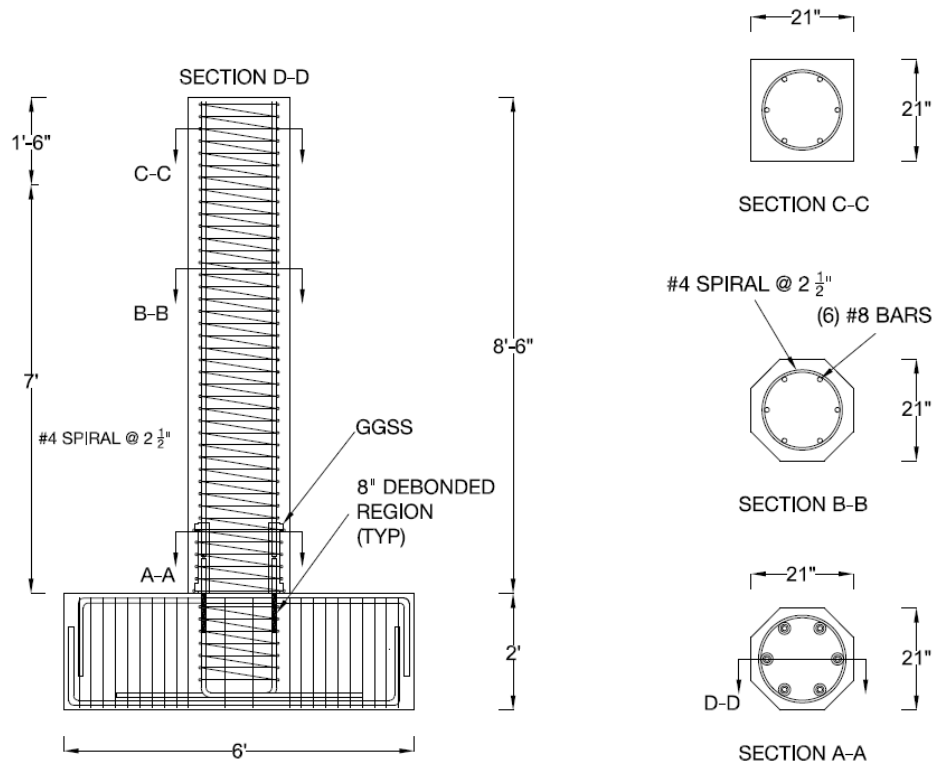


Figure 2-18. Details of GGSS-3.

the GGSS-3 column and footing rebar cages in concrete forms, before concrete was cast. The average compressive strength of concrete at 28 days was obtained as 6.7 ksi.

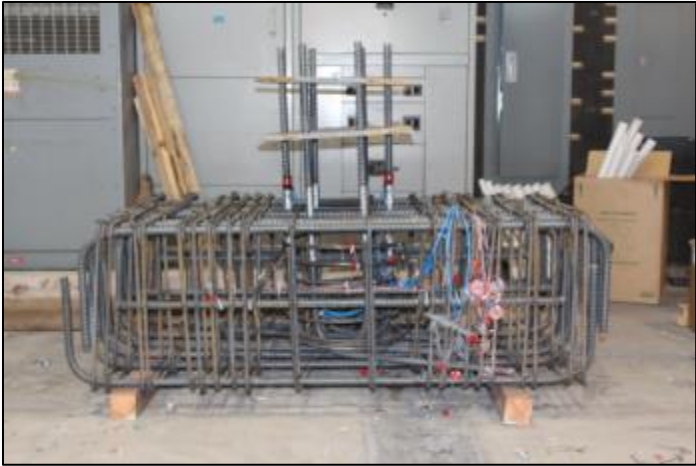
The precast components were removed from the forms when concrete strength reached 3 ksi. A step-by-step procedure was carried out to perform the grouting operation, as described for the previous test specimens. The grout was pumped into each GGSS by inserting the nozzle into the bottom port. **Figure 2-21** shows ¼” spacers taped to the interface, and washers placed over the dowels to prevent the bed grout from entering the GGSS. The wooden dam used to cast the bed grout is also visible in this figure. Following ASTM C109, several 2-in. cubes were made to obtain the 28-day and test-day compressive strength of the grout.

Temporary wood bracing was used to prevent movement of the GGSS-3 column until the grout developed sufficient strength. This specimen remained attached to the testing frame for a minimum of 28 days before testing, so the grout could cure completely. In the meantime, test preparation and external instrumentation were carried out. The average compressive strength of

the grout at 28 days was 15.6 ksi. **Figure 2-22** displays GGSS-3 in the final testing position, at the end of the grouting operation.



(a) Column rebar cage.



(b) Footing rebar cage.

Figure 2-19. GGSS-3 rebar cages.

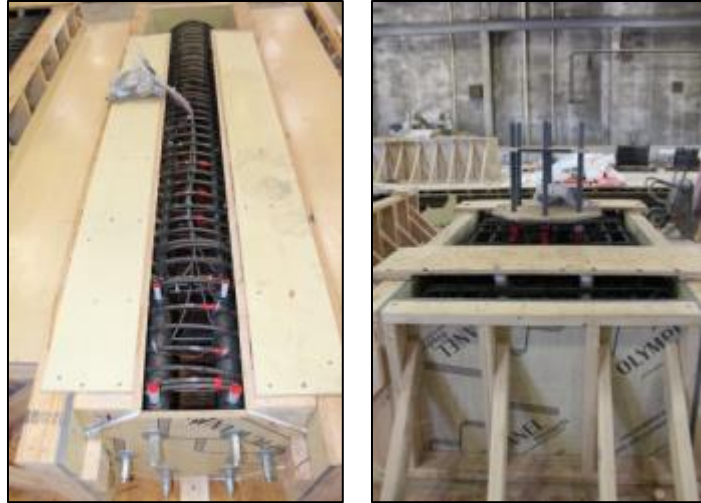


Figure 2-20. GGSS-3 precast components inside concrete forms.



Figure 2-21. Grouting operation for GGSS-3.



Figure 2-22. GGSS-3 in final position.

#### 2.2.4 GGSS-CIP

GGSS-CIP was the control specimen in this connection category; i.e. column-to-footing connections. It represents monolithic construction without any GGSS to splice the reinforcement. The results from all experimental tests on the precast column-to-footing connection specimens will be compared to the test results for the GGSS-CIP. The spiral reinforcement did not have any splice either, confining the core concrete from top of the column monolithically down to the bottom of the footing, as a single long helical reinforcement around the longitudinal bars. The diameter of the spiral was kept the same as for the spiral around the column bars for the other three test models, implying an identical moment arm for column longitudinal bars in all test specimens.

Construction of this last specimen began with building the column rebar cage by using the same wooden template as for the previous specimens. Hanging from a forklift, the column

longitudinal bars were tied to the spiral at every corner from the bottom towards the column top, as shown in **Figure 2-23**.

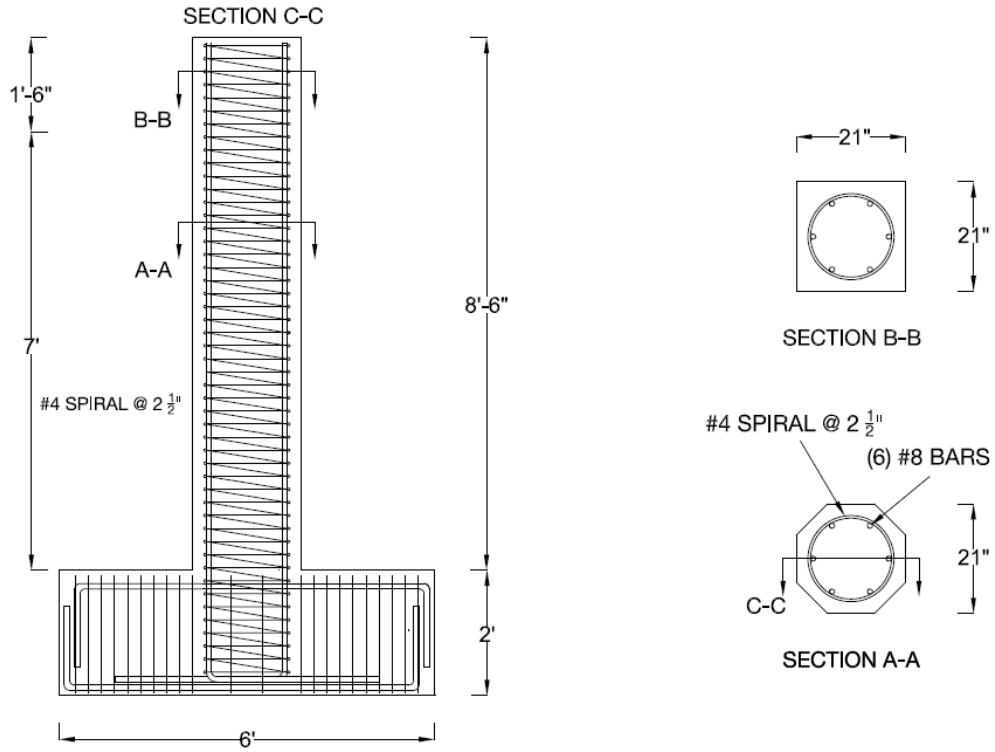
Tails of the column hooked bars were 2 ft-6 in. long and oriented into the joint core to conform to the AASHTO-Seismic Code and also to provide a stable base for the column rebar cage during the construction phase. **Figure 2-24** shows the details of the GGSS-CIP in addition to the finalized rebar cage.

The constructed rebar cage was transported to the precast plant to cast the concrete. **Figure 2-25** shows this monolithic component sitting in the concrete form prior to casting. Several 4 in. x 8 in. cylinders were made to obtain the concrete compressive strength at different ages including before removal of the specimen from the form, at 28 days, and on the test day. As presented in **Figure 2-25**, 1 ½” PVC tubes were embedded inside the footing cage in order to fasten the specimen to the test frame. The average concrete compressive strength of this specimen was 5.2 ksi at 28 days.



Figure 2-23. Construction of GGSS-CIP.

Specimen GGSS-CIP was taken out of the form and transported back to the Structures Laboratory when the concrete strength reached 3 ksi. It was fastened to the test frame while test preparation procedures were implemented. **Figure 2-26** displays the test specimen in the final testing position.



(a) Details of GGSS-CIP.



(b) Rebar cage ready to cast concrete.

Figure 2-24. GGSS-CIP specimen details and rebar cage.



Figure 2-25. GGSS-CIP rebar cage inside concrete form.



Figure 2-26. GGSS-CIP in final position.

## 2.3 Column-to-Cap Beam Connections

All four specimens in this category had identical geometric properties and similar detailing of the plastic hinge region. Differences included alterations in FGSS location, either inside the column or inside the cap beam, in addition to debonded length of rebar that only applies to the third test specimen, i.e. FGSS-3. The last specimen—FGSS-CIP— simply did not have any FGSS, for it served as the control test specimen.

The GSS used to build the precast models in this category was referred to as FGSS earlier in this report, denoting the existence of a fastened rebar to the factory-end of the FGSS. In other words, the rebar was threaded to one end earlier during the construction of rebar cages, and the dowel bar protruding from the other precast component was grouted at the other end, while installing the test specimen.

### 2.3.1 FGSS-1

The first specimen studied in this category was comprised of a precast column with FGSS embedded in the column end, and a precast cap beam with 7-in. projected dowel bars.

Column longitudinal bars were fastened to the threaded end of the FGSSs, in the first step of the construction phase. All bars were hand-tightened initially, which took about 4 turns, then tightened up by means of a pipe wrench. A form mounting fixture was implemented to fasten the FGSSs to a wooden template to arrange column bars in the desired configuration. A No. 4 spiral with a pitch of 2.5 in. was used to confine the column longitudinal bars. The spiral over the FGSS region had a 1 5/8-in. larger diameter than the spiral for the rest of the columns, due to a larger diameter of the FGSS compared to column longitudinal rebar. This resulted in an overlapping spiral region right above the FGSS.

The cap beam was built similar to the footing, in which the circular joint core was first constructed by tying the hooked dowel bars to a spiral of equal diameter as the column spiral. The tails of these bars were 2 ft-4 in. long, pointed inward to comply with the design code and provide a stable joint core. **Figure 2-27** shows the precast components under construction.



(a) Column end FGSS and overlapping spiral.



(b) Cap beam dowel bars with inward tails.

Figure 2-27. FGSS-1 precast components under construction.

Tie wires were used extensively to achieve a sturdy rebar cage in order for the cages not to become distorted during transportation to the precast plant for casting concrete. Details of specimen FGSS-1 are presented in **Figure 2-28** and the final rebar cages making up the test model are shown in **Figure 2-29**.

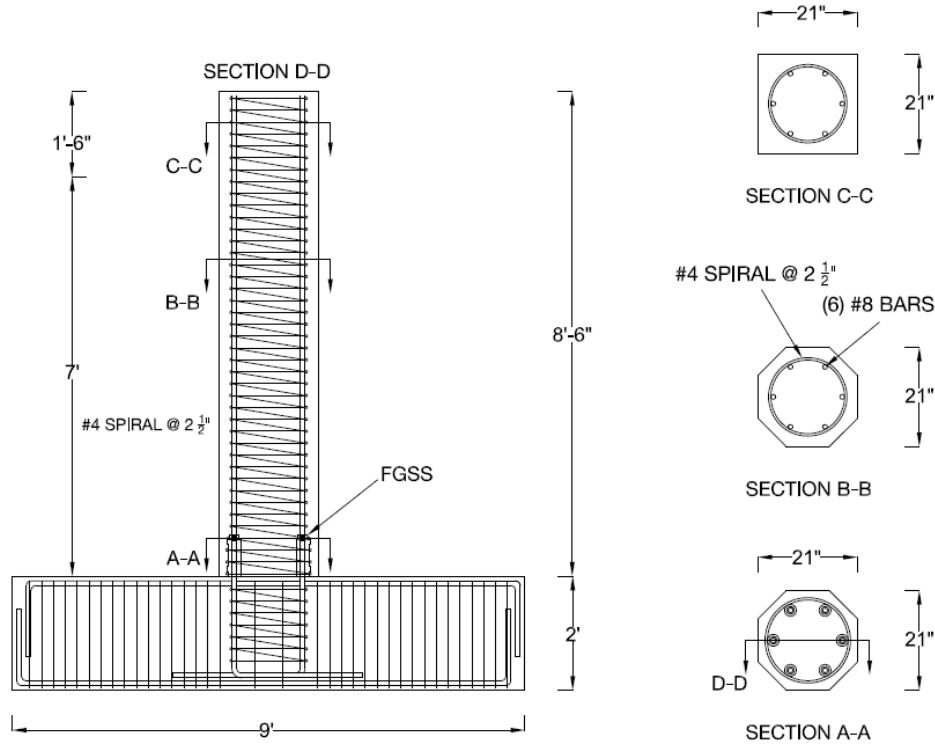


Figure 2-28. Details of FGSS-1.



(a) Column rebar cage.



(b) Cap beam rebar cage.

Figure 2-29. FGSS-1 rebar cage.

The dowel bars protruding from the cap beam in **Figure 2-29** were left considerably longer than required before casting the concrete. This was mainly done to keep the joint core plumb and sturdy using two wooden templates on the dowel bars. These bars were cut to the required length of 7 in. right before assembling the precast components.

Concrete was cast in a highly supervised condition to avoid introducing damage to the instrumentation. 1 ½" PVC pipes were positioned inside the cap beam form to accommodate the interior support rods that were going to be used in fastening the specimen to the test frame. Several 4 in. x 8 in. concrete cylinders were prepared to obtain the compressive strength of

concrete at specified time intervals before the experiment. **Figure 2-30** displays the FGSS-1 precast components inside the formwork before pouring concrete. The 28-day compressive strength of this concrete was 5.3 ksi.

The precast concrete components were removed from the forms once the compressive strength of the concrete reached 3 ksi and were transported back to the Structures Laboratory, where the experiments were conducted. The last step before conducting the tests was to install the precast components and grout the FGSSs and interface. A proprietary high strength and ready-to-mix grout, exclusively formulated to be used with this particular type of GSS was used in accordance with the instructions in the FGSS manual. A single 50-lb bag of grout mixed with 0.7 gallons of water was sufficient to fill up all six FGSSs and cast the bed grout. The grouting operation was very similar to the procedure undertaken for the column-to-footing connections. An electric mixer with a Jiffler paddle was utilized to continuously mix the grout with water, for 5 minutes. The flow test carried out after mixing indicated that the grout had a good consistency with an acceptable spread diameter of 5 in. In general, this grout had



Figure 2-30. FGSS-1 precast components inside concrete forms.

less fluidity than the one used for the GGSS specimens, therefore the grouting operation was relatively more cumbersome. **Figure 2-31** shows the precast components during the grout operation, where a wooden dam was built on the cap beam to facilitate casting of the ¼-in. bed grout.

The column was lowered slowly and dowel bars were inserted into the corresponding FGSS. As described for the previous test specimens, a hand pump was utilized to pump the grout into the FGSS bottom port. Both inlet and outlet ports were plugged when the FGSS was completely filled with grout. 2-in. grout cubes were made to obtain the compressive strength of the grout at desirable time intervals.

FGSS-1 remained connected to the test frame until the grout developed sufficient strength. In the meantime, test preparations were performed. This specimen is displayed in **Figure 2-32** in the final position after the grouting operation; note that this configuration was tested with the cap beam in the inverted position for ease of testing. The average compressive strength of the grout at 28 days was 12.5 ksi.

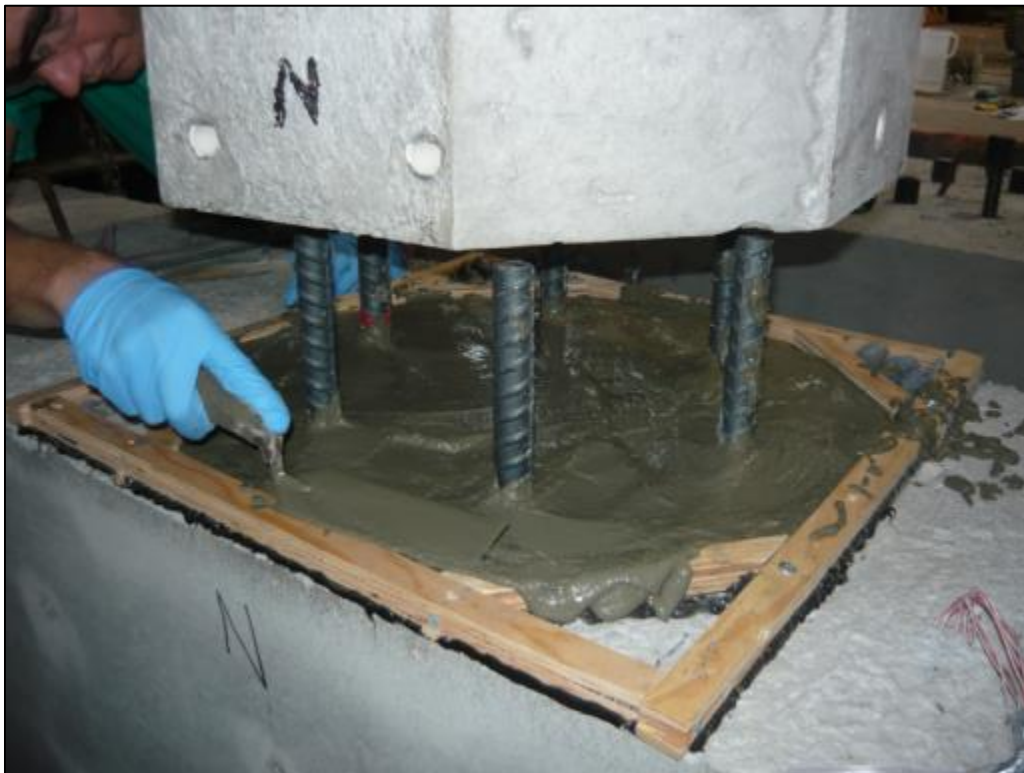


Figure 2-31. Grouting operation for FGSS-1.

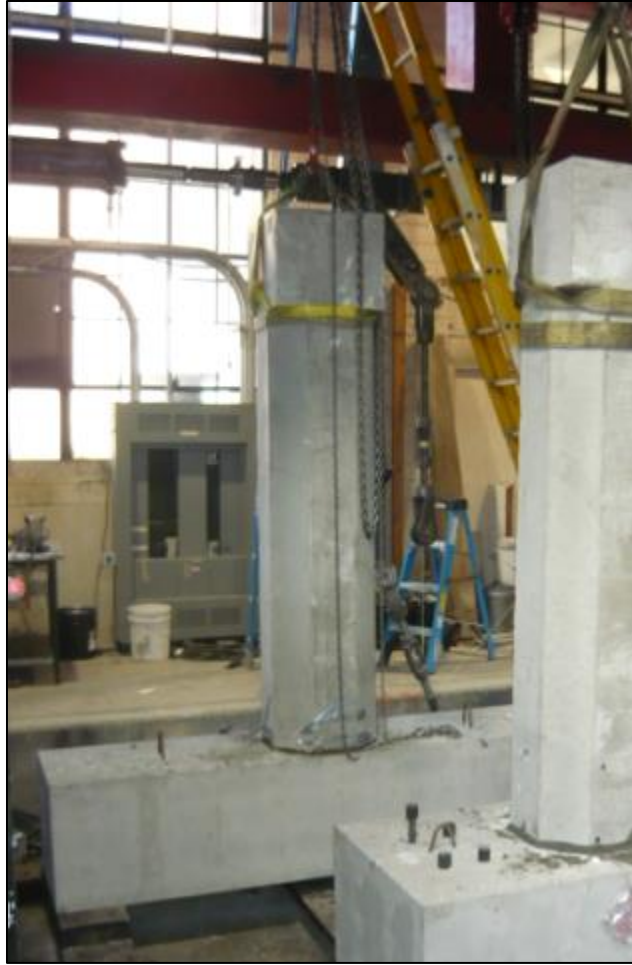


Figure 2-32. FGSS-1 (far behind) in final position.

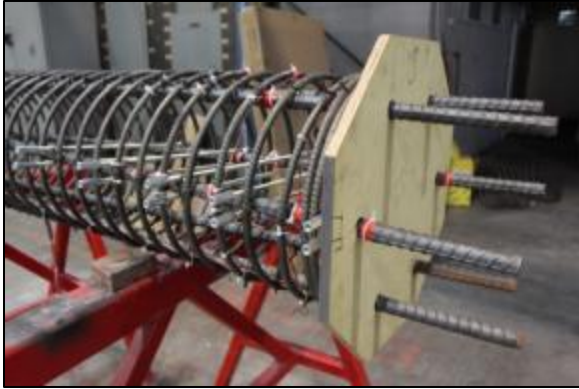
### 2.3.2 FGSS-2

The location of the FGSS was changed from the column end to the cap beam for this specimen. This was equivalent to the second alternative described in the previous section for the column-to-footing connection GGSS-2. Such a change in the connection of the two precast components would make it conform to the design code because the FGSS would not be in the plastic hinge zone of the column. Another significant reason for examining this alternative was to investigate the performance of this test specimen in which the disruption to the plastic hinge region of the column was reduced with respect to FGSS-1. Such a connection configuration was successfully implemented in the Provo to Salt Lake Frontrunner rail bridge construction, using a different GGS.

The precast column rebar cage was built first. Six No. 8 bars in a circular arrangement were confined by a No. 4 spiral with a pitch of 2.5 in. Dowel bars 7-in. long protruded from the column end, as shown in **Figure 2-33(a)**. The joint core was built and centered in the cap beam. Threaded hooked bars were previously tightened on the FGSS by means of a pipe wrench, and arranged in a circular fashion using a template. Horizontal joint reinforcement consisting of a closely spaced spiral was tied to both the vertical hooked bars and the FGSS, as shown in **Figure 2-33(b)**. Tails of the hooked bars were oriented into the joint core, and had a length of 2 ft-4 in.

Tie wires were used extensively to secure the joint core and thus, minimize the likelihood of a mismatch between the column and the cap beam. FGSS-2, like all other specimens, was transported to the precast plant for casting of the concrete. General details of the test specimen are provided in **Figure 2-34**, which depicts the dimensions, arrangement of reinforcing bars, and sectional properties.

The rebar cages that formed this specimen are shown in **Figure 2-35**. Double hoops used in the cap beam were uniformly distributed along the beam, and top and bottom layers of rebar were tied to double hoops. The entire shear reinforcement in the cap beam had seismic detailing in accordance with the design code [16].



(a) Column rebar cage with projecting bars.



(b) FGSS placed within cap beam.

Figure 2-33. FGSS-2 precast components under construction.

Concrete was cast and several 4 in. x 8 in. cylinders were made from the same batch. These cylinders were used to obtain the concrete compressive strength at several times, such as lifting of the components from the concrete forms, 28-day strength, and on the test day. 1 1/2" PVC pipes were located in designated spots for support rods that would be used to secure the test specimen in the test frame. **Figure 2-36** shows the FGSS-2 precast components in the

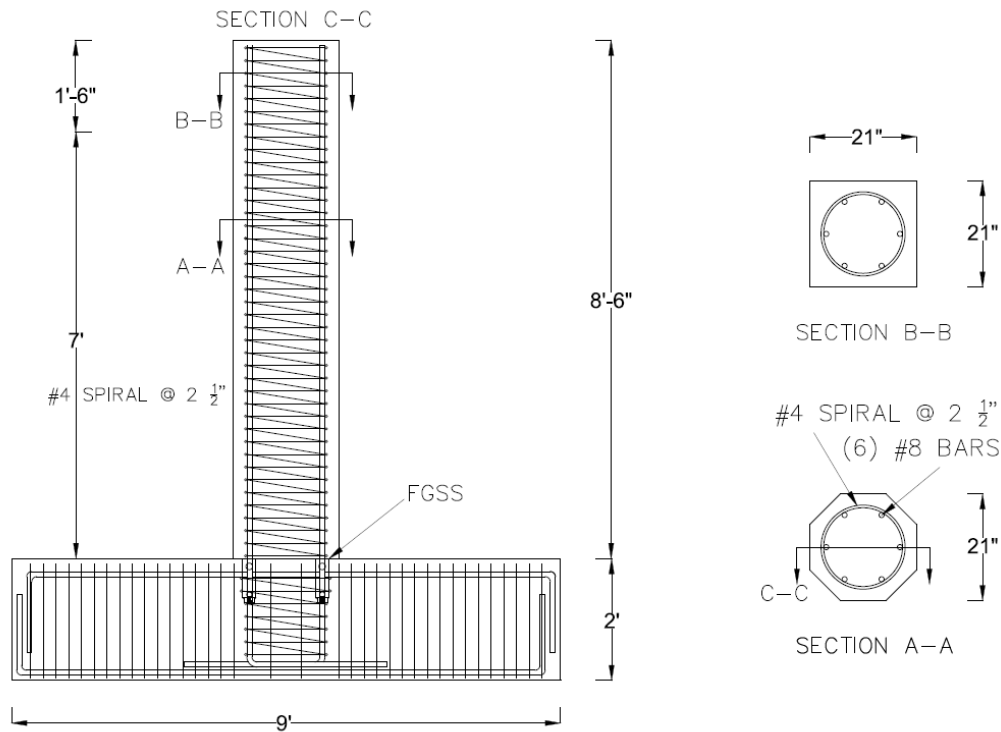


Figure 2-34. Details of FGSS-2.

forms. The average compressive strength of the concrete was 3.9 ksi at 28 days.

The precast components were removed from the forms when the concrete compressive strength reached 3 ksi. The grouting operation procedure was carried out as described FGSS-1. The flow test showed an acceptable grout consistency with a spread diameter of 5.25 in, although it was hard to pump the grout with the Kenrich GP-2HD hand pump which was used for this purpose. As opposed to the post-grout procedure followed for FGSS-1, in which the grout was pumped into each FGSS against the gravity, a pre-grout technique was carried out in a similar approach to specimen GGSS-2. This was done to facilitate the installation process. To perform a pre-grout operation, both inlet and outlet port of all FGSSs were sealed during construction of



(a) Column rebar cage.



(b) Cap beam rebar cage.

Figure 2-35. FGSS-2 rebar cages.



Figure 2-36. FGSS-2 precast components inside concrete forms.

the rebar cages. During installation, all FGSSs were filled with grout from the wide end opening, as shown in **Figure 2-37**. Grout cubes were made to obtain the 28-day and test-day compressive strength of the grout.

When all six FGSSs were filled, grout was cast at the interface of the precast members.  $\frac{1}{4}$ -in. spacers were placed at the interface to achieve a desirable bed grout thickness. The column was gently set down into position and braced temporarily to prevent movement until the grout developed sufficient strength.

Compression tests on grout cubes indicated that the 28-day compressive strength of the FGSS-2 grout was 10.3 ksi—the lowest grout strength among all column-to-cap beam and column-to-footing specimens. **Figure 2-38** shows this specimen fastened to the test frame in the Structures Laboratory.



Figure 2-37. Grouting operation for FGSS-2.



Figure 2-38. FGSS-2 in final position.

### 2.3.3 FGSS-3

This test specimen had nearly the same characteristics as FGSS-1 in terms of dimensions, steel reinforcement configuration, and location of the FGSS. The key difference between the two specimens was only a deliberate and localized debonding implemented on an 8-in. portion of the cap beam dowel bars right below the column-to-cap beam interface. Two layers of duct tape were wrapped around the designated rebar region to ensure there was no bond between the rebar and concrete as shown in **Figure 2-39**.

The main objective of the intentional rebar debonding was to provide a better strain distribution along the critical region which was outside the FGSS, within the cap beam. This would reduce the strain concentration over the short length around the column-to-cap beam interface, thus premature rebar fracture would be delayed. The 8-in. debonded length was obtained by subtracting the required development length of a hooked rebar from the available depth in the cap beam. This was carried out in accordance with the AASHTO LRFD Bridge

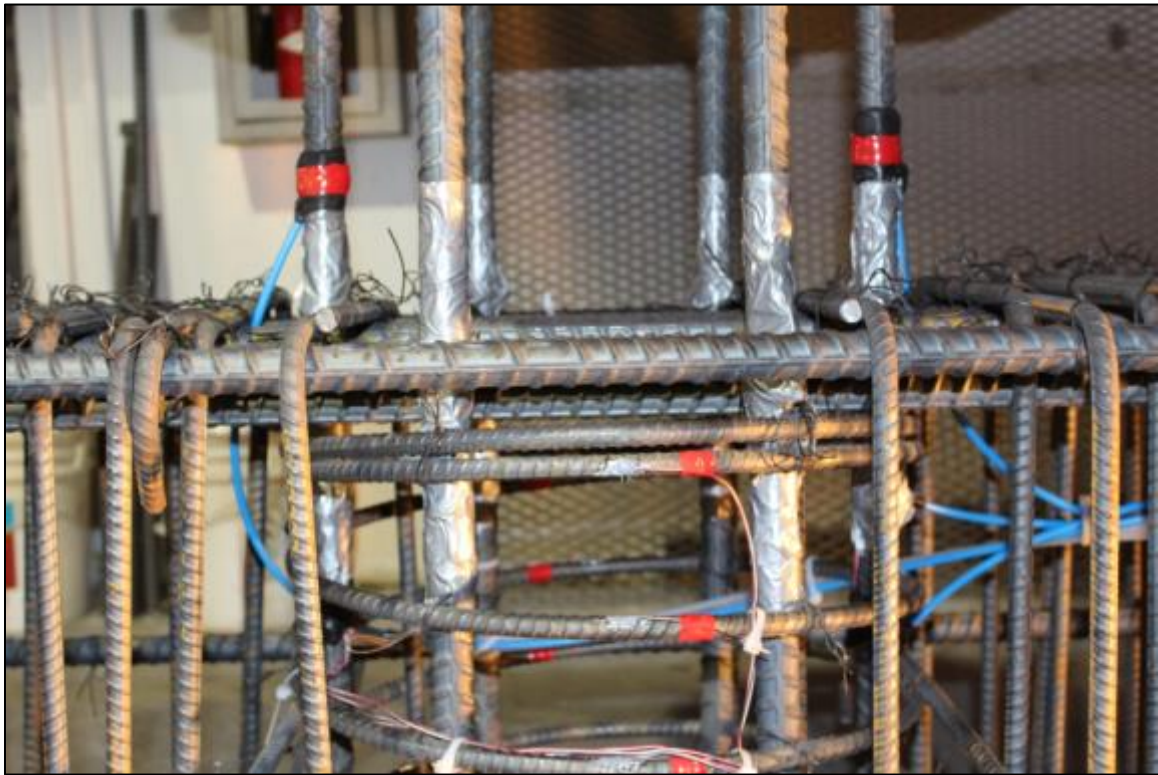


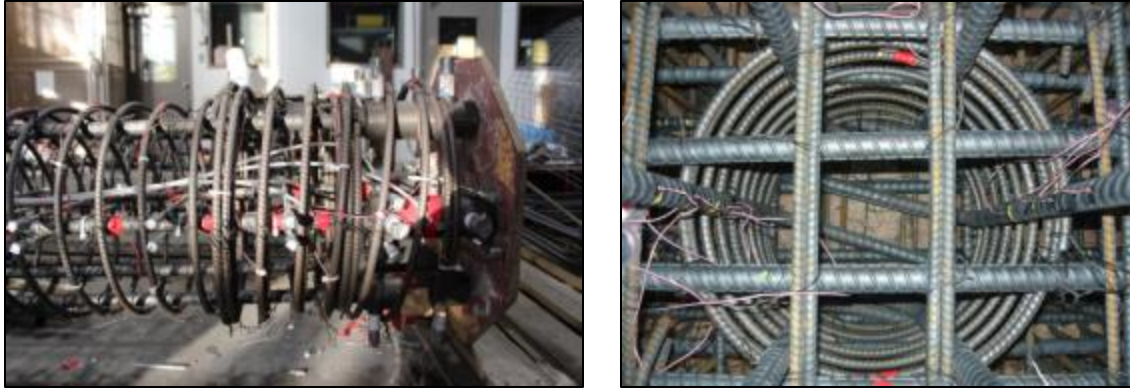
Figure 2-39. Debonded region of the dowel bars for FGSS-3.

Design Specifications, although the AASHTO-Seismic Code inhibits a reduced anchorage length even if standard hooks are incorporated. The basic development length requirement was used, as shown in Equation (1), along with pertinent modification factors, as discussed in **Section 2.2.3** for specimen GGSS-3.

Column longitudinal bars were fastened to the threaded end of the FGSSs, in the first step during the construction phase. Bars became hand-tight initially which took 4 turns and then tightened up by means of a pipe wrench. Next, the form mounting fixtures previously used for FGSS-1 and FGSS-2 were cleaned and reused to fasten the FGSSs to the wooden template to arrange the column bars in the desired configuration. A No. 4 spiral with a pitch of 2.5 in. was used to confine the column longitudinal bars. The spiral used over the FGSS region had a 1 5/8-in. larger diameter than the spiral for the rest of the columns, due to the larger diameter of the FGSS compared to column longitudinal rebar. This resulted in an overlapping spiral region right above the FGSS.

The cap beam was built in a similar approach to the first test specimen in the column-to-cap beam category, i.e. FGSS-1. **Figure 2-40** shows the precast components under construction. The details of test specimen FGSS-3 are illustrated in **Figure 2-41** and the rebar cages for the precast components are shown in **Figure 2-42**. The dowel bar length was left considerably longer than needed before casting the concrete in order to keep the cap beam rebar core as sturdy as possible. All dowel bars were cut to length by a grinder before the grouting operation.

Several 4 in. x 8 in. cylinders were made following ASTM C39, for future investigation of the concrete compressive strength. Eight 1 1/2" PVC pipes were positioned inside the cap beam rebar cage to accommodate the interior support rods and eventually fasten the test specimen to the test frame. **Figure 2-43** shows the FGSS-3 column and cap beam rebar cages in concrete forms, before concrete was cast. The average concrete compressive strength at 28 days was 6.7 ksi. The precast components were taken out of the forms when the concrete had reached a compressive strength of 3 ksi. The grouting operation was carried out to connect the two pieces together in the Structures Laboratory as described in Section 2.3.1 for FGSS-1. The column is shown in **Figure 2-44** prior to the grouting operation, with the FGSSs embedded inside the bottom part. The inlet and outlet ports of the FGSS used to pump the grout into the sleeves are also visible on



(a) Column end FGSS and overlapping spiral. (b) Cap beam joint core- top view.

Figure 2-40. FGSS-3 precast components under construction.

the surface of the column. 2-in. grout cubes were made to obtain the compressive strength of the grout at 28 days in addition to the test day.

One temporary brace was sufficient to maintain the column plumb within an acceptable tolerance, as shown in **Figure 2-45**. This specimen remained attached to the test frame for 28

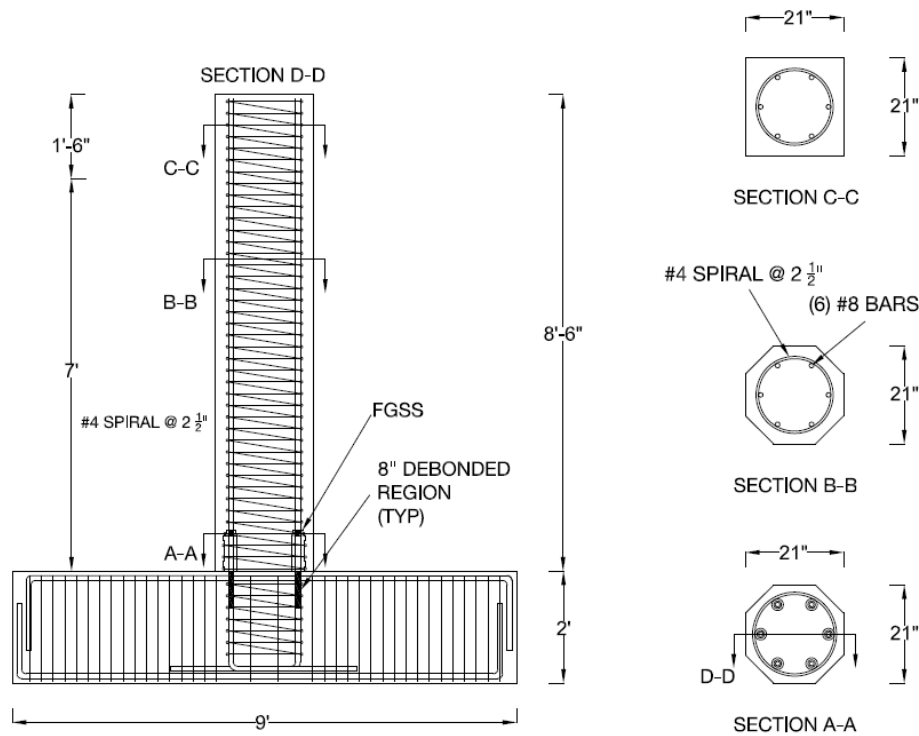


Figure 2-41. Details of FGSS-3



(a) Column rebar cage.



(b) Cap beam rebar cage.

Figure 2-42. FGSS-3 rebar cages.



Figure 2-43. FGSS-3 precast components inside concrete forms.

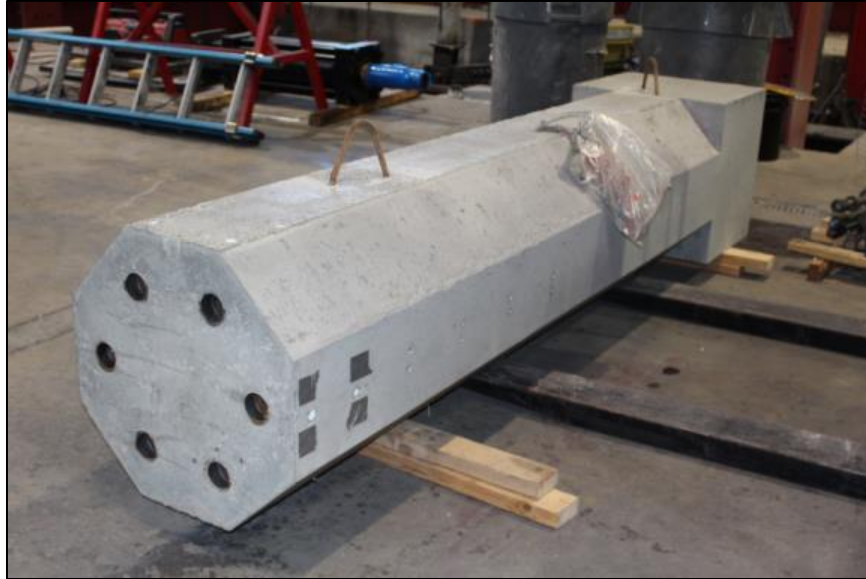


Figure 2-44. FGSS-3 precast column before grouting operation.

days to cure the grout to cure and allow it to reach maximum strength. The average compressive strength of the grout at 28 days was 10.6 ksi.



Figure 2-45. FGSS-3 in the final position.

#### 2.3.4 FGSS-CIP

FGSS-CIP was the control specimen in the column-to-cap beam connection category. It represents a monolithic construction without any FGSS to splice the reinforcement. The results from all experimental tests on precast column-cap beam connections are compared to the test results for the FGSS-CIP, in coming chapters. The spiral reinforcement did not have any splice either, confining the core concrete from top of the column monolithically down to the bottom of the cap beam, as a single long helical reinforcement around the longitudinal bars. The diameter of the spiral was kept the same as for the spiral around the column bars in the other three test models, thus ensuring an identical moment arm for column longitudinal bars in all specimens.

Construction of this specimen began with building the column rebar cage by using the same wooden template as in the previous specimens. The column longitudinal bars were tied to the spiral at every corner from the bottom towards the column top. Tails of the column hooked bars were 2 ft-4 in. long and were bent inward to comply with the design code and achieve a sturdy base for the column rebar cage during construction. Once the column was completed, it was placed on the cap beam bottom reinforcement that was already positioned properly. The tails of the column rebar were then tied to the cap beam bottom reinforcement. Subsequently, cap beam double hoops, top reinforcement, and middle bars were added to complete the rebar cage. **Figure 2-46** shows the joint area during the construction stage, and **Figure 2-47** demonstrates the details of the FGSS-CIP and finalized rebar cage for this specimen.

The constructed rebar cage was transported to the precast plant to cast the concrete. **Figure 2-48** shows this monolithic component sitting in the concrete form prior to casting. Several 4 in. x 8 in. cylinders were made to obtain the concrete compressive strength at different time intervals including before removal of the specimen from the form, at 28 days, and on test day. As presented in **Figure 2-48**, 1 ½" PVC tubes were embedded inside the cap beam cage in order to fasten the specimen to the test frame. The average concrete compressive strength was 5.2 ksi at 28 days.

FGSS-CIP was taken out from the form and transported back to the Structures Laboratory once the concrete strength had reached 3 ksi. The specimen was fastened to the test frame while

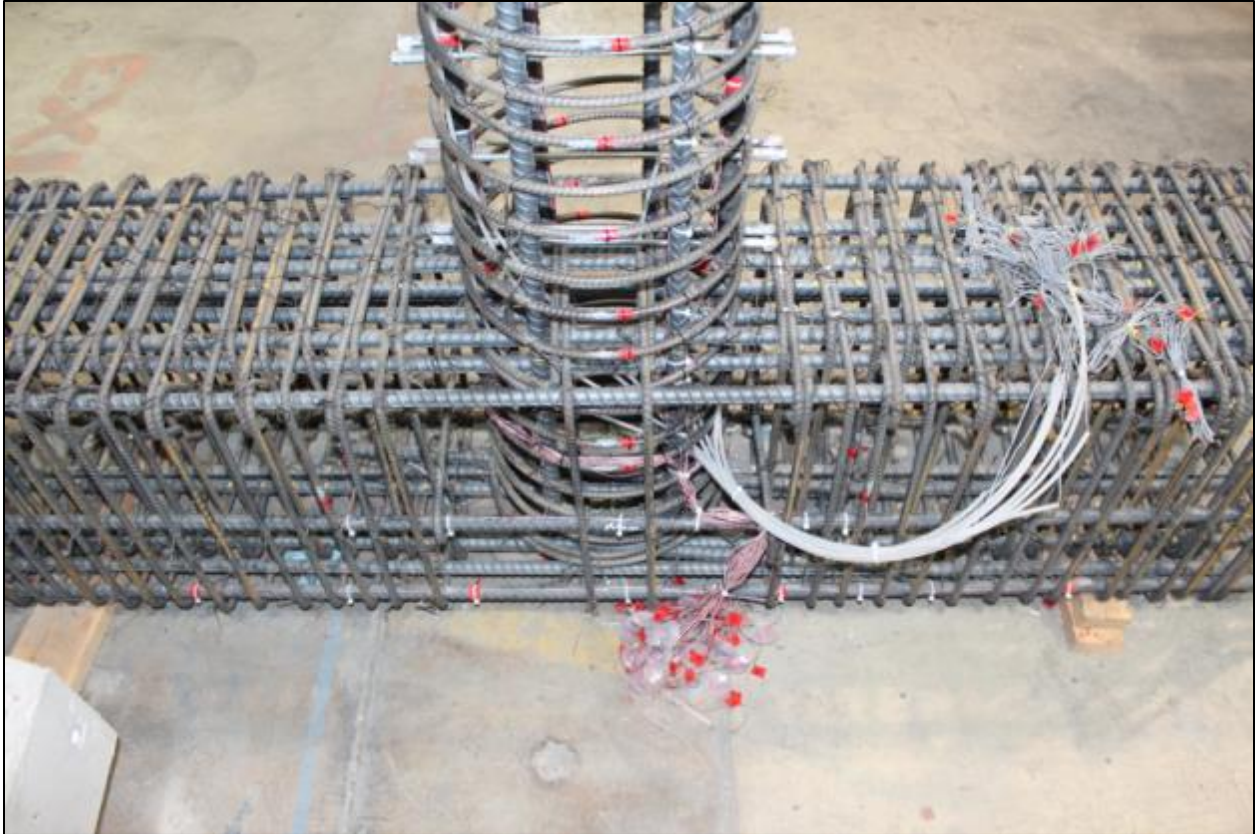
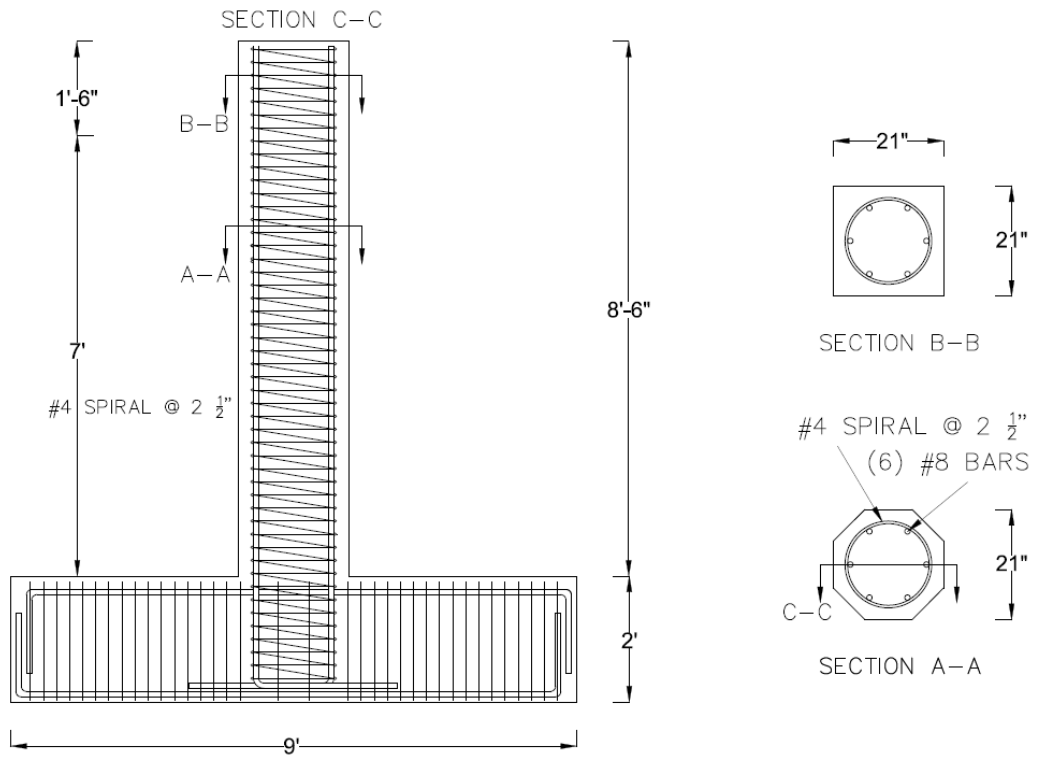


Figure 2-46. FGSS-CIP joint area.

test preparation procedures were implemented. **Figure 2-49** displays the test specimen in the final testing position.



(a) Details of FGSS-CIP.



(b) Rebar cage ready to cast concrete.

Figure 2-47. FGSS-CIP specimen detail and rebar cage.



Figure 2-48. FGSS-CIP rebar cage inside concrete form.



Figure 2-49. FGSS-CIP in final position.

### **3.0 TEST PROCEDURE**

This chapter covers the required steps taken to develop the testing program, and methods implemented to monitor the response and capture the test results. Details of the instrumentation types and locations are included, along with a description of test setup and lateral displacement history applied to the specimens.

#### **3.1 Instrumentation**

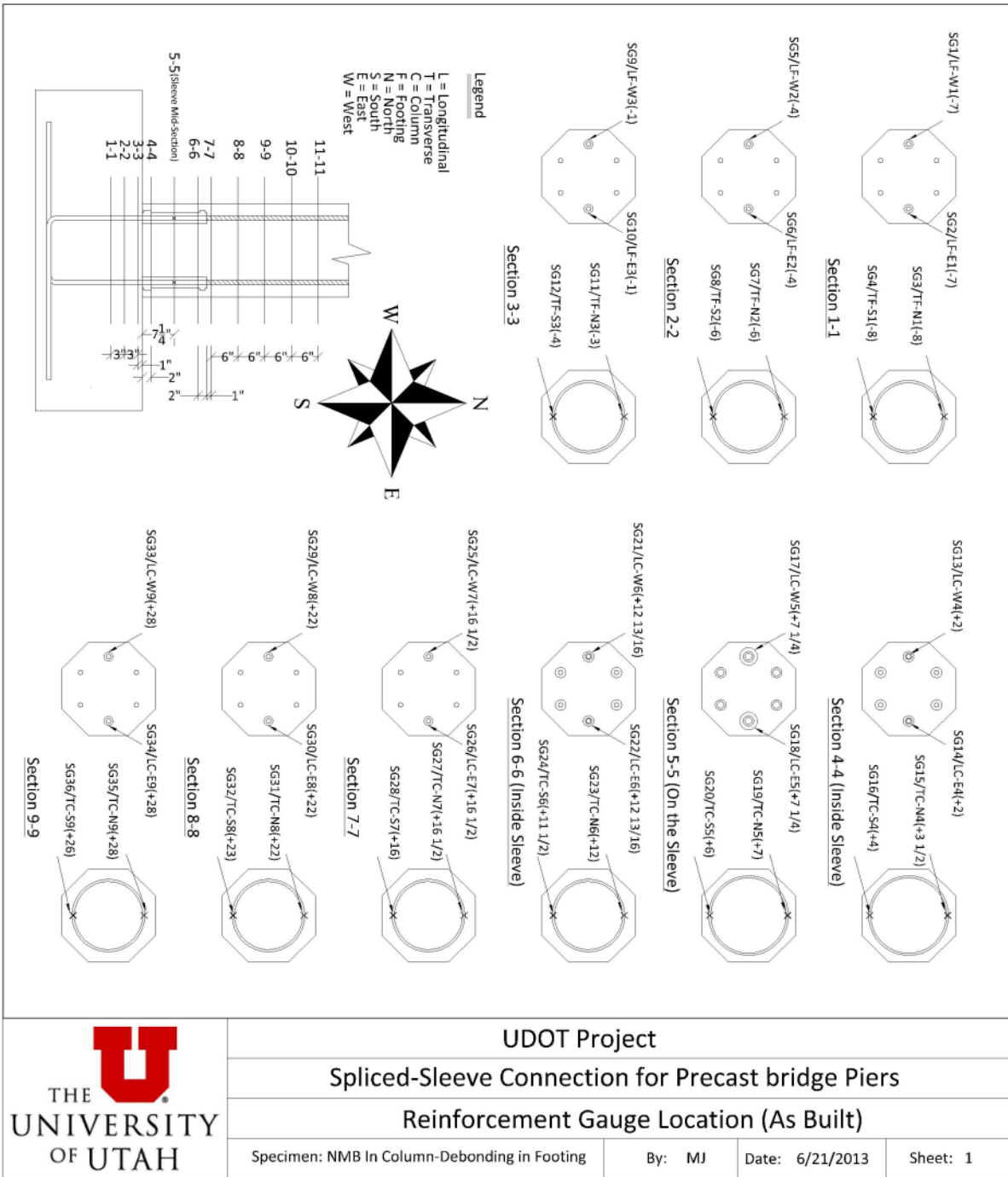
Various types of instrumentation were used to obtain the test results and help understand the overall performance. This section includes discussions on the application of strain gauges, string potentiometers, and Linear Variable Differential Transformers (LVDT).

##### **3.1.1 Strain Gauges**

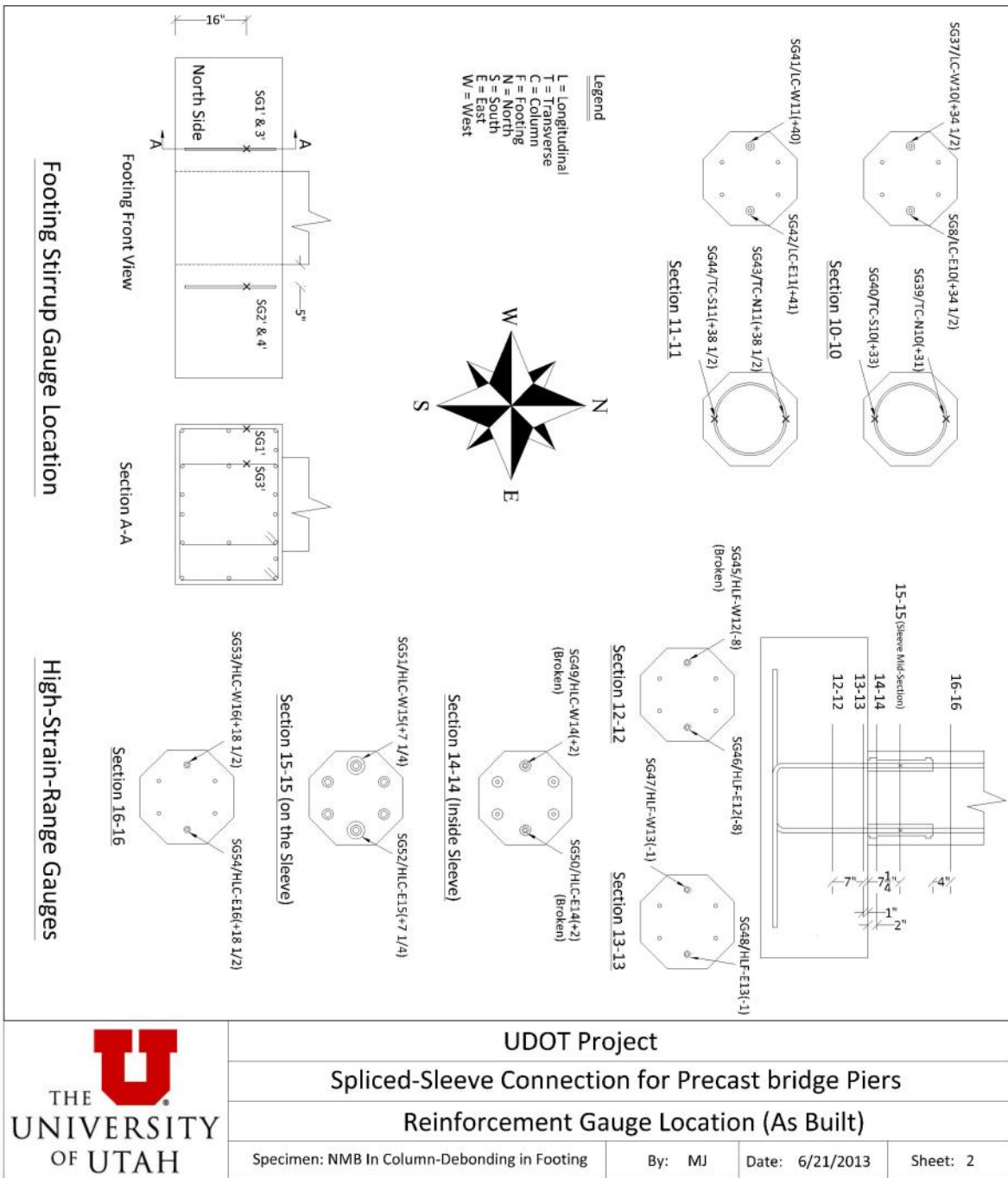
Test specimens were instrumented with several strain gauges especially in the plastic hinge region and the joint area, where maximum demand was anticipated to occur. These gauges were installed on longitudinal and transverse reinforcement to capture the strain levels during the test. For the precast test models, strain gauges were placed on the GSS middle section to obtain the induced strain values on the sleeves.

Strain gauges were mostly attached to the two longitudinal bars located farthest from the centerline of the column, to characterize the maximum strain conditions. In most of the tests, strain gauges were also applied to such bars for the portion grouted inside the GSS at a section located 2 in. from the GSS ends. The objective was to determine when these bars would yield.

A sample of a typical strain gauge layout is shown in **Figure 3-1**. This layout includes the location, designation, and type of strain gauge used at each specific section. It is noted that only the two extreme longitudinal reinforcing bars were gauged in each section and only two strain gauges were placed on the corresponding spiral section, for specimen GGSS-3.



(a) Sample strain gauge layout-part 1.



(b) Sample strain gauge layout-part 2.

Figure 3-1. Strain gauge layout for GGSS-3.

A detailed step-by-step procedure was followed for surface preparation, attachment of strain gauges, and protection from debris and further damage that was likely to be caused by the surrounding concrete. **Figure 3-2** displays the strain gauges placed on the spiral and longitudinal rebar during the last phase of construction for GGSS-3. Wires were carefully routed towards a point in the middle of the footing where significant damage was unlikely to occur. **Figure 3-3** shows the strain gauges on the joint spiral and longitudinal rebar for FGSS-3. Strain gauge wires were protected inside the hollow flexible plastic blue tubes.

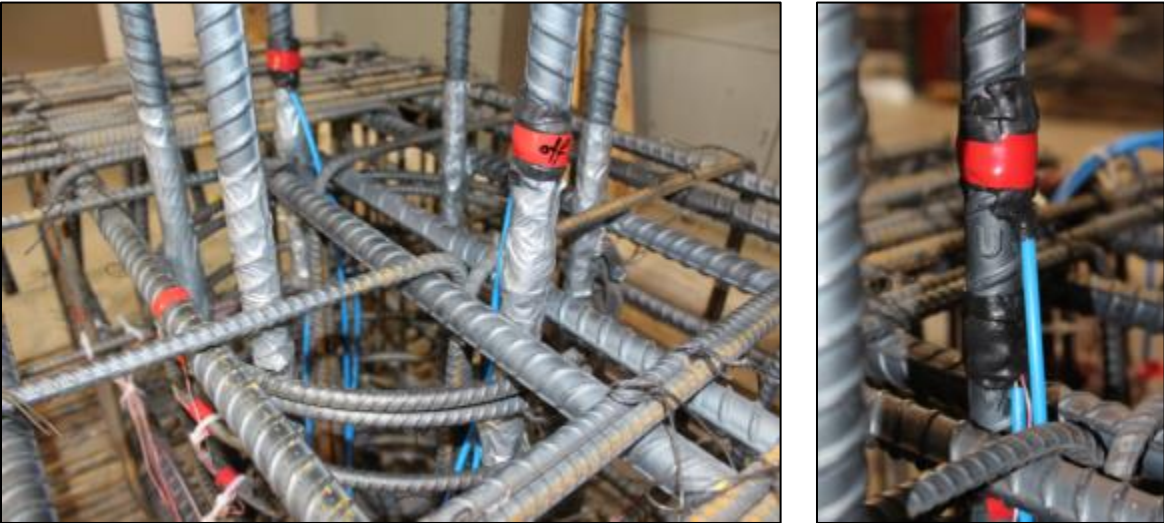


Figure 3-2. Strain gauges on GGSS-3.

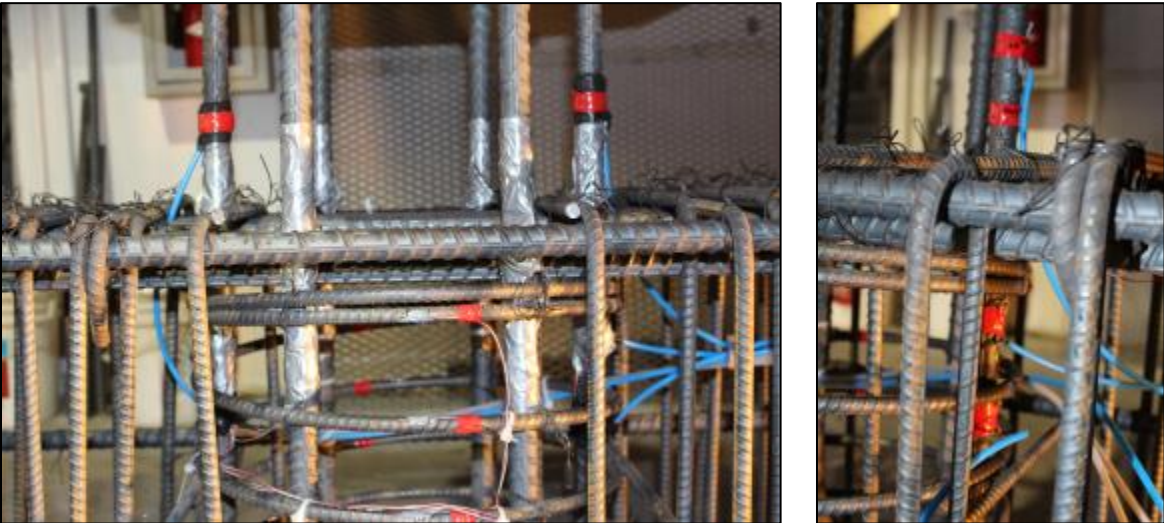


Figure 3-3. Strain gauges on FGSS-3.

### 3.1.2 String Potentiometers

Two string potentiometers were used to measure the column displacements during the test. They were both attached to the column head at an elevation equal to the height of the center of the actuator. The two string potentiometers were oriented in the opposite direction. Column displacements were obtained by taking the average of the readings collected from these potentiometers. Force-displacement figures were constructed utilizing the results from this instrumentation. Readings from the string potentiometers provided information for further indirect analyses, such as discussions on energy dissipation capacity for the test specimens.

**Figure 3-4** shows the west string potentiometer installed on GGSS-3.

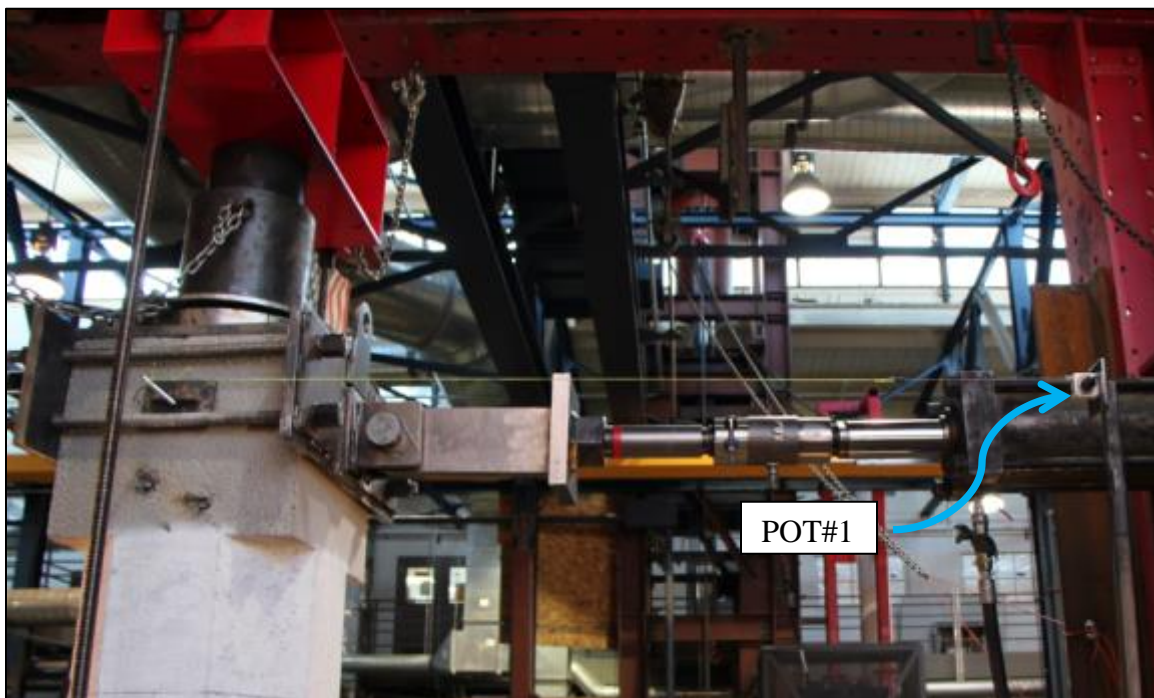


Figure 3-4. String potentiometer on west side of specimen GGSS-3.

### 3.1.3 Linear Variable Differential Transformers

Linear Variable Differential Transformers (LVDTs) were used to study the curvature distribution along the column end, obtain the base rotation capacity and characterize bond-slip rotation, and verify the global vertical and horizontal movements of the test specimens.

Ten LVDTs were mounted to the column end, over an approximately 30-in. region, to measure the relative vertical displacements between the sections and provide data for curvature analysis. Column base rotation and subsequent bond-slip rotation were studied using the lowest pair of LVDTs on the column end, or LVDT 1 and 2 as illustrated in **Figure 3-5** for the column-to-footing connections. Other LVDTs were used to compute the curvature capacity along the column end. The LVDT configuration was similar for the column-to-cap beam connections.

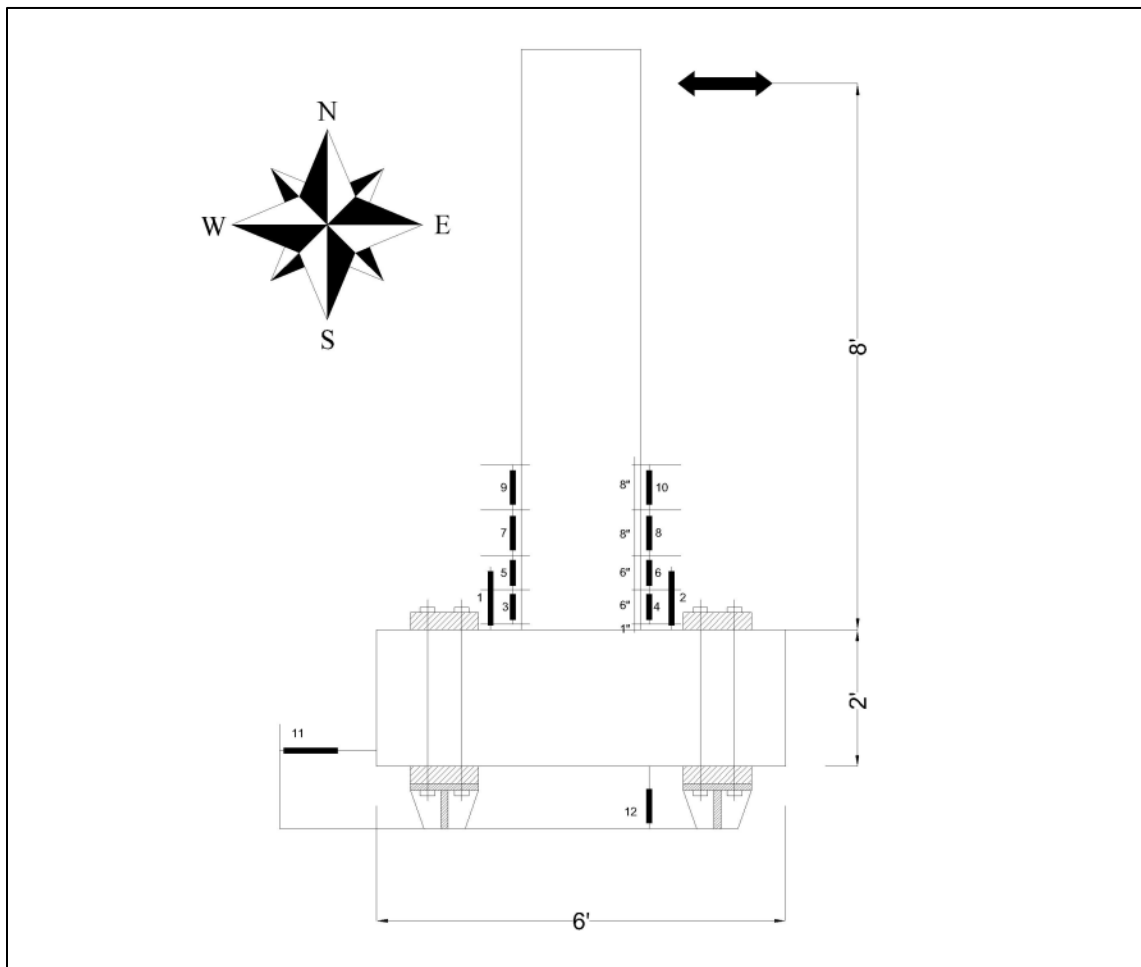


Figure 3-5. LVDT configuration for column-to-footing connections

Using 1 ½-in. steel angles and spherical rod ends, these LVDTs were fastened to 3/8-in. diameter all-thread rods which were embedded in the column core. **Figure 3-6(a)** shows the all-thread rods placed inside the column cage, while **Figure 3-6(b)** displays the LVDTs mounted on the column end before the test. Four sets of LVDTs were used to create four curvature segments over which the curvature was assumed to be constant. The segment height was specified to be 6 in. for the bottom two curvature segments and 8 in. for the top two curvature segments. This was determined in accordance with the stroke capacity of the LVDTs along with the predicted curvature demands in the particular segment. A preliminary sectional analysis had been conducted to estimate the ultimate curvature capacity of the critical section for a monolithic connection, as discussed in **Section 2.1**. The predicted ultimate curvature was then converted into a predicted ultimate strain in the critical column segment. The maximum LVDT stroke along with a proper segment height resulted in the selection of a desired LVDT configuration for all curvature segments.



(a) LVDT all-thread rods attached to rebar cage



(b) LVDTs attached to fixture.

Figure 3-6. LVDTs for curvature analysis.

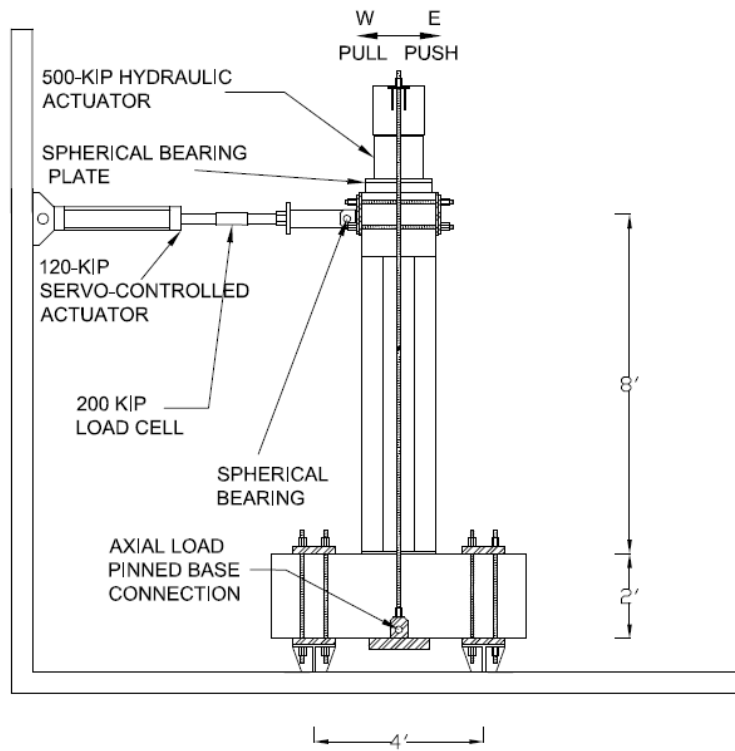
LVDTs 11 and 12 in **Figure 3-5** were only used to verify the test setup and ensure that the test specimen would not undergo unexpected global slippage in the vertical or horizontal direction.

### 3.2 Test Setup

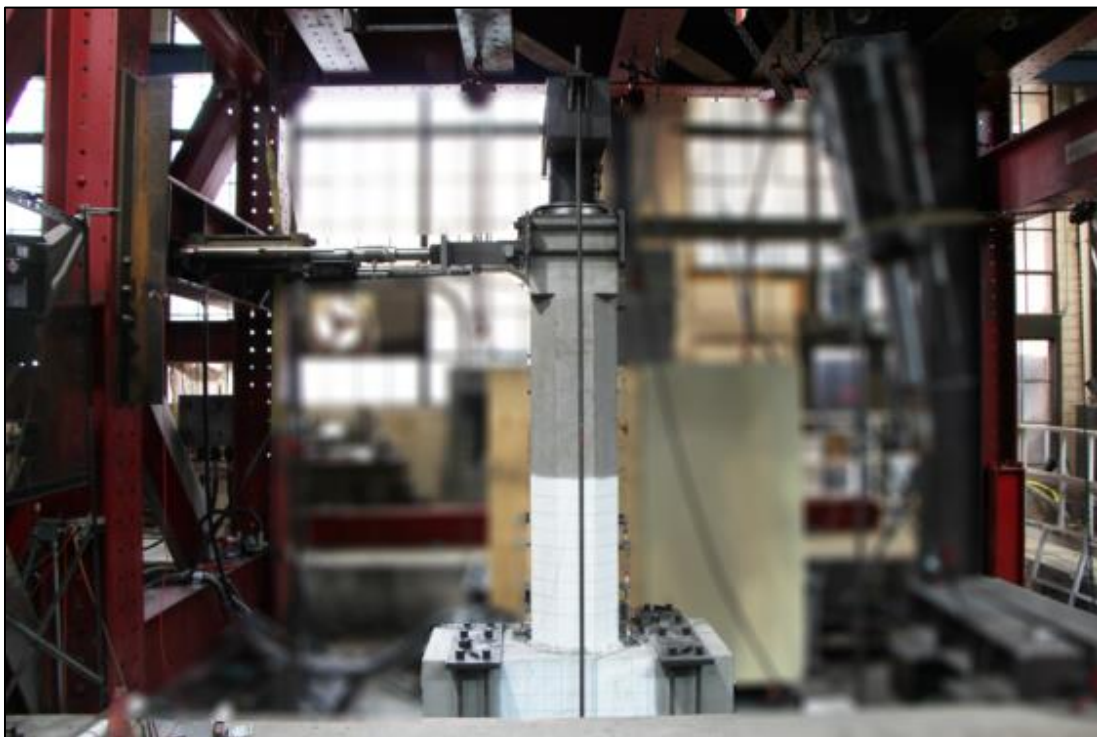
All specimens were tested inside the test frame of the Civil and Environmental Engineering Department Structures Laboratory at the University of Utah. This test frame has a capacity to resist 500 kip in any of the three directions. The column-to-cap beam connections were tested in an inverted condition. Each test specimen was connected to the floor girders by means of 8 high strength all-thread rods on each side, half of which ran through the PVC pipes embedded in the footing (or cap beam), before casting the concrete. The rods were then bolted to 1 ½-in. top and bottom plates to prevent the specimen from moving or slipping during the test. This support condition was designed to provide very limited rotational restraint, and hence represent a hinged support condition.

The axial load application system consisted of a cylindrical 500-kip hydraulic actuator, a 4-ft long stiffened W14x90 spreader beam, a 3-in. thick A36 steel plate, and two 14 ft-6 in. long 150 ksi all-thread rods. The 500-kip actuator rested on the column top and applied a compression force to the steel beam above it, causing the all-thread rods to pull on the steel plate that was underneath the footing (or cap beam). An axial load of 6% of the column axial capacity was applied to simulate the gravity loads that typically present in a bridge column. **Figure 3-7** and **Figure 3-8** include the schematic test setup in addition to the test frame configuration for column-to-footing and column-to-cap beam specimens, respectively.

A 120-kip servo-controlled actuator, with an overall stroke of 18 in. applied the cyclic load to the precast test specimens; however, both of the control specimens were tested using a 250-kip servo-controlled actuator with an overall stroke of 24 in. These hydraulic actuators were powered by an MTS pump with a 3000-psi work load and were used to apply a reversed cyclic quasi-static displacement history to the column as described in the next section.

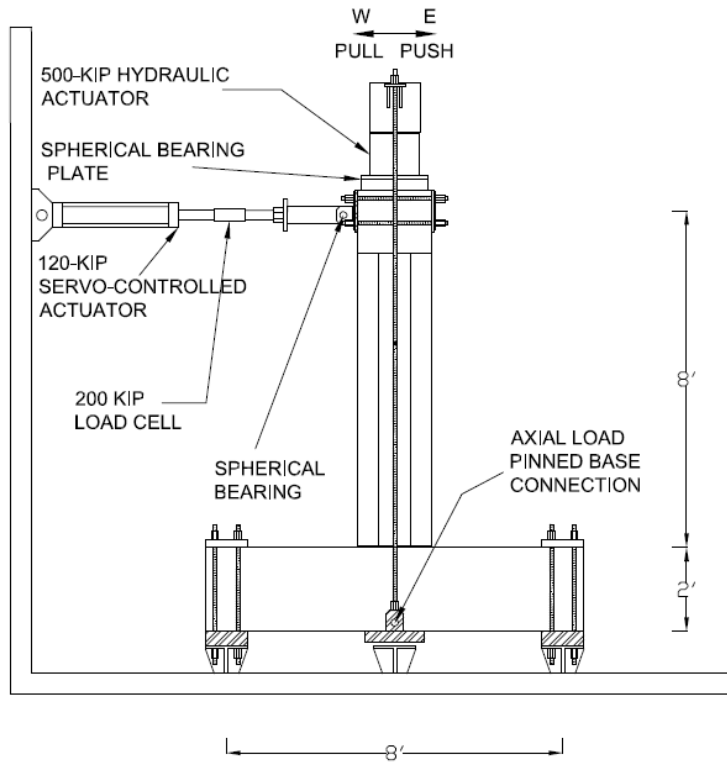


(a) Schematic test setup.

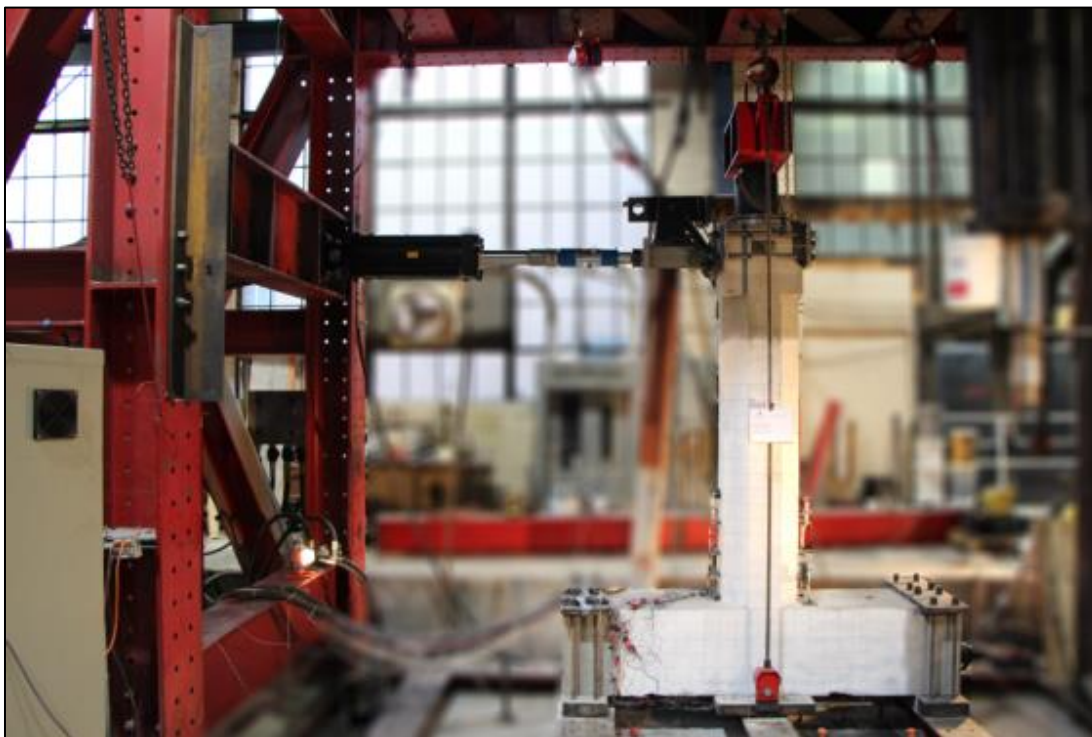


(b) Test setup.

Figure 3-7. Experimental configuration of column-to-footing test specimens.



(a) Schematic test setup.



(b) Test setup.

Figure 3-8. Experimental configuration of column-to-cap beam test specimens.

### 3.3 Displacement History

A reversed cyclic quasi-static displacement-control protocol was applied to the column at an elevation 8 ft above the footing or cap beam, as shown in **Figure 3-7** and **Figure 3-8**. This displacement history was comprised of increasing amplitudes as multiples of the predicted yield displacement of the column [20]. Two cycles were employed for each drift ratio as depicted in **Figure 3-9**. A 5-minute pause was introduced after the completion of each drift ratio, to examine the test specimen and make observations regarding the visible aspects of the response. The displacement rate was set to 1.2 in./min up to the end of the 3-in. drift ratio, after which it was changed to 4 in./min and was kept constant until completion of the test.

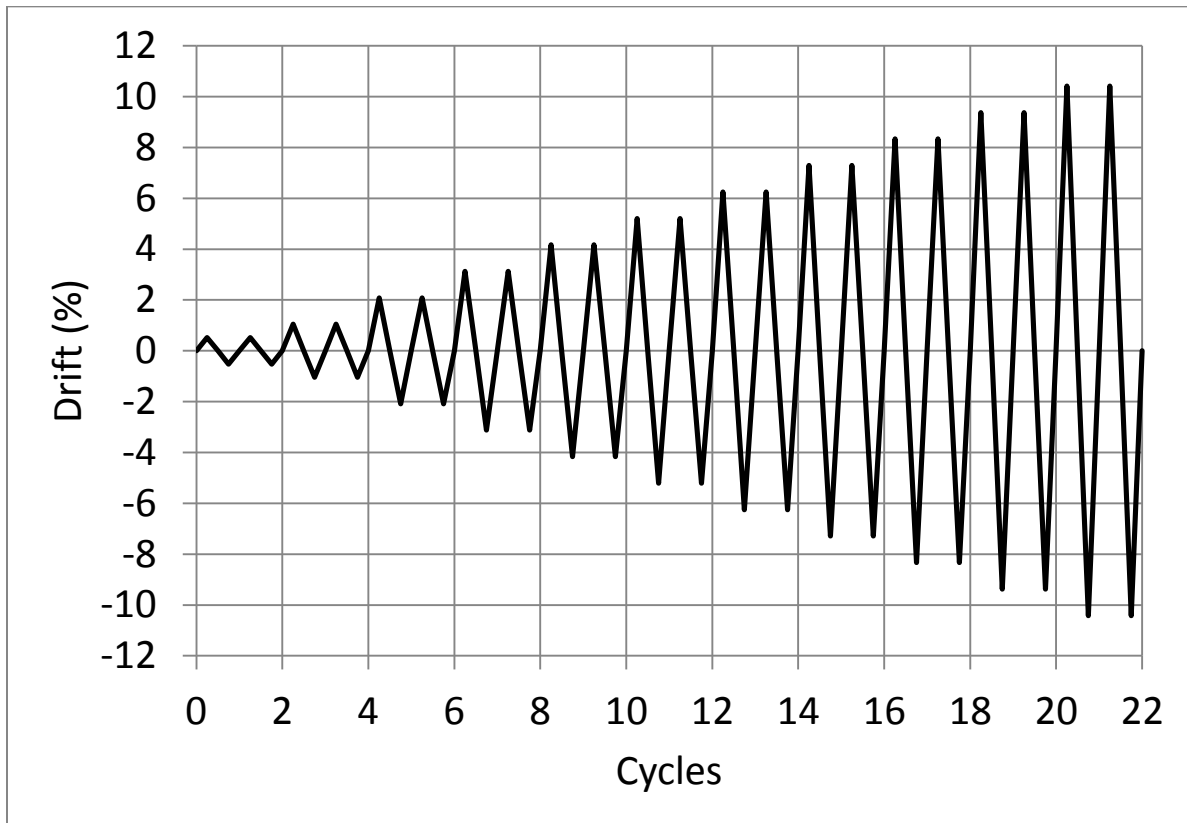


Figure 3-9. Displacement history.

## **4.0 TEST RESULTS**

The measured response of the specimens under applied lateral loading history is discussed in this chapter. Analysis of the measured response of individual tests includes discussions on the visual aspects of the performance; hysteretic behavior; ductility capacity of each test specimen along with a discussion of plastic rotation capacity; energy dissipation capacity; and lastly distribution of curvature along the column. A comparative study is undertaken for each connection category to provide a better assessment of the performance relative to available alternatives and most importantly the control specimen. The comparison includes the lateral force-displacement response; energy dissipation capacity in terms of equivalent viscous damping; cyclic degradation of stiffness; and investigation of the curvature distribution discrepancies among all test specimens.

## 4.1 Analysis of the Response

This section describes the four evaluation methods implemented and presented herein for each test specimen in the following sections.

### 4.1.1 Experimental Observations and Damage States

This section summarizes the visual observations made during the test with respect to damage progression including formation and development of cracks and spalling of concrete. Overall performance of test specimens recorded during the test and captured in photographs is discussed, such as onset of rebar buckling and fracture, or excessive slippage of the spliced bar. Termination of the experiment and failure mode of each test specimen is investigated with the aid of the hysteresis response that was developed for each test. Damage states shown on the hysteresis response graph indicate significant stages of performance. The quality of hysteresis loops along with strength and stiffness degradation are also noted. Select photographs of the specimen are provided to present the state of damage at particular drift ratios. All test specimens were painted white and grid lines divided the concrete surface into 4-in. squares. Different color markers were used to mark the cracks with a displacement level index to identify the crack formation sequence.

### 4.1.2 Displacement Ductility Capacity and Plastic Rotation Capacity

Displacement ductility capacity is considered as the ability of a structural component to perform beyond the yield point without excessive strength deterioration. This parameter was computed for each test specimen based on the concept of equal energy of an idealized elasto-plastic system [21]. The average backbone curve was first constructed using the peak values of the first cycle for each drift ratio. The idealized elasto-plastic curve was then generated in order to calculate the displacement ductility. To obtain the effective yield displacement of the system, it was assumed that the idealized elasto-plastic curve intersects the average backbone curve at a force equal to 70% times the effective yield force. This value was utilized in accordance with the recommendations in the *ACI 374 Guide for Testing Reinforced Concrete Structural Elements under Slowly Applied Simulated Seismic Loads* [20]. The ultimate displacement was taken as the displacement corresponding to a 20% drop in the lateral load capacity [22]. Displacement

ductility was then obtained as the ratio of the ultimate displacement to the yield displacement of the system.

The rotation capacity of each test specimen was assessed by dividing the column-top displacement by the overall height of the column. The plastic rotation was obtained and presented in bending moment-rotation plots for each test specimen. This could help identify the rotational characteristics of the test alternatives with respect to the control specimens. Equations (2) and (3) contain the parameters required for such an analysis, as follows:

$$\theta_p = \frac{\Delta_p}{H} \quad (2)$$

$$\Delta_p = \Delta - \Delta_y \quad (3)$$

where,  $\theta_p$  and  $\Delta_p$  are the plastic rotation and displacement, respectively,  $H$  is the overall column height,  $\Delta$  is the column-top displacement at the actuator level, and  $\Delta_y$  is the yield displacement obtained previously for ductility calculations.

#### 4.1.3 Cumulative Energy Dissipation

One of the main features of bridge ductile elements in high seismic regions is their ability to dissipate energy through inelastic deformations. This is an indication of the quality of the hysteretic response. The presence of mild steel in the plastic hinge region capable of undergoing inelastic behavior is significant for achieving the required amount of energy dissipation. The area enclosed by the hysteresis loops is referred to as the hysteretic energy of a system. This was computed cumulatively for each test specimen to obtain the energy dissipation capacity at any desired time step for comparative studies.

#### 4.1.4 Column Curvature Profile

LVDTs installed on both extreme sides of the column base, were used to study the curvature distribution and curvature capacity of the specimens. Therefore, four curvature segments were specified by using four LVDTs on each side of the column. The average curvature was computed as shown in Equation (4):

$$\phi = \frac{A - B}{wh} \quad (4)$$

where A and B are LVDT readings, and w and h are the segment width and height, respectively. These parameters are shown in **Figure 4-1**, for the first curvature segment in the column base. The average curvature profile was constructed over a 30-in. column height above the column base. The average curvature values were normalized by multiplying them by the column dimension of 21 in., and the curvature segment heights were divided by the column overall height of 96 in. Positive curvature values were associated with the push direction and negative values with the pull direction. The calculated curvature value was assumed to be an average over the whole segment height. Curvature values are included up to a 6% drift ratio, which was the last common drift ratio among all specimens. Dashed lines in the plots mark the top of the GSS in the column base for precast specimens with GSS inside the column.

According to the data collected from strain gauges on the column longitudinal bars and footing or cap beam dowels, the yielding pattern for both extreme bars was studied. This provides information for regions within each specimen with extreme bars in the inelastic range.

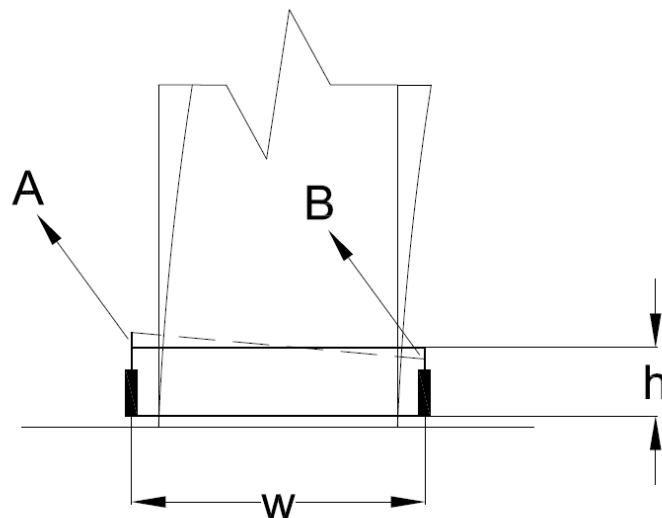


Figure 4-1. Curvature parameters for one curvature segment.

## 4.2 Response of Column-to-Footing Connections

The response of the column-to-footing connections is presented in this section. Four evaluation methods described in **Section 4.1** are utilized to study the results from each test. A comparative study is also presented at the end of this section, emphasizing the similarities and differences that exist between the test specimens.

### 4.2.1 GGSS-1 Results

#### 4.2.1.1 Experimental Observations and Damage States

**Figure 4-2** shows the lateral force-displacement curve in addition to the major damage states including end of crack formation and initiation of spalling, yield penetration, and rebar fracture. Hysteresis loops were wide and stable for this specimen without strength degradation up to a 7% drift ratio. A slight reduction in strength is noted at the 8% drift ratio. The test was terminated at the end of the 9% drift ratio due to a drop larger than 20% in lateral force. The overall hysteresis response was symmetric in terms of strength and residual drift.

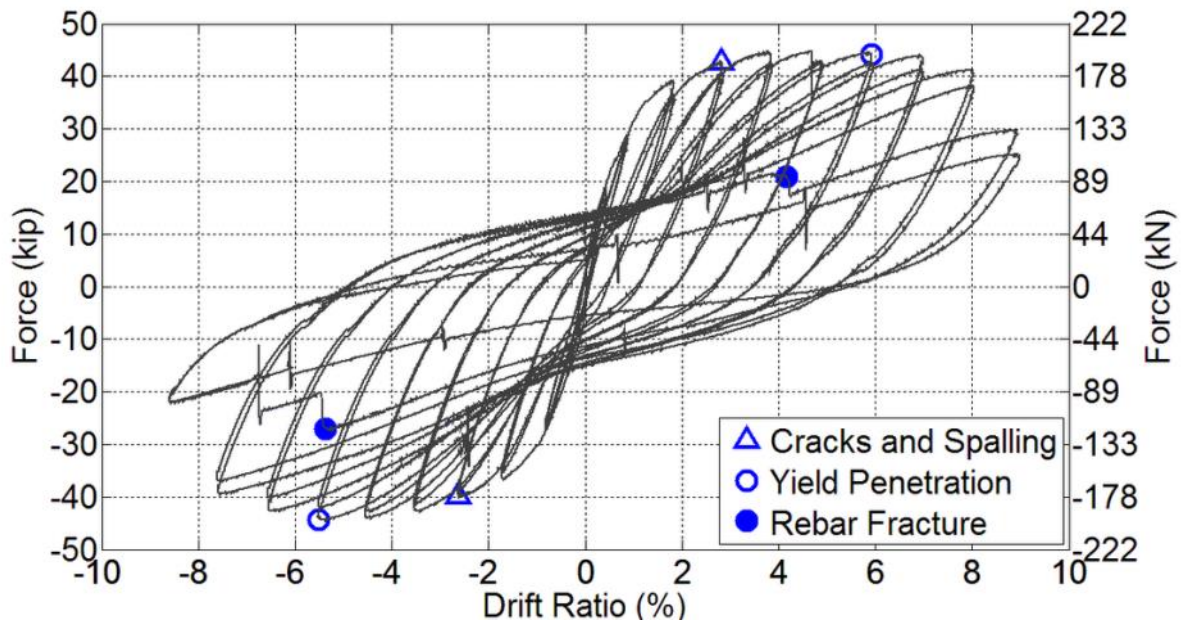
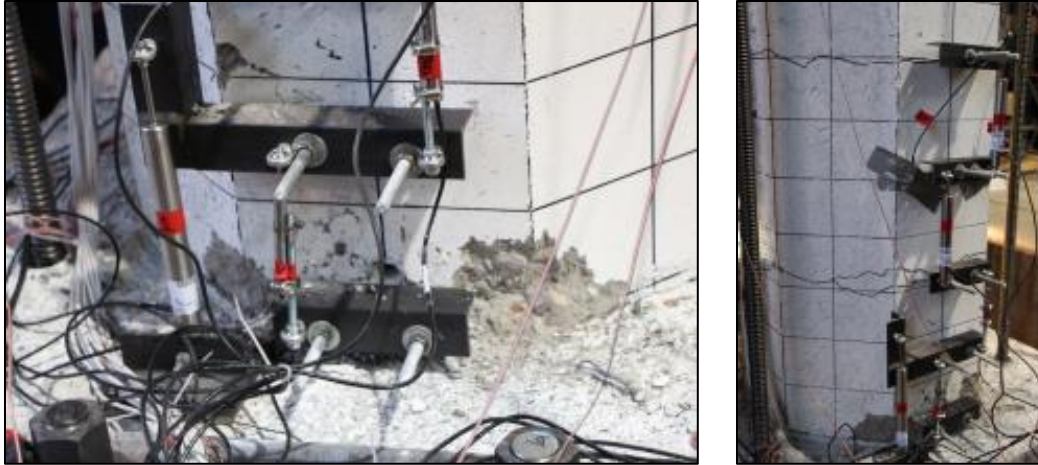


Figure 4-2. Hysteresis response of GGSS-1 with damage states.

A hairline minor crack developed at the bed grout, located at the column-to-footing interface, during the 0.5% drift ratio. This crack became wider and was accompanied by another crack forming right above the GGSS during the first cycle of the 1% drift ratio. By the end of the 3% drift ratio, all major cracks had developed including a relatively large crack at the bed grout, another one at a section close to the top of the GGSS, and a third crack at the end of the spiral-overlapping zone about 30 in. above the column base, as shown in **Figure 4-3(a)**. Spalling initiated during the first cycle of the 3% drift ratio and progressed near the corners of the octagonal column. The spalled area had a height of 4in. on both sides of the column and a crack width of 0.009 in. above the GGSS. Cracks widened and spalling progressed at higher drift ratios. The aforementioned select crack had a width of 0.013 in. at a drift ratio of 4%, 0.02 in. at a drift ratio of 5%, and 0.03 in. at the 6% drift ratio. Yield penetration was noted at the end of the 6% drift ratio with a depth of 1.5 in. and 1 in. on the west and east side of the column, respectively. The height of the spalled region was 8 in. and 14 in. on the west and east side of the column, respectively. **Figure 4-3(b)** shows the damage state at the end of the 6% drift ratio. The column spiral became visible during the 7% drift ratio and a few hairline cracks were spotted on the north and south side of the footing. The bed grout deteriorated around the perimeter of the column end, while the spalled region over the GGSS became deeper and the GGSS was visible at the end of the 8% drift ratio.

During the last drift ratio of 9% for GGSS-1, all six longitudinal column bars had buckled. Concrete spalling grew larger in terms of area and depth, and the spiral and GGSSs were exposed, as shown in **Figure 4-3(c)**. The two extreme bars fractured in the first cycle of the push and pull directions of the 9% drift ratio, due to low cycle fatigue. Rebar fracture occurred 1in. to 1.5 in. below the surface of the footing, where there was no confining transverse reinforcement. Post-test investigations ascertained that the confined concrete core remained undamaged and the GGSSs themselves did not slip inside the column. The footing remained perfectly elastic as a capacity-protected member with minor hairline cracks in the joint region. Compression test results on concrete cylinders and grout cubes indicated that the compressive strength of the concrete and grout were 5.9 ksi and 14.4 ksi, respectively, on the day of the test.



(a) Damage state at 3% drift ratio: cracks and spalling.



(b) Damage state at 6% drift ratio: cracks, spalling, and yield penetration.



(c) Damage state at 9% drift ratio: spalling, exposed rebar cage, and fractured bar.

Figure 4-3. GGSS-1 visual observations.

#### 4.2.1.2 Displacement Ductility Capacity and Plastic Rotation Capacity

The average backbone curve was constructed in accordance with the method described in **Section 4.1.2**, along with the idealized elasto-plastic curve. **Figure 4-4** depicts the plots in addition to the parameters required to obtain the displacement ductility. The effective yield displacement and force for GGSS-1 were found to be 1.45 in. and 41.91 kip, respectively. The ultimate displacement, corresponding to a 20% strength drop, was 7.79 in., resulting in a displacement ductility of 5.4.

**Figure 4-5** displays the moment-plastic rotation relationship up to the test termination point. The plot shows that GGSS-1 had a plastic rotation of 0.0630 rad which occurred at the 8% drift ratio, before excessive strength reduction.

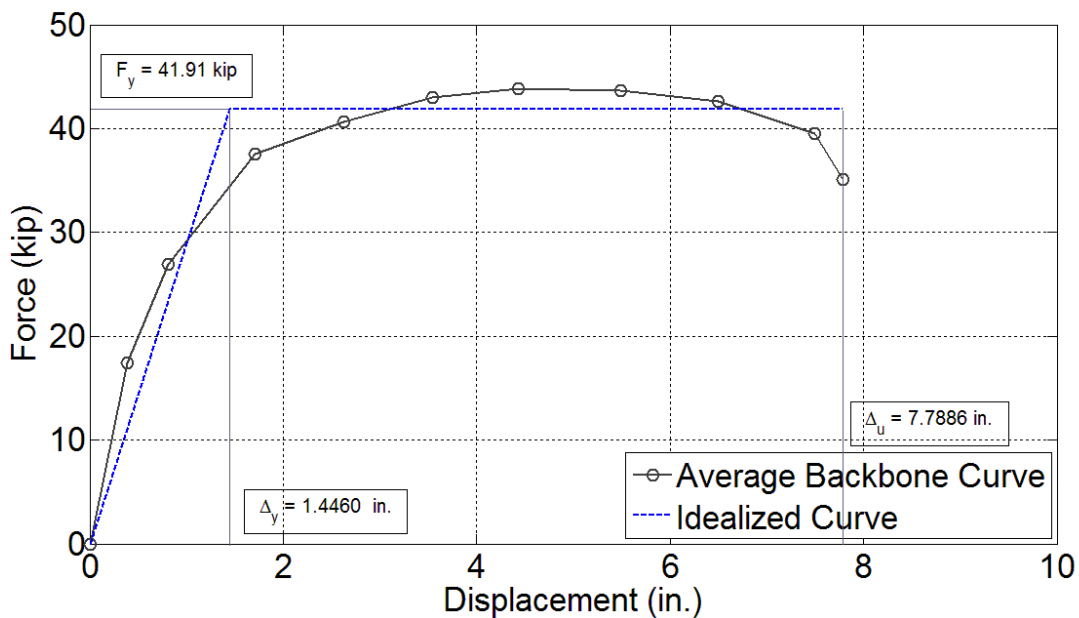


Figure 4-4. Average backbone curve and displacement ductility for GGSS-1.

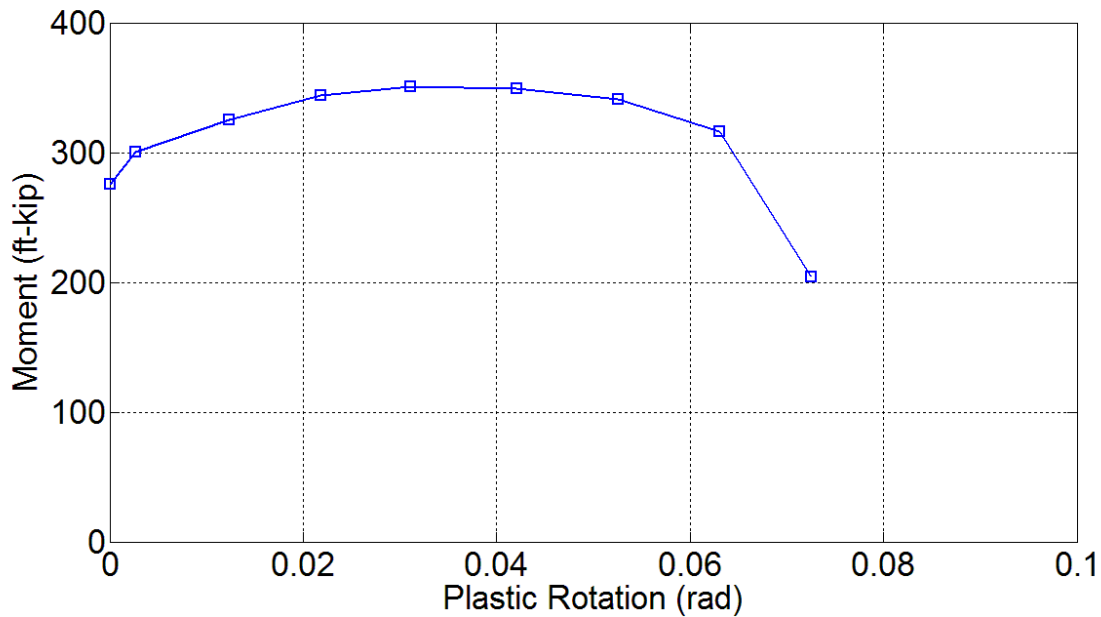


Figure 4-5. Plastic rotation capacity for GGSS-1.

#### 4.2.1.3 Cumulative Energy Dissipation

The cumulative hysteretic energy is plotted against drift levels in **Figure 4-6**. It is noted that GGSS-1 steadily dissipated energy with an increasing rate as it went through the inelastic portion of the response. During the 9% drift ratio, this rate decreased as a result of fracture of extreme column bars. The cumulative hysteretic energy was found to be 253 in-kip, 1487 in-kip, and 2522 in-kip at the 3%, 6%, and 9% drift ratios, respectively.

#### 4.2.1.4 Column Curvature Profile

The GGSS-1 column curvature profile illustrated in **Figure 4-7** indicates that bending action was more pronounced in the two sections below and above the GGSS. This was attributed to the presence of relatively more rigid GGSSs at the column base that resulted in considerably smaller curvature values along the height of the GGSS itself. Lack of curvature above the GGSS region was because of a lower flexural demand around that elevation in the column.

Strain gauges located on the extreme longitudinal bars, at the column base and within the joint core, covered an area with a depth of 7 ½ in. into the footing and 21 ¾ in. up above the

column base. These strain gauges showed that both extreme bars yielded over the whole range covered by strain gauges, except for the initial 5-in. portion of both the factory and field dowels which was embedded and confined inside the GGSS.

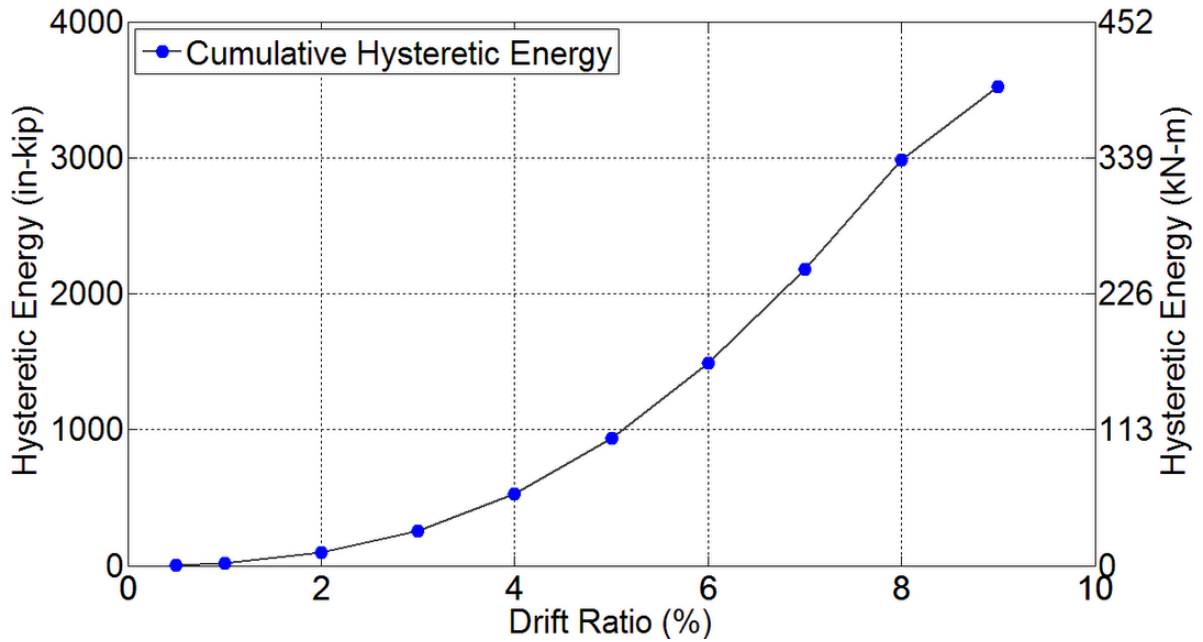


Figure 4-6. Energy dissipation capacity of GGSS-1.

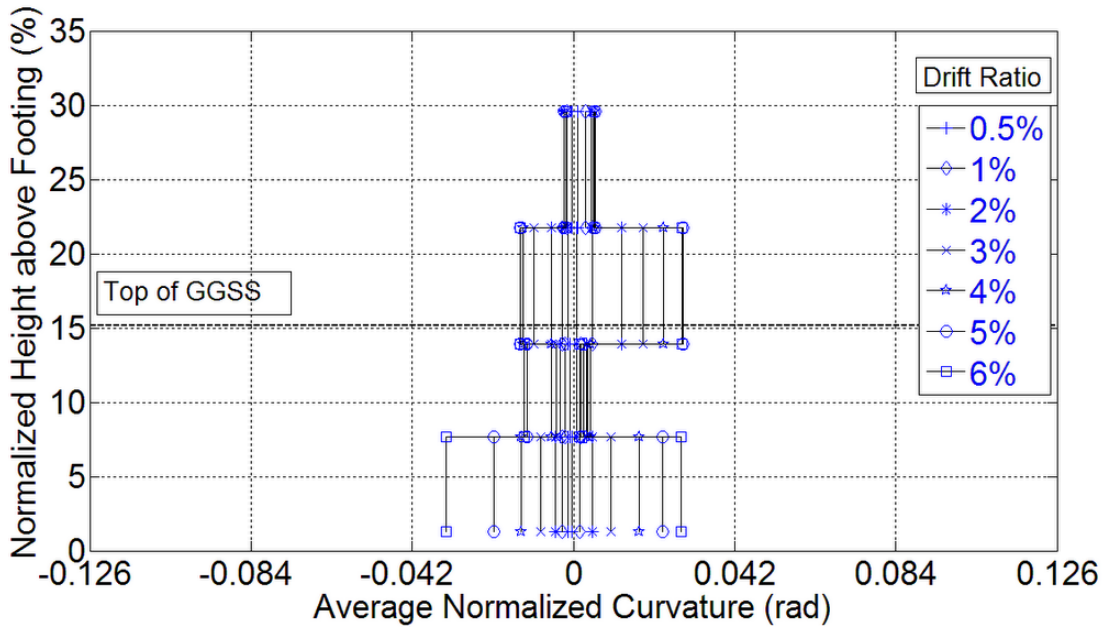


Figure 4-7. Normalized curvature distribution for GGSS-1.

## 4.2.2 GGSS-2 Results

### 4.2.2.1 Experimental Observations and Damage States

**Figure 4-8** shows the hysteresis response of this specimen in addition to the major damage states including end of crack formation and initiation of spalling, and rebar fracture. Hysteresis loops were wide and stable for this specimen without strength degradation up to the 7% drift ratio, when the extreme east column bar fractured during the first pull cycle. The test was terminated at this point due to a drop larger than 20% in the lateral force. The overall hysteresis response was considered satisfactory, although there was a slight difference between the peak lateral forces in the push and pull directions.

Hairline flexural cracks developed at two elevations of 12 in. and 28 in. above the column end during the 0.5% drift ratio. These cracks widened during the next drift ratio followed by another crack formed at the column-to-footing interface. By the end of the 3% drift ratio, a total of 9 major flexural cracks had developed including the two largest cracks that occurred at the bed grout and 6 in. above the column end. The width of the latter crack measured 0.03 in, on the east side of the column. The GGSS-2 column is shown in **Figure 4-9** at maximum displacement during the 3% drift ratio along with the two aforementioned cracks. The initiation

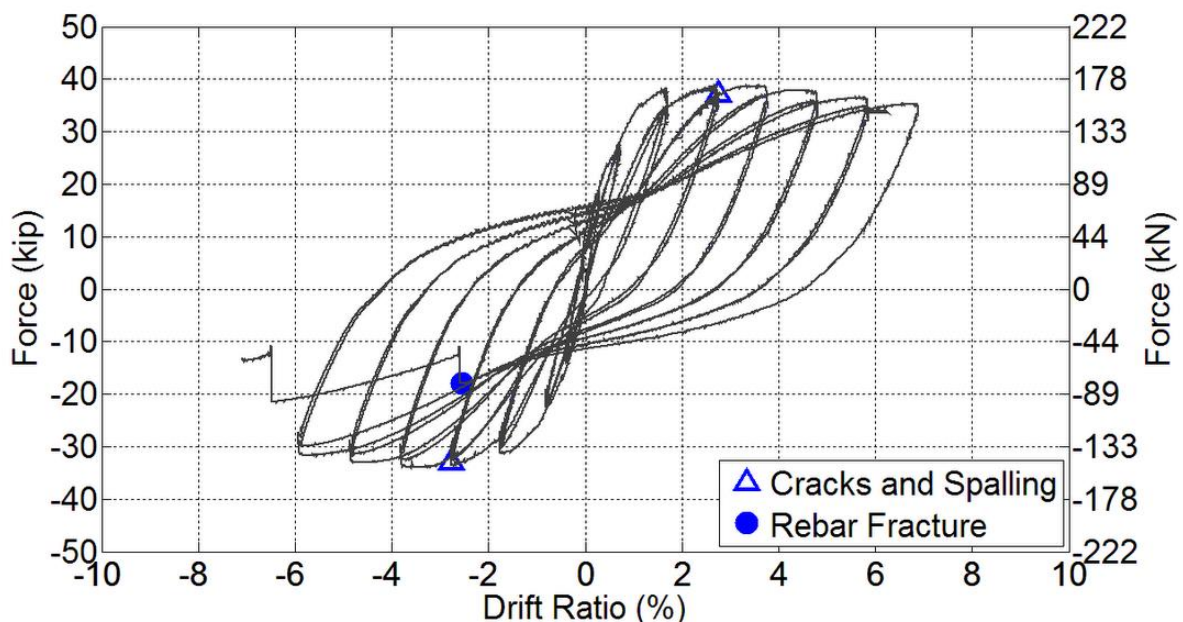


Figure 4-8. Hysteresis response of GGSS-2 with damage states.

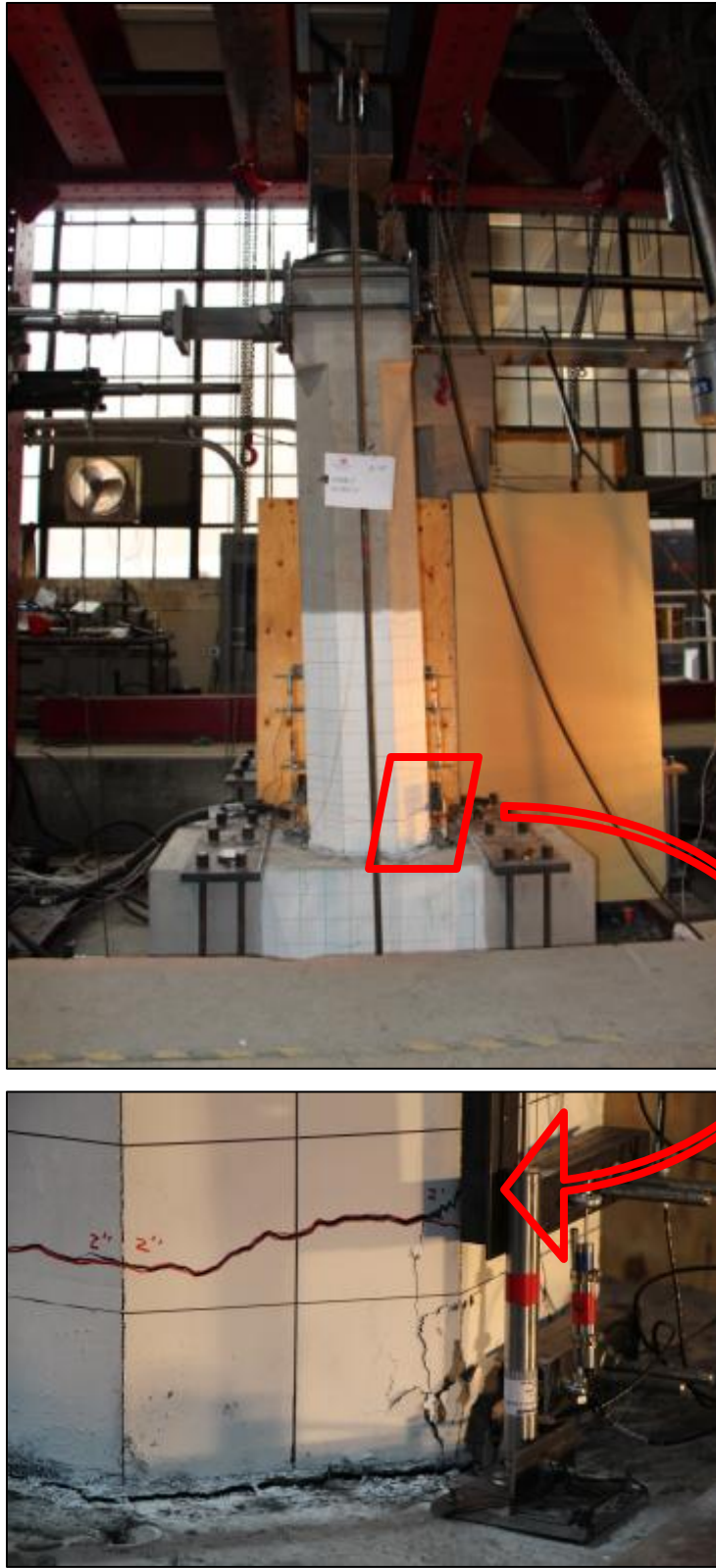


Figure 4-9. GGSS-2 at maximum displacement during the 3% drift ratio—Largest crack.

of spalling at the south-east corner of the octagonal column is also visible with a vertical dimension of 4 in. The state of damage to the column plastic hinge region is shown in **Figure 4-10(a)** in addition to the spalled region and major flexural cracks that formed along the column height. It was noted that flexural cracks occurred at approximately 8-in. increments.

The column plastic hinge region became deteriorated with an increase in the drift ratio. Cracks opened further and spalling intensified during the 4% drift ratio. The select crack located 6 in. above the column base had a width of 0.05 in. at the end of this drift ratio, and another crack at 10 in. from the column base had a width of 0.02 in. A few inclined cracks, known as flexure-shear cracks, developed during the 4% and 5% drift ratios on the north and south sides of the column base, due to an increased tensile demand. A large piece of concrete cover with a dimension of 7 in. split from the column base during the 5% drift ratio. Smaller concrete cover pieces, measured 4 in. and 6 in., became separated from the surface of the column base during the 6% drift ratio.

During the first pull of the 7% drift ratio, the extreme column reinforcing bar fractured at a section 2 in. above the interface, and the test was terminated as the column strength dropped below 80% of the maximum reached. Fracture of the rebar was attributed to low cycle fatigue as a result of successive bending and re-straightening of the extreme reinforcing column bar. Post-test investigation revealed that the cover concrete was crushed completely around the column end, after removing the loose material. Thus, spiral hoops together with extreme column bars were evident at the end of the test.

The crack developed at the column-to-footing interface during the previous drift ratios became a 0.0625-in. permanent gap, when the test was terminated. **Figure 4-10(b)** depicts the damaged area at the column base including major cracks, spalled region, and the fractured column bar.

The footing remained intact with only a few scattered minor cracks below the interface in the joint region. The test-day compressive strength of the concrete and grout was 5.5 ksi and 13.5 ksi, respectively.



(a) Damage state at 3% drift ratio: cracks and spalling.



(b) Damage state at 7% drift ratio: cracks, spalling, fractured bar, and exposed rebar cage.

Figure 4-10. GGSS-2 visual observations.

#### 4.2.2.2 Displacement Ductility Capacity and Plastic Rotation Capacity

A displacement ductility of 6.1 was obtained for this test specimen using the standard procedure described in **Section 4.1.2**, as shown in **Figure 4-11**. The idealized curve was constructed to achieve all parameters required to compute the displacement ductility capacity. The ultimate displacement of 6.42 in. was associated with a 20% drop in the lateral force. Effective yield strength and yield displacement were obtained as 32.63 kip and 1.05 in., respectively.

**Figure 4-12** displays the moment-plastic rotation relationship up to the test termination point. The plot shows that GGSS-2 had a plastic rotation of 0.0478 rad which occurred at the 6% drift ratio, without a considerable reduction in the moment capacity.

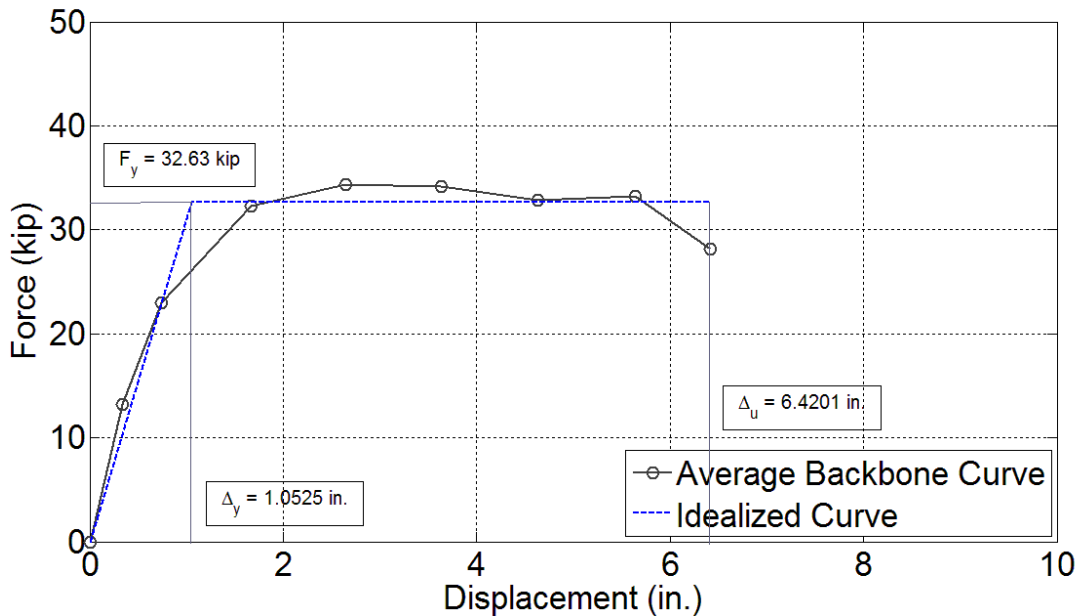


Figure 4-11. Average backbone curve and displacement ductility of GGSS-2.

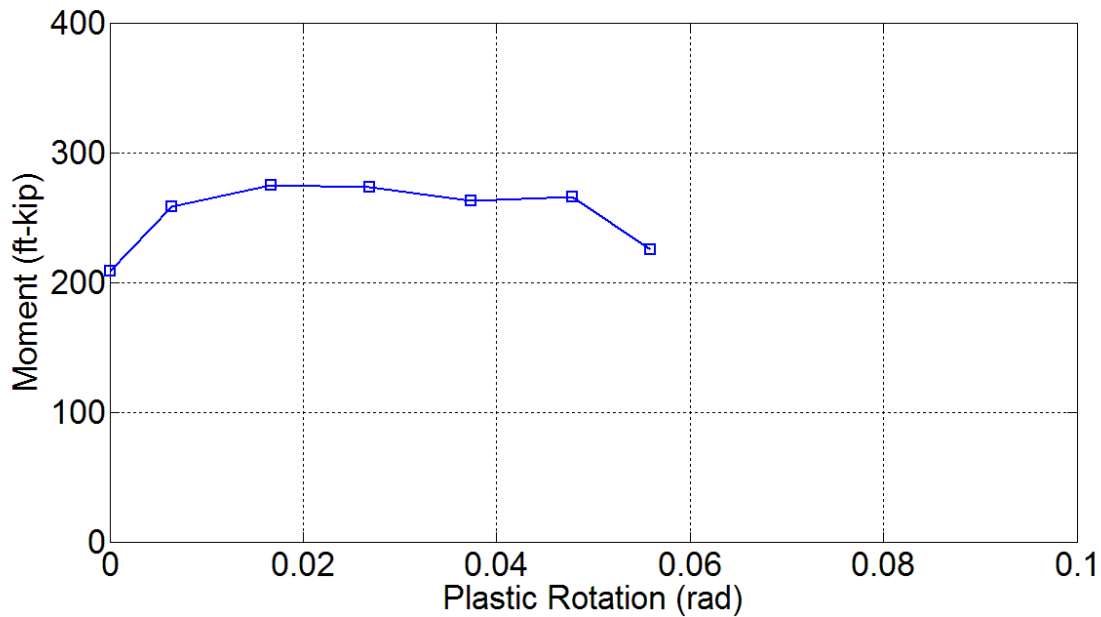


Figure 4-12. Plastic rotation capacity for GGSS-2.

#### 4.2.2.3 Cumulative Energy Dissipation

**Figure 4-13** shows the cumulative hysteretic energy per drift ratio. It was observed that GGSS-2 steadily dissipated energy with an increasing rate during all drift ratios, except for the last drift ratio in which the east column rebar fractured in the first pull cycle. This property of GGSS-2, along with other pertinent response characteristics, will be utilized to ascertain a comparative evaluation of the overall performance, with respect to other specimens in this category. The cumulative hysteretic energy was 270 in-kip at a 3% drift ratio, and 1563 in-kip at a 6% drift ratio.

#### 4.2.2.4 Column Curvature Profile

The GGSS-2 column curvature profile is shown in **Figure 4-14**. A well-distributed curvature profile was achieved for this test specimen as there was no GGSS in the column base to introduce disruption to the regular flow of stresses from the column to the footing. Curvature values were highest along the first curvature segment located closest to the column-to-footing interface, and lowest along the last curvature segment located at the uppermost region of the column base. Curvature demand gradually decreased with an increase in distance from the

interface. This was a desirable distribution of inelasticity along the plastic hinge region of the column.

Strain gauges located on the extreme longitudinal bars, in the column base and within the joint core, covered an area with a depth of 16 in. into the footing and 20 in. up above the column base. These strain gauges showed that the extreme column dowels yielded starting at 5 in. from the tip of the column dowel bars which was confined within the GGSS connectors, or in other words, 2 in. into the footing from the column-to-footing interface. On the contrary, the footing dowel bars did not perform inelastically and strain values remained below the rebar yield strain.

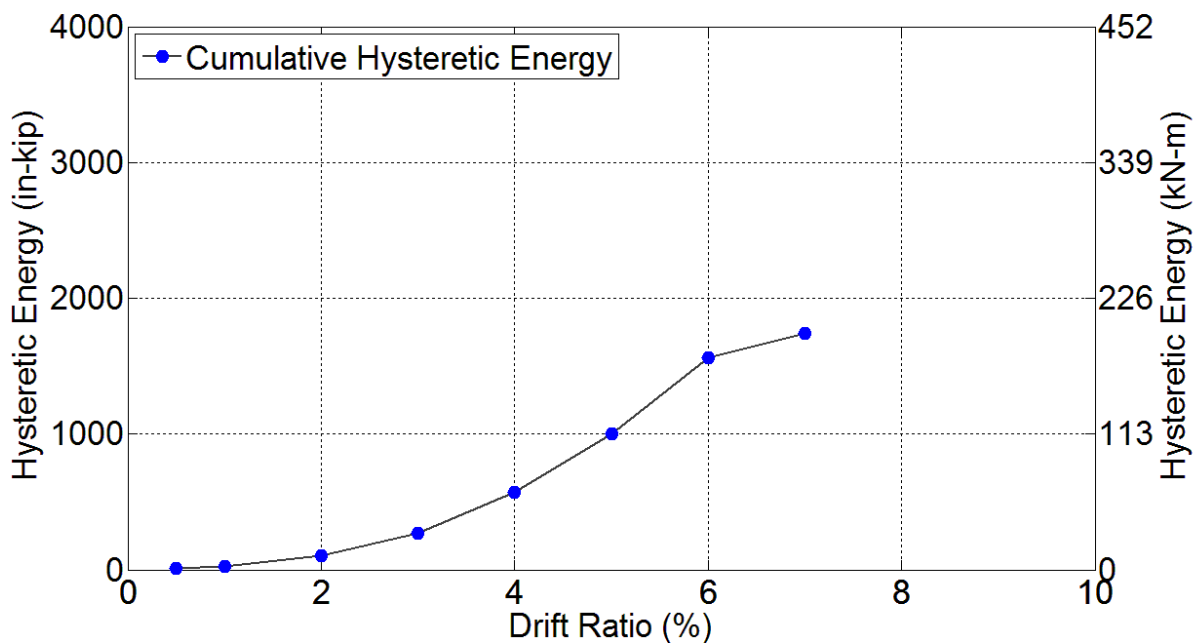


Figure 4-13. Energy dissipation capacity of GGSS-2.

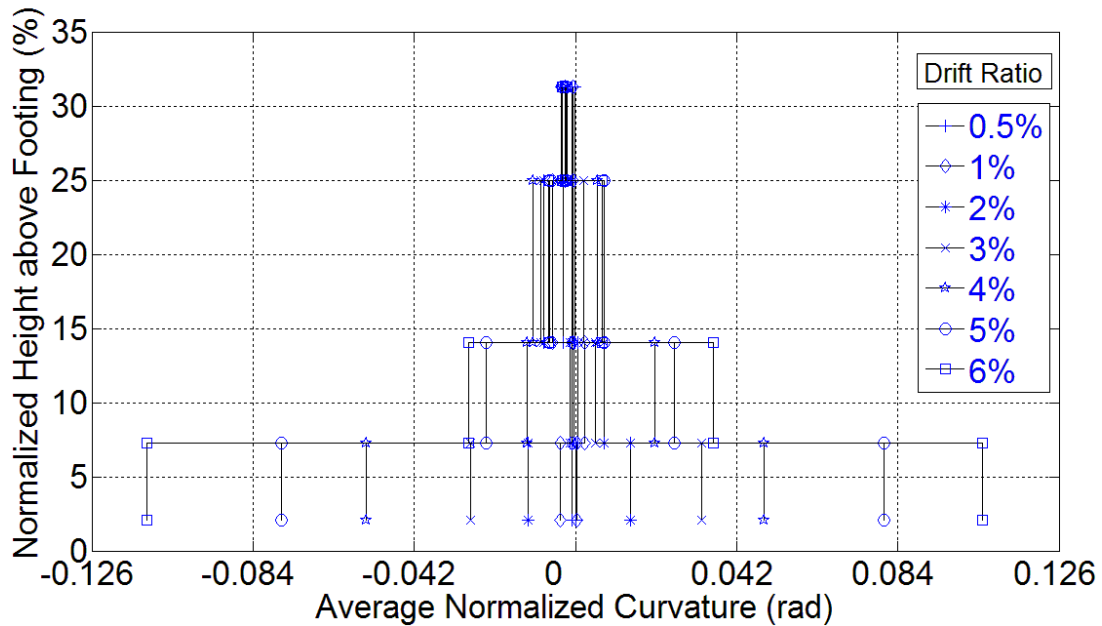


Figure 4-14. Normalized curvature distribution for GGSS-2.

### 4.2.3 GGSS-3 Results

#### 4.2.3.1 Experimental Observations and Damage States

The hysteresis response of GGSS-3 is plotted in **Figure 4-15** including damage states such as end of crack development and initiation of spalling, and fracture of the column rebar. GGSS-3 had wide and stable hysteresis loops that implied a relatively good energy dissipation capacity. Strength peaked at the 5% drift ratio for both push and pull directions, then slightly reduced afterwards. Strength degradation was minimal up to the last drift ratio when the east column rebar fractured during the first pull cycle. The test was terminated at the end of the 8% drift ratio with a 35% drop in strength in the pull direction. The overall hysteresis response indicated an entirely satisfactory and ductile performance.

During the first cycle of the 0.5% drift ratio hairline flexural cracks formed at two elevations: (i) at 14 in., i.e. at the top of the GGSS, and (ii) at 23 in. above the column-to-footing interface. Five more cracks developed along the column height including one crack at the bed-to-grout interface during the 1% drift ratio. These cracks opened further when the column top was at a maximum displacement during the 2% drift ratio, but then closed back up by the time

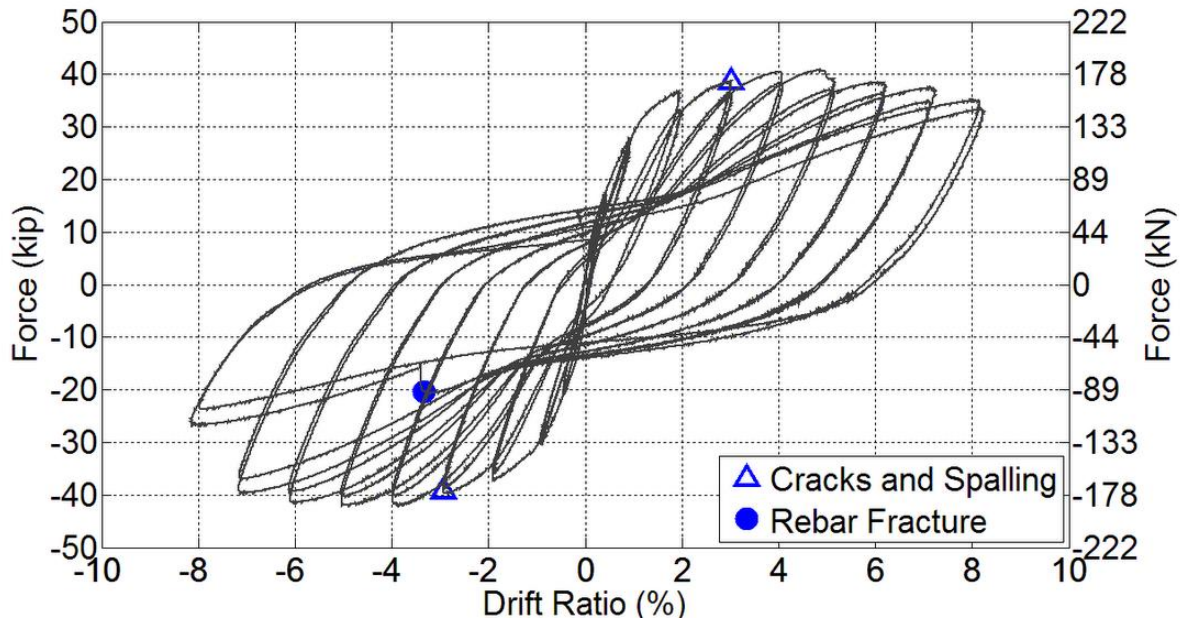


Figure 4-15. Hysteresis response of GGSS-3 with damage states.

the specimen returned to zero drift, hence all cracks were still considered hairline. The crack developed at the interface would turn into a relatively large opening while the column top was at the extreme position. By the end of the 3% drift ratio, eight flexural cracks had formed in the column, two of which, located at the interface and above the GGSSs, had the largest widths. The width of the crack above the GGSS was measured at 0.007 in. during the 3% drift ratio. Partial spalling initiated at the corners of the octagonal column during the last cycle of the 3% drift ratio. **Figure 4-16(a)** shows the state of damage at the end of the 3% drift ratio.

Spalling continued to grow on the east and west sides of the column near the interface with increasing column displacement. The spalled area had a vertical dimension of less than 4 in. in the plastic hinge zone after completion of the 4% drift ratio. The select crack that was located above the GGSS had width of 0.013 in. at the end of this drift ratio. Spalling became more severe during the next few cycles, with a maximum height of the flaked concrete of 10 in. and 16 in. for the 5% and 6% drift ratios, respectively. The width of the select crack was 0.02 in. throughout the remaining cycles until completion of the test.

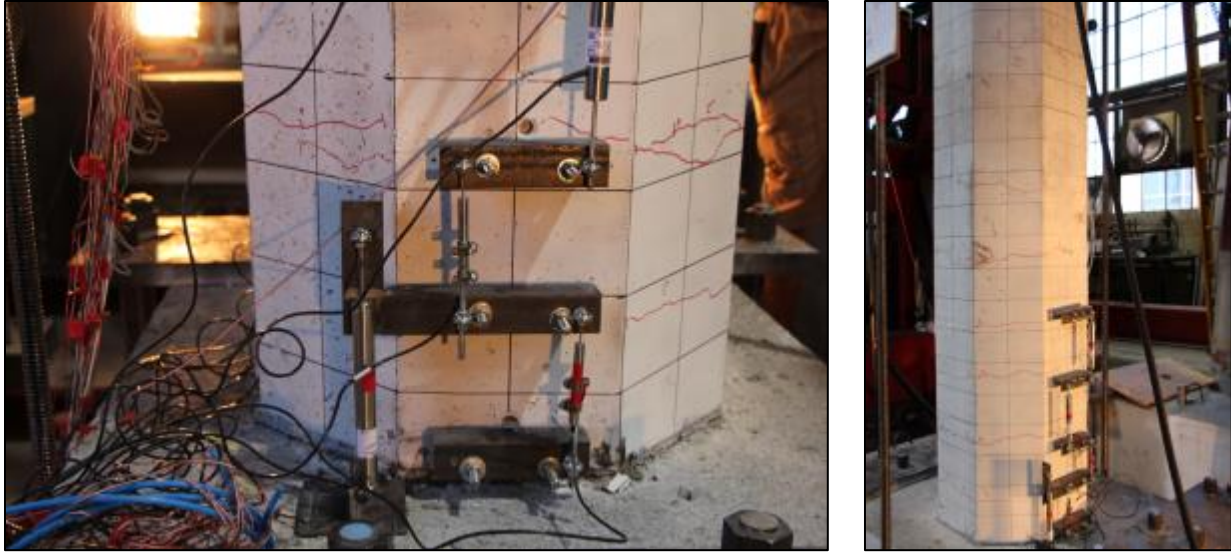
The spiral reinforcement became exposed during the 7% drift ratio when the cover concrete crushed completely over the lowermost column segment. The gap created at the bed

grout section became magnified, when the column was at the extreme position, in such a way that the footing dowel bar became visible, as displayed in **Figure 4-17**.

During the first pull at the 8% drift ratio, the extreme column reinforcing bar fractured at the interface, and the test was terminated as the column strength dropped below 80% of the maximum. Fracture of the rebar was attributed to low cycle fatigue as a result of successive bending and re-straightening. Post-test investigation revealed that the cover concrete deteriorated within the lowest 4-in. section of the column, and hence, one spiral hoop and the bottom end of the GGSS were visible. The bed grout deteriorated in most areas within the interface and large loose pieces were removed from the interface. Damaged concrete was noted around the top portion of the debonded bars in the footing.

The crack which had developed at the column-to-footing interface during the previous drift ratios became a 3/32-in. permanent gap at the end of the test. **Figure 4-16(b)** depicts the damaged area in the column base including major cracks, spalled region, and the fractured column bar.

The footing remained intact without any evident damage. The test-day compressive strength of the concrete and grout were 8.4 ksi and 14.6 ksi, respectively.



(a) Damage state at 3% drift ratio: cracks and spalling.



(b) Damage state at 8% drift ratio: cracks and spalling, fractured bar, and exposed rebar cage.

Figure 4-16. GGSS-3 visual observations.

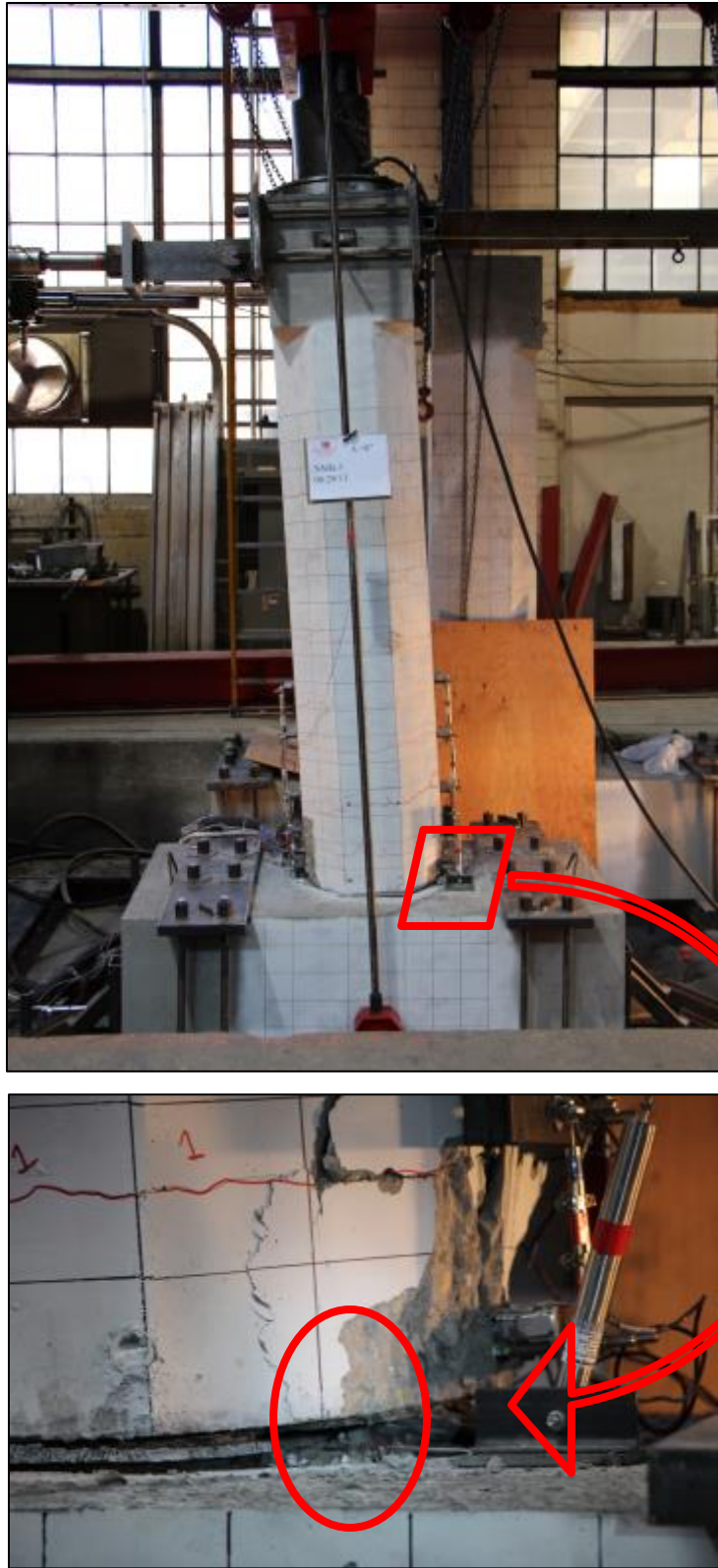


Figure 4-17. GGSS-3 footing dowel became visible at the 7% drift ratio.

#### 4.2.3.2 Displacement Ductility Capacity and Plastic Rotation Capacity

The average backbone curve was constructed by taking the average of the peak points in the push and pull direction from the force-displacement response. The idealized curve was then obtained following the procedure discussed in **Section 4.1.2**.

**Figure 4-18** shows both curves including the necessary parameters to study the displacement ductility capacity of GGSS-3. The effective yield point was identified by the effective yield strength as 38.21 kip, and the yield displacement as 1.11 in. The ultimate displacement corresponding to a 20% drop in the lateral force was obtained as 7.58 in. A displacement ductility capacity of 6.8 was achieved by this specimen—the highest displacement ductility capacity among all precast column-to-footing specimens.

**Figure 4-19** displays the moment-plastic rotation relationship up to test termination. GGSS-3 had a plastic rotation of 0.0603 rad that occurred at the 7% drift ratio, prior to a strength reduction at the 8% drift ratio.

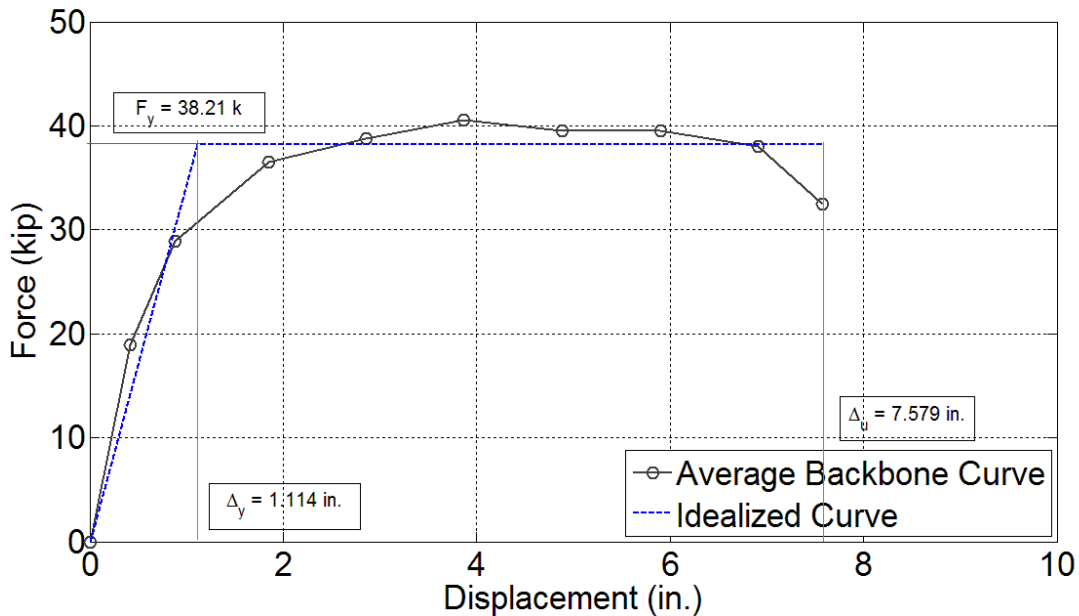


Figure 4-18. Average backbone curve and displacement ductility of GGSS-3.

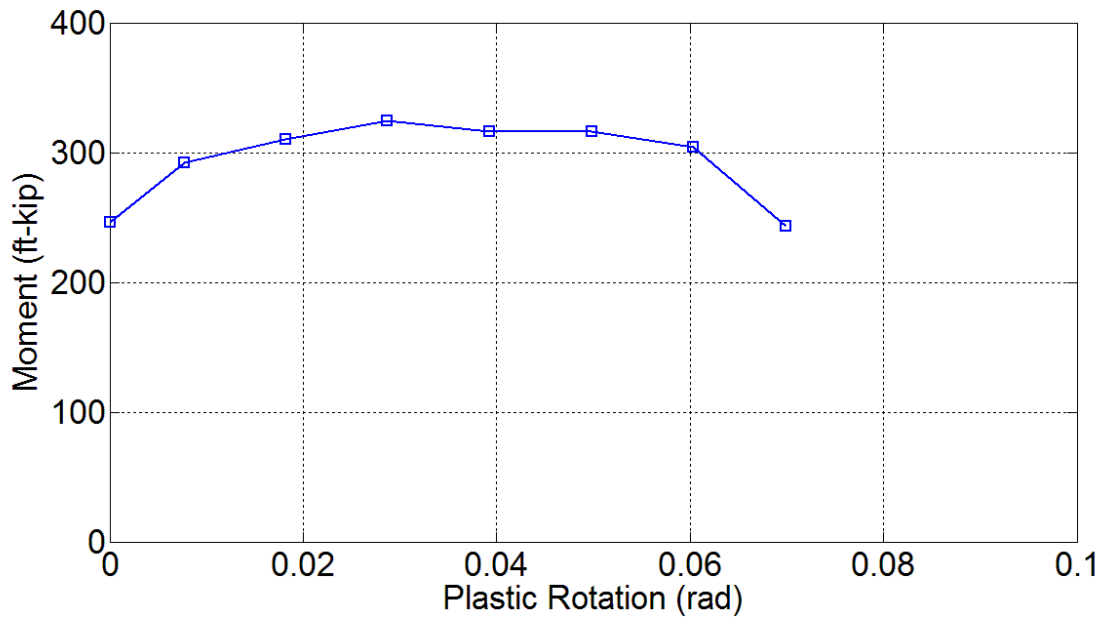


Figure 4-19. Plastic rotation capacity for GGSS-3.

#### 4.2.3.3 Cumulative Energy Dissipation

The area enclosed by the hysteresis loops of GGSS-3 was calculated for each drift ratio and plotted cumulatively, as shown in **Figure 4-20**. The hysteretic energy capacity of this specimen was found to be entirely acceptable and satisfactory, as a result of a desirable cyclic performance. The cumulative hysteretic energy was 287 in-kip, 1613 in-kip, and 3042 in-kip at the 3%, 6%, and 8% drift ratios, respectively.

#### 4.2.3.4 Column Curvature Profile

**Figure 4-21** displays the average normalized curvature profile along the GGSS-3 column base. The plot shows that the curvature demand was minimal over the GGSS region and inelastic action was shifted to lower sections into the footing, especially within the 8-in. debonded rebar region and consequently over the unconfined section around the column-to-footing interface. This curvature profile demonstrates that the contribution of the column flexural behavior to the column displacement is relatively small; on the contrary, the effect of rebar slip over the debonded region plays a significant role in the overall inelastic response of GGSS-3.

Strain gauges located on the extreme longitudinal bars, in the column base and within the joint core, covered an area with a depth of 7 in. into the footing and 22 in. up above the column base. These strain gauges showed that both extreme bars yielded over the range covered by strain gauges, except for the initial 5-in. portion of both the factory and field dowels which was embedded and confined inside the GGSS.

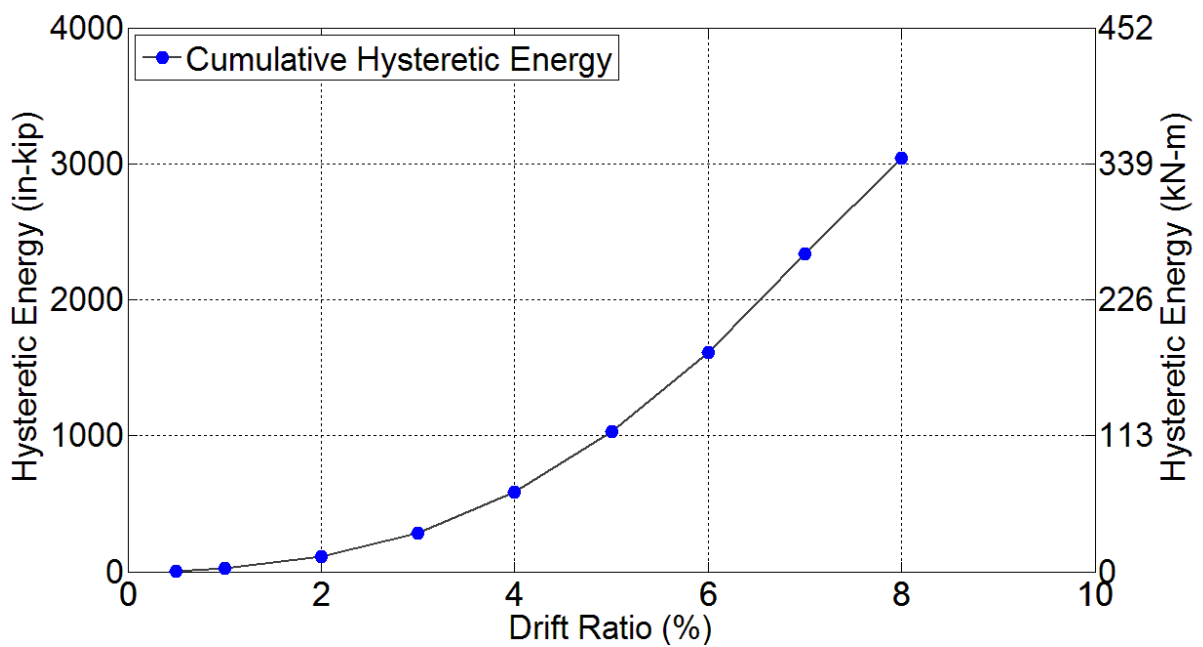


Figure 4-20. Energy dissipation capacity of GGSS-3.

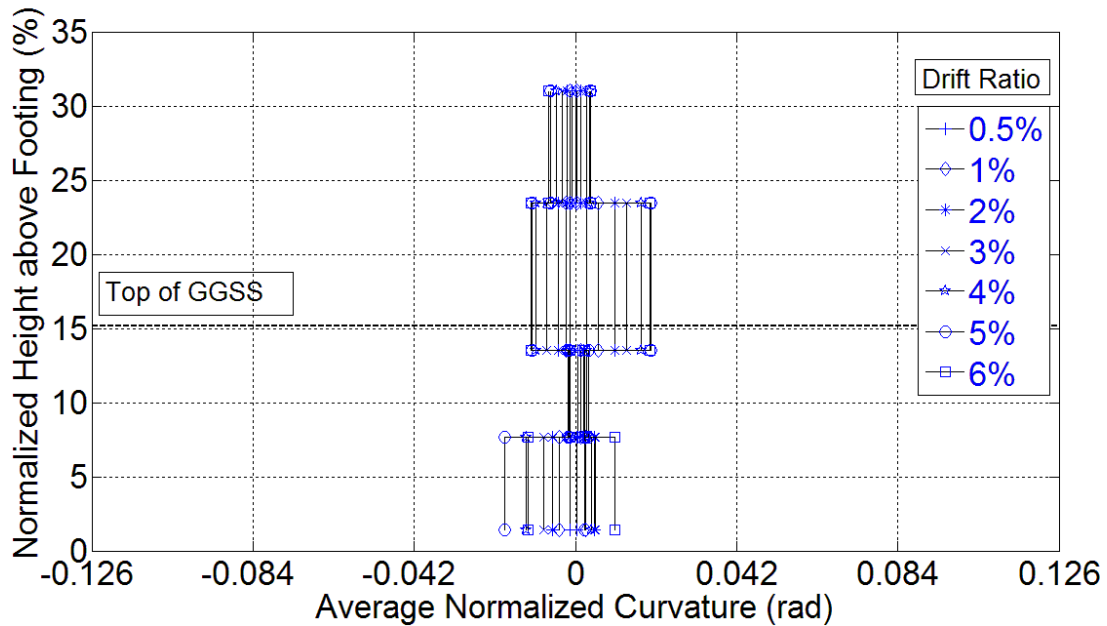


Figure 4-21. Normalized curvature distribution for GGSS-3.

#### 4.2.4 GGSS-CIP Results

##### 4.2.4.1 Experimental Observations and Damage States

The hysteretic response of this test specimen is presented in **Figure 4-22**, in addition to damage states corresponding to: (1) end of major crack formation and beginning of spalling, (2) yield penetration, and (3) rebar fracture. The overall response was very good as a result of the wide and stable hysteresis loops that implied a relatively high energy dissipation capacity. The lateral load peaked at 35.95 kip during the 2% drift ratio and at 37.07 kip during the 4% drift ratio for the push and pull direction, respectively.

The column west rebar fractured at the end of the 2<sup>nd</sup> push during the 8% drift ratio, and the east bar fractured during the 1<sup>st</sup> pull of the 9% drift ratio, by the end of which the test was terminated. This test specimen had a remaining 60% strength capacity at the end of the test, in both directions.

By the end of the 0.5% drift ratio, two hairline flexural cracks formed at two sections located 12 in. and 32 in. above the column-to-footing interface. More flexural cracks developed

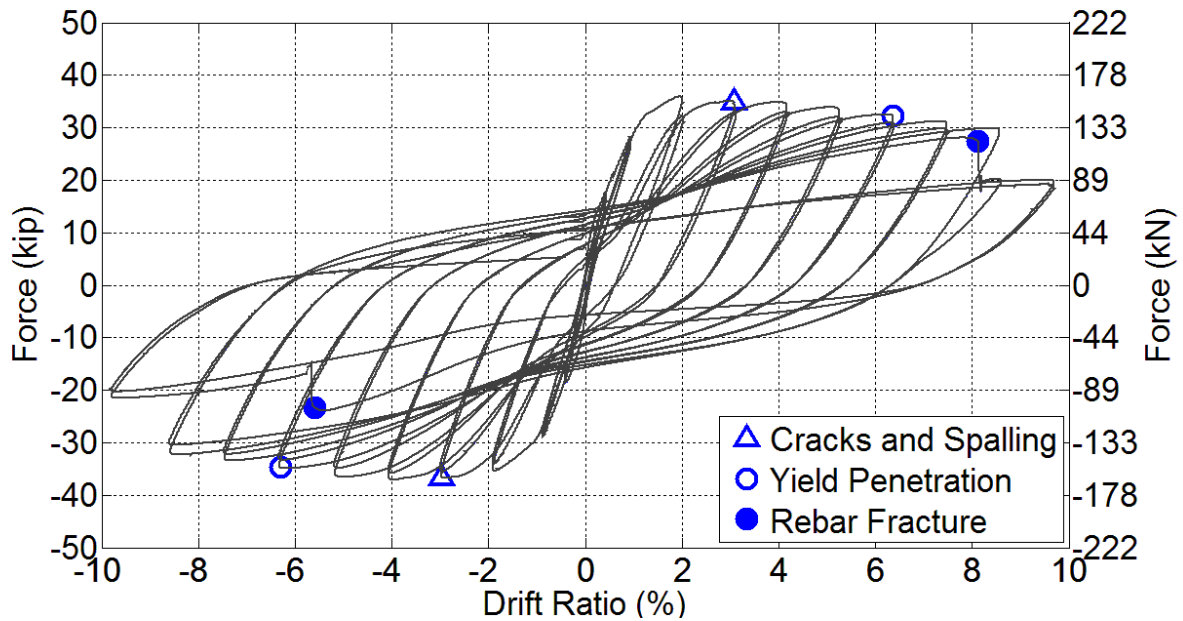


Figure 4-22. Hysteresis response of GGSS-CIP with damage states.

during the 1% drift ratio and 2% drift ratio. The largest crack which had developed 4 in. above the column base had a width of 0.02 in. on the east side of the column during the 2% drift ratio. Concrete delamination initiated around the west and east sides of the column during the 1% drift ratio. This condition became more evident with increasing drift ratios. Spalling initiated at the column corners and a total of nine flexural cracks developed by the end of the 3% drift ratio. The select crack developed at 4 in. above the column base had a width of 0.06 in. at the end of the 3% drift ratio. Another major crack that had formed 12 in. above the column base during the previous drift ratio widened and measured 0.007 in. **Figure 4-23(a)** displays the damage state at the end of the 3% drift ratio.

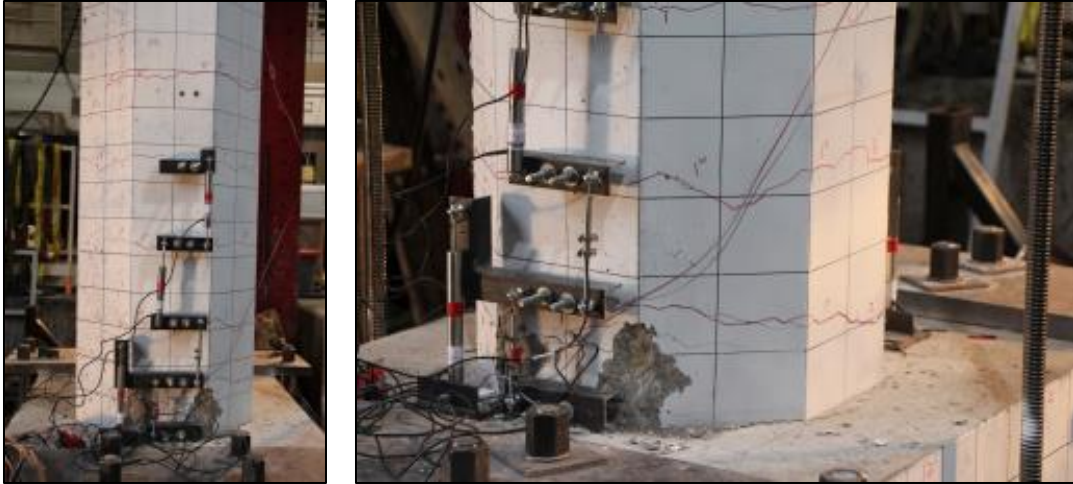
At the 4% drift ratio, spalling grew larger especially at the column corners. A 12-in. high spalled area was evident on both sides of the column. The aforementioned largest crack—formed at an elevation 4 in. above footing—closed back up and measured 0.025 in. The width of other representative cracks remained unchanged. During the 5% drift ratio, inclined or flexure-shear type cracks developed on the north and south sides of the column because of an increased tensile demand in the concrete.

At the 6% drift ratio, spalling became wider and covered most of the plastic hinge region of the column, hence all major cracks were hidden within the spalled region which made it difficult to make crack-width measurements. Yield penetration was also noted around the extreme two bars. **Figure 4-23(b)** shows the extent of damage to the column base including major flexural and inclined cracks, and the spalled region.

During the 7% drift ratio, the spalled region became deeper in such a way that the spiral became partially visible. The extreme west column rebar fractured, as a result of low cycle fatigue, slightly before the peak displacement during the second push of the 8% drift ratio while the extreme east column bar was still undamaged but visible. This rebar broke during the first cycle of the 9% drift ratio due to low cycle fatigue caused by consecutive high-strain bending and re-straightening of the rebar.

Post-test investigations revealed that the west and east column bar fractured 1.5 in. and 2 in. above the footing. The footing concrete delamination had a depth of 1 in. on the west side. The spalled region in the plastic hinge region had a maximum width and effective height of 21 in. and 8 in., respectively. At the end of the test, column longitudinal rebar and spiral were visible at the column base, as shown in **Figure 4-23(c)**.

The footing remained intact with only two minor cracks developing in the joint region during the 2% drift ratio. The test-day compressive strength of the concrete was 6.7 ksi.



(a) Damage state at 3% drift ratio: cracks and spalling.



(b) Damage state at 6% drift ratio: spalling and inclined cracks.



(c) Damage state at end of test: cracks, spalling, concrete delamination, and fractured rebar.

Figure 4-23. GGSS-CIP visual observations.

#### 4.2.4.2 Displacement Ductility Capacity and Plastic Rotation Capacity

Following the procedure described in this chapter, the average backbone curve and idealized curve were constructed to compute the displacement ductility capacity of GGSS-CIP. The effective yield strength and yield displacement were obtained as 33.62 kip and 0.95 in., respectively. The ultimate displacement corresponding to a 20% reduction in the lateral force capacity was equal to 8.45 in. Consequently, the displacement ductility capacity of GGSS-CIP was found to be 8.9. **Figure 4-24** shows both the average backbone curve and idealized curve along with relevant parameters.

**Figure 4-25** displays the moment-plastic rotation relationship up to test termination. The plot shows that GGSS-CIP had a plastic rotation of 0.0759 rad at the 8% drift ratio, prior to a considerable reduction in moment capacity.

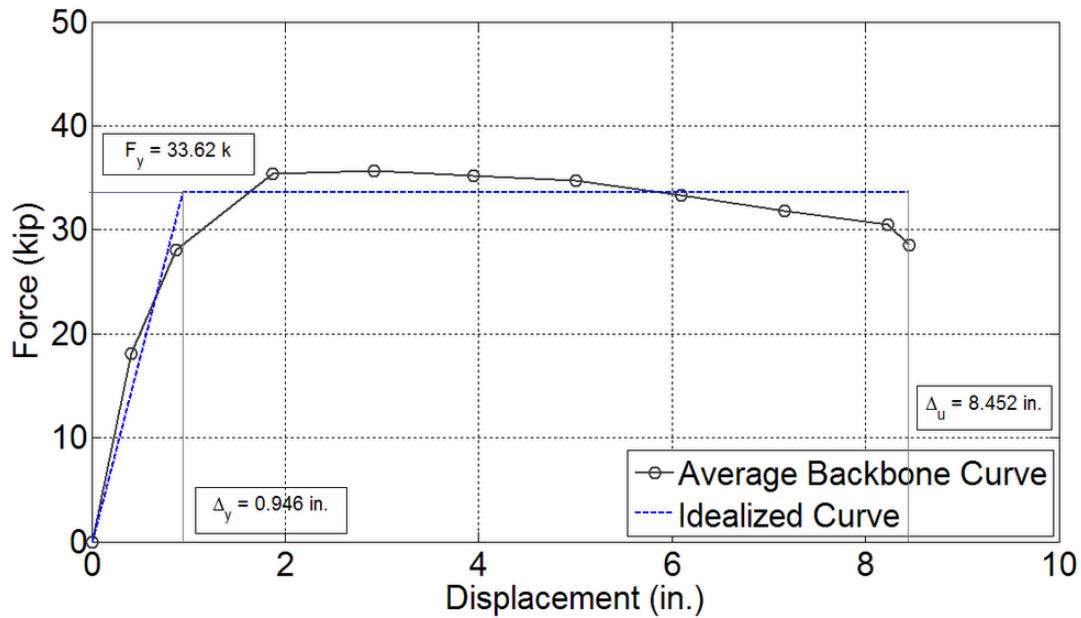


Figure 4-24. Average backbone curve and displacement ductility of GGSS-CIP.

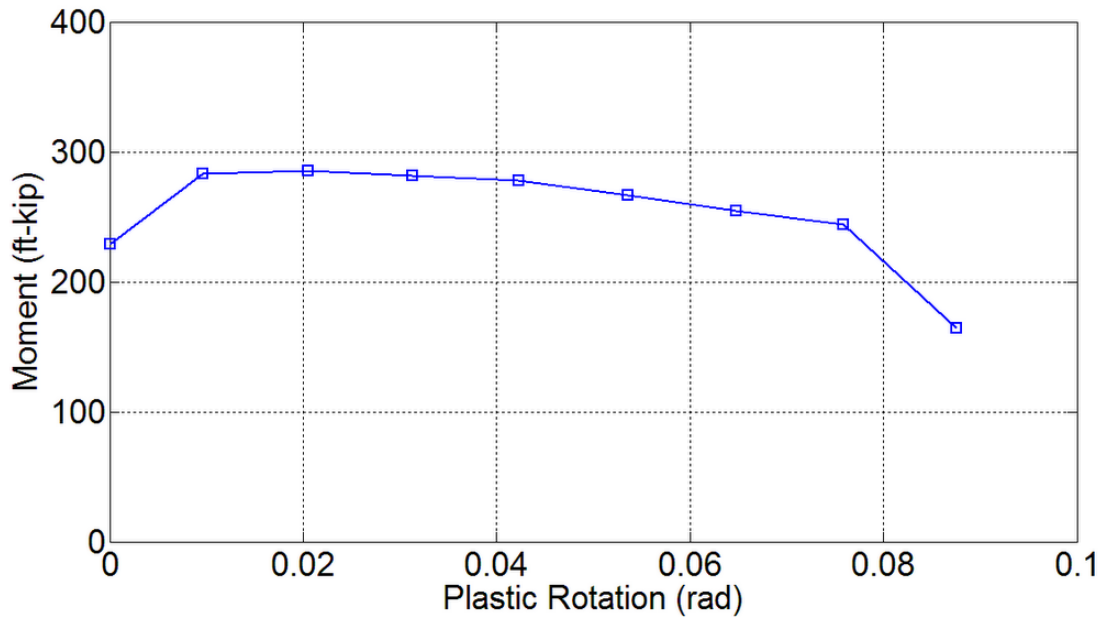


Figure 4-25. Plastic rotation capacity for GGSS-CIP.

#### 4.2.4.3 Cumulative Energy Dissipation

The cumulative hysteretic energy is plotted against drift levels in **Figure 4-26**. It was observed that the specimen dissipated energy at an increasing rate as it went through the inelastic portion of the response. The rate did not decrease during the 8% drift ratio even though a column rebar fractured. This was because the rebar fracture occurred when the column-top displacement was close to the peak, hence did not drastically affect the dissipated energy during the 8% drift ratio. However, this affected the hysteretic energy capacity of the 9% drift ratio as the lateral force capacity was reduced. Also, the fracture of the column east rebar during this drift ratio resulted in a decrease in energy dissipation. The cumulative hysteretic energy was 299 in-kip, 1657 in-kip, and 3906 in-kip at 3%, 6%, and 9% drift ratio, respectively.

#### 4.2.4.4 Column Curvature Profile

The curvature profile for GGSS-CIP is shown in **Figure 4-27**. A well-distributed curvature profile was achieved for this specimen as expected for a reinforced concrete column, with conventional cast-in-place details. Curvature values were highest along the first curvature segment located closest to the column-to-footing interface, and lowest along the last curvature

segment located at the uppermost region of the column base. This was a desirable curvature distribution along the plastic hinge region of the column.

Strain gauges located on the extreme longitudinal bars, in the column base and within the joint core, covered an area with a depth of 9 ½ in. into the footing and 34 in. up above the column base. These strain gauges showed that both extreme column bars yielded within this instrumented region.

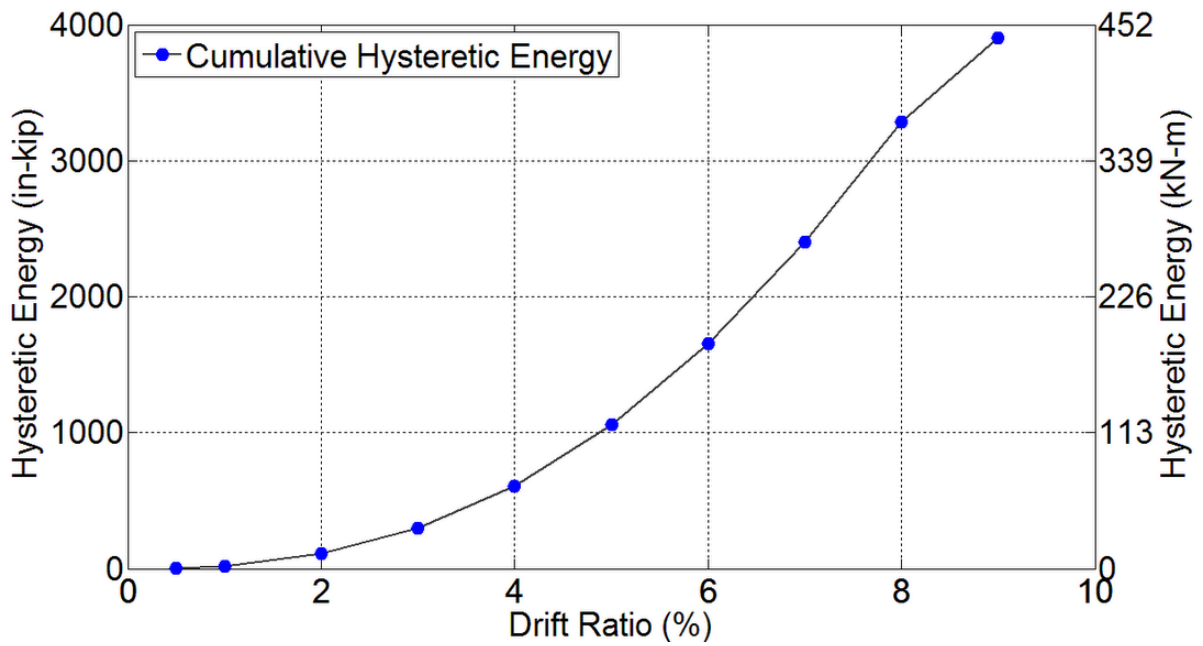


Figure 4-26. Energy dissipation capacity for GGSS-CIP.

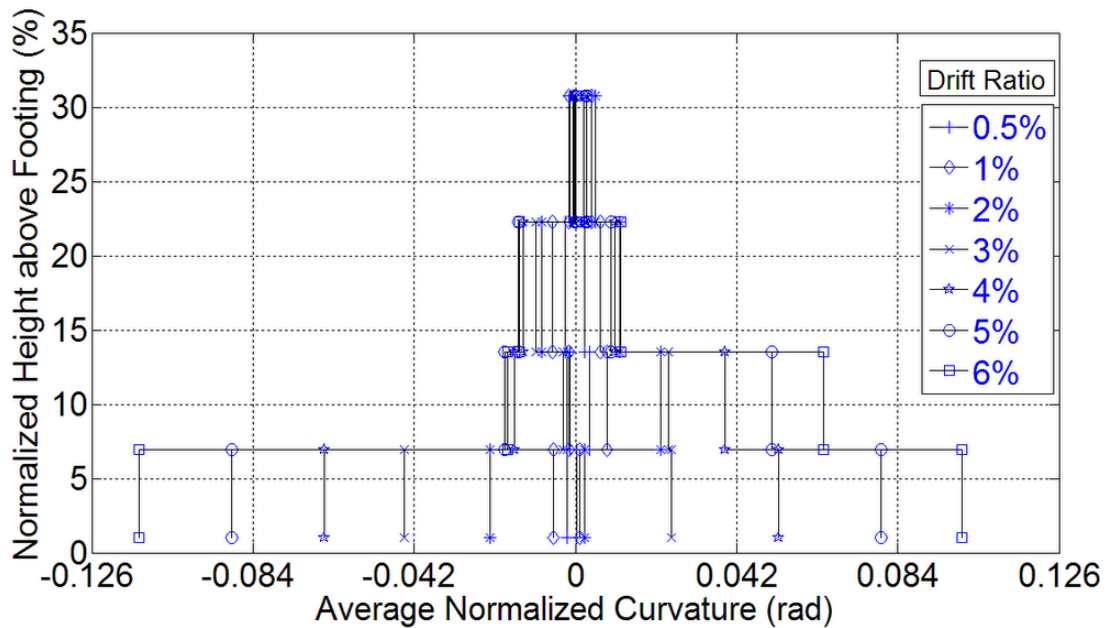


Figure 4-27. Normalized curvature distribution for GGSS-CIP.

#### 4.2.5 Comparative Study of Column-to-Footing Connections

To compare the results from the experiments in this category of test specimens, it is essential to know the material properties for the rebar, concrete, and grout. Tension test on reinforcing bars along with compression tests on concrete cylinders and grout cubes were performed for each test specimen. The results of tension tests on reinforcing bars for the column-to-footing specimens are presented in **Table 4-1**. It is observed that the same rebar was incorporated in all test alternatives. **Table 4-2** contains the compression test results for the concrete and the grout utilized in the construction of the column-to-footing test specimens.

Table 4-1. Rebar properties for column-to-footing test specimens.

Specimen	Column Rebar			
	Longitudinal (NO. 8)		Transverse (NO. 4)	
	Yield	Ultimate	Yield	Ultimate
GGSS-1	68	93	63	103
GGSS-2	68	93	63	103
GGSS-3	68	93	63	103
GGSS-CIP	68	93	63	103

Table 4-2. Concrete and grout properties for column-to-footing test specimens.

Specimen	Concrete		Grout	
	28-day	Test day	28-day	Test day
GGSS-1	5.3	5.9	14.4	14.4
GGSS-2	3.9	5.5	11.1	13.5
GGSS-3	6.7	8.4	15.6	14.6
GGSS-CIP	5.2	6.7	NA	NA

#### 4.2.5.1 Force-Displacement Response

In the previous sections, the displacement ductility capacity of each test specimen was obtained based upon the hysteretic response to the simulated seismic loads. The displacement ductility capacity of all specimens in this category is shown in **Table 4-3**, in addition to the parameters used to perform the calculations. It is noted that GGSS-1 had the lowest displacement ductility capacity of 5.4, GGSS-2 had an intermediate value of 6.1, and the ductility for GGSS-3 was 6.9. These values compared well to the displacement ductility of 8.9 that was achieved for the cast-in-place specimen, i. e. GGSS-CIP. In addition, the displacement ductility capacities obtained for all precast test specimens exceeded the minimum displacement ductility capacity of 3 for ductile components as specified in Caltrans Seismic Design Criteria (SDC) [17]. According to the AASHTO-Seismic provisions, the local ductility demand for ductile members in high-seismic zones is limited to 5 and 6 for single-column bents and multiple-column bents, respectively [16].

Table 4-3. Effective yield properties and displacement ductility for column-to-footing test specimens.

Specimen	Last Drift Ratio (%)	$F_y$ (kip)	$\Delta_y$ (in.)	$\Delta_u$ (in.)	$K_{eff}$ (kip/in)	$\mu_\Delta$
GGSS-1	9	41.91	1.45	7.79	28.98	5.4
GGSS-2	7	32.63	1.05	6.42	31.00	6.1
GGSS-3	8	38.21	1.11	7.58	34.31	6.8
GGSS-CIP	9	33.62	0.95	8.45	35.55	8.9

The force-displacement response of the column-to-footing test specimens revealed a noticeable distinction between the precast specimens and the GGSS-CIP. The GGSS-CIP failed due to rebar fracture of the column longitudinal bars, as a result of the low cycle fatigue. A premature rebar fracture was observed for the case of the GGSS-1 and GGSS-2 because of a higher strain levels concentrated right at the end of the GGSS located at the interface of the column to footing. In GGSS-3, the intentional debonding which was provided over the 8-in length of the footing dowel bars improved the strain localization and postponed the premature fracture of the bars.

The backbone curve, or the so-called cyclic envelope, was constructed by joining the peak values of the first cycle for each drift ratio. **Figure 4-28** shows the cyclic envelopes for all column-to-footing test specimens. It is observed that the overall force-displacement performance of all 4 test specimens is similar up to the 1% drift ratio. Specimens GGSS-1 and GGSS-3 had the greatest strength capacities among all. This was mainly attributed to the presence of the GGSS in the column base which led to a partial transition of the flexural action to the section right above the GGSS. However, a higher axial load was applied to the GGSS-1 unintentionally which resulted in a larger lateral force capacity for this test specimen. This axial load was 60%

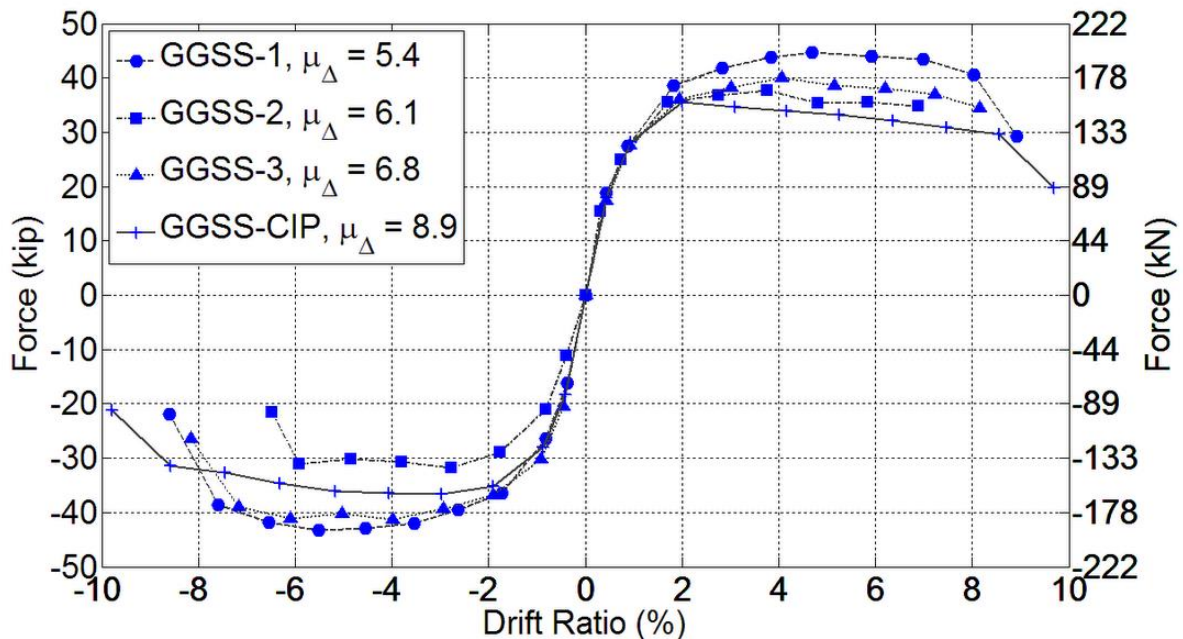


Figure 4-28. Force-displacement response of column-to-footing test specimens.

larger than the axial load applied to the GGSS-3, including the different concrete compressive strengths used for the two specimens. Comparing GGSS-3 to the GGSS-CIP, it is observed that the lateral force capacity of the GGSS-3 was 13% larger than that of the GGSS-CIP, on average for both push and pull directions.

#### *4.2.5.2 Stiffness Degradation*

The effective stiffness was calculated in each cycle using the peak displacement values and the corresponding forces. The average of the stiffness values was then obtained for both cycles of every drift ratio. **Figure 4-29** displays the average effective stiffness at each drift ratio for all specimens. A similar trend was noted in the stiffness reduction per drift ratio for all specimens. The degradation rate was much higher during the first few cycles; mainly because of column rebar yielding. For example, there was a 60% reduction in GGSS-2 stiffness by the end of the 2% drift ratio. The stiffness degradation graph indicates that the precast test specimens had similar average component stiffness characteristics, and suggests that the GGSS in the column base or footing did not change the overall stiffness degradation rate.

#### *4.2.5.3 Energy Dissipation Capacity*

The cumulative hysteretic energy capacity for all column-to-footing test specimens is shown in a same graph in **Figure 4-30**. As observed, the rate of this quantity which is directly associated with the area under the hysteretic loops increases with an increase in the drift ratio up to the failure drift ratio, for all test specimens. **Figure 4-30** shows that all four test specimens had a very similar hysteretic energy dissipation capacity up to the 3% drift ratio, after which GGSS-CIP and GGSS-2 had a slightly better performance. This implies that the GGSS-2 which had the GGSS inside the footing had wider and more stable hysteresis loops that compared well with the cast-in-place specimen, i. e. the GGSS-CIP.

Equivalent viscous damping is another quantity used to evaluate the relative energy dissipation capacity of systems under cyclic loads. The equivalent viscous damping offers more information about the hysteretic response of the system since both the hysteretic and strain energy are included in this method. The equivalent viscous damping ratio ( $\xi_{eq}$ ) was obtained as

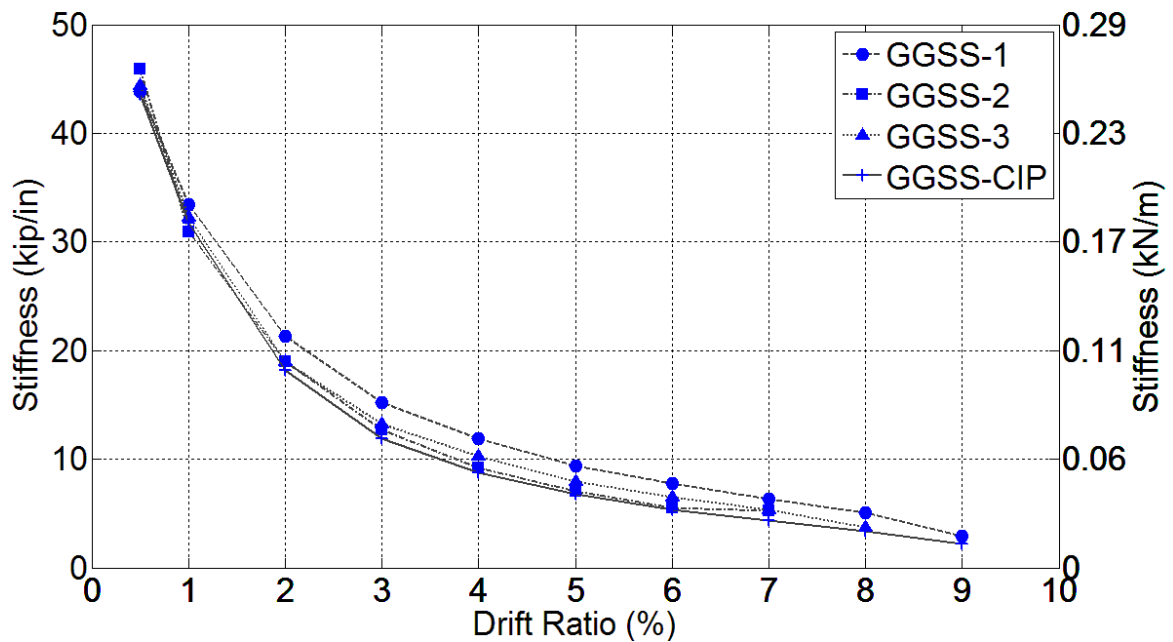


Figure 4-29. Stiffness degradation for column-to-footing test specimens.

the ratio of the hysteretic energy to the energy of the equivalent viscous system as defined in Equation (5) [23].

$$\xi_{eq} = \frac{E_D}{4\pi E_{S0}} \quad (5)$$

where  $E_D$  and  $E_{S0}$  are the area inside the hysteresis loop and the strain energy, respectively.

**Figure 4-31** presents the average  $\xi_{eq}$  of both cycles for each drift ratio. In the inelastic region of the response, which begins after completion of the 1% drift ratio,  $\xi_{eq}$  for all specimens increases with an increase in the drift ratio. At the 8% drift ratio, GGSS-CIP had a  $\xi_{eq}$  of 31% which indicates a reasonable value for a reinforced concrete component with a good seismic detailing. It is evident that GGSS-2 and GGSS-CIP had greater  $\xi_{eq}$  during all drift ratios. For instance,  $\xi_{eq}$  at 6% drift ratio was 17%, 26%, 20%, and 24% for the GGSS-1, GGSS-2, GGSS-3, and GGSS-CIP, respectively. This implies that a relatively superior energy dissipation capability is achieved when the GGSS is incorporated in the footing, rather than the column base.

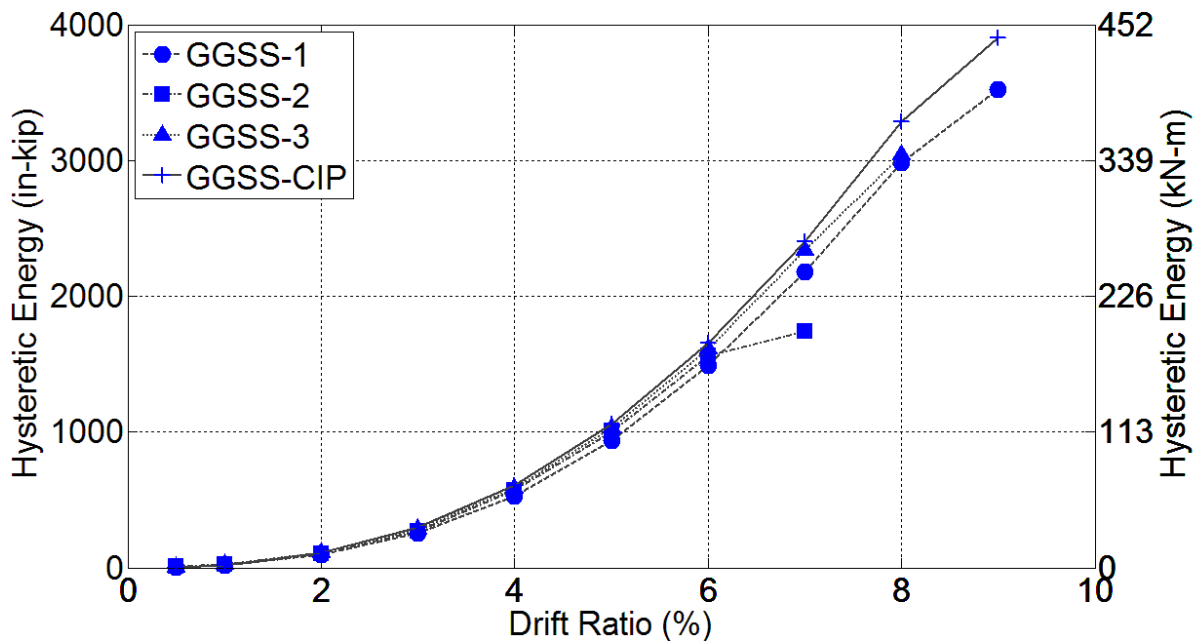


Figure 4-30. Cumulative hysteretic energy for column-to-footing test specimens.

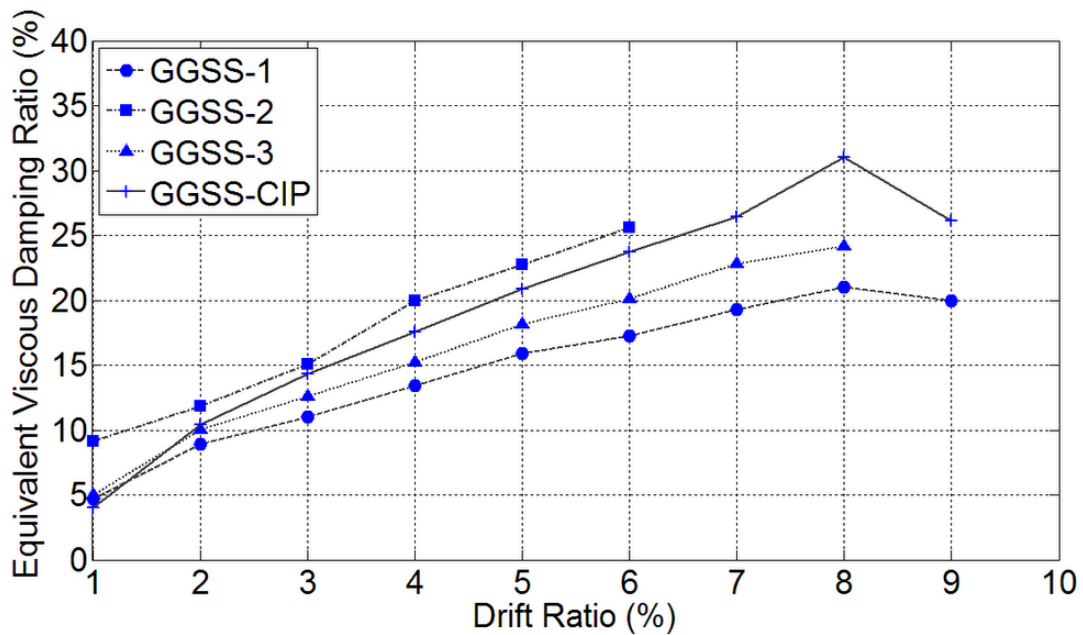


Figure 4-31. Equivalent viscous damping for column-to-footing test specimens.

### 4.3 Response of Column-to-Cap beam Connections

The measured response of the column-to-cap beam connections is presented in this section. Four evaluation methods described in **Section 4.1** will be utilized to study the results obtained from each test. A comparative study will also be presented at the end of this section, emphasizing the similarities and differences that exist between the specimens.

#### 4.3.1 FGSS-1 Results

##### *4.3.1.1 Experimental Observations and Damage States*

The hysteresis response of FGSS-1 is shown in **Figure 4-32** which includes two major damage states, i.e. cracking and spalling of concrete, and rebar pull-out failure. The pinched hysteresis loops achieved for this specimen indicate that the overall force-displacement performance of FGSS-1 is controlled by bond-slip characteristics of the FGSS system. In addition to pinching that occurred due to excessive slippage of the cap beam dowel bar in the FGSS, rebar slippage introduced another type of disruption in the unloading branch of the response in the push direction. This condition was attributed to the closure of the gap originally formed as a result of bond deterioration and the consequent bar slip. This gap closure phenomenon is readily visible on the unloading branch of the hysteresis loops for the 4%, 5%, 6% drift ratios in the push direction.

The lateral force peaked at the 5% and 3% drift ratio in the push and pull direction, respectively. A gradual strength reduction or cyclic strength deterioration was noted as a result of bond deterioration between the dowel bar and the grout inside the FGSS. The test was terminated at the end of the 6% drift ratio due to a load reduction of 20% and 30% for the push and pull direction, respectively. Failure of FGSS-1 was caused by excessive bar slippage and the consequent pull-out of rebar from the FGSS.

The first crack formed at the bed grout section, accompanied by another crack just above the FGSS, during the first cycle of the 1% drift ratio. Both cracks were hairline and not measurable when the column returned to the stationary condition. All major cracks developed by the end of the 3% drift ratio. Spalling initiated at the corners of the octagonal column during the

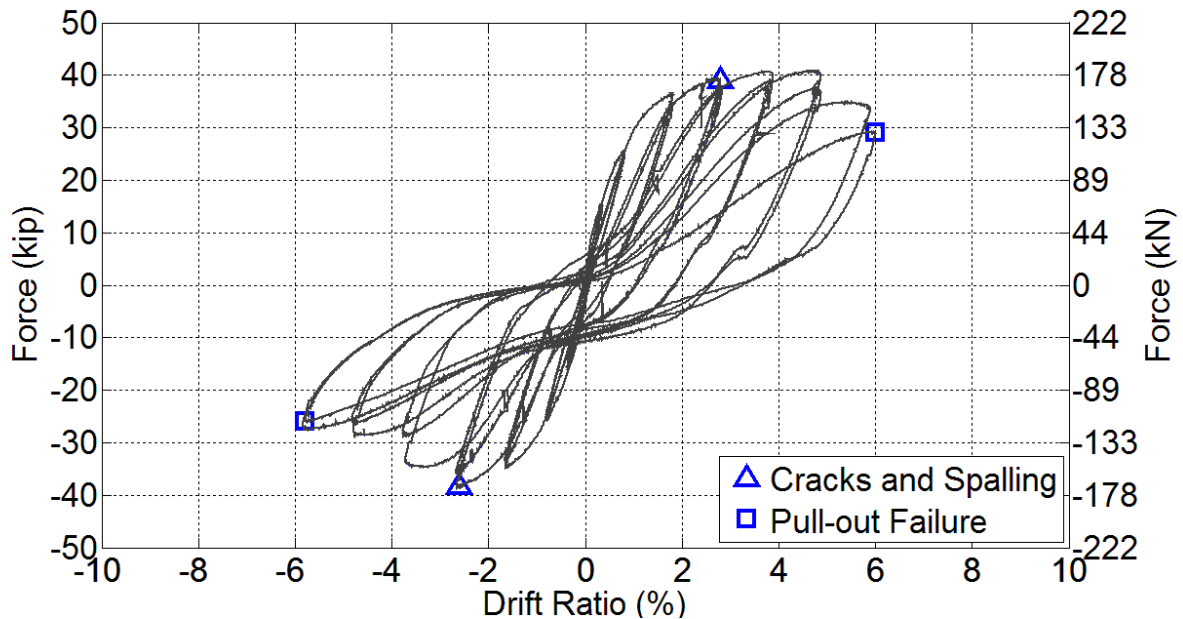


Figure 4-32. Hysteresis response of FGSS-1 with damage states.

first cycle of the 3% drift ratio. The largest crack, which had been formed at the bed grout section during the previous drift ratios, turned into a gap at the interface of the column to the cap beam during the 3% drift ratio. This is evident in **Figure 4-33(a)** that shows the gap opening while the column was at the peak displacement of the 3% drift ratio. **Figure 4-33(b)** displays the damage state at the end of this drift ratio.

Cracks widened and concrete spalling progressed at higher drift ratios. During the 6% drift ratio, the cone shape of the expelled grout became visible when the test specimen was at maximum displacement in the pull direction. This condition is presented in **Figure 4-33(c)**. The test was terminated after completion the 6% drift ratio due to bond deterioration, and subsequent rebar pull-out. The height of the spalled concrete region was 8in. and 12in. on the west and east side of the column, respectively. The spiral was partially exposed within the column end and the bed grout was crushed at the column peripheral. The permanent opening at the bed grout had a residual gap equal to 0.1 in. **Figure 4-33(d)** shows the damage state at the end of the test.

The cap beam remained intact with only a few scattered minor cracks in the joint region. The test-day compressive strength of the concrete and grout was 6.2 ksi and 13.3 ksi, respectively.



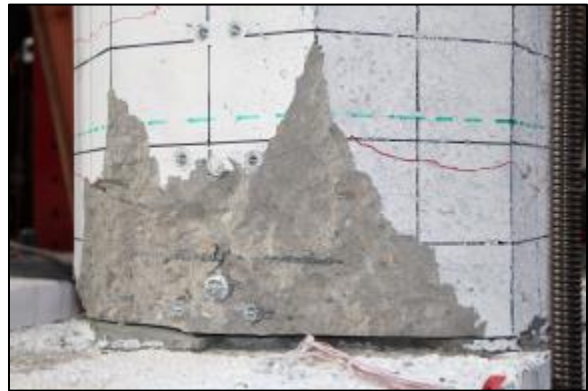
(a) Bed grout opening at 3% drift ratio (peak).



(b) Damage state at 3% drift ratio.



(c) Bar pull-out during 6% drift ratio.



(d) Damage state at end of test.

Figure 4-33. FGSS-1 visual observations.

#### 4.3.1.2 Ductility Capacity and Plastic Rotation Capacity

The average backbone curve was constructed in accordance with the method described in **Section 4.1.2**, along with the idealized elasto-plastic curve. **Figure 4-34** depicts the two plots in addition to the parameters required to obtain the displacement ductility. The effective yield displacement and force for FGSS-1 were 1.08 in. and 35.35 kip, respectively. The ultimate displacement, corresponding to a 20% strength drop, was 5.32 in., resulting in a displacement ductility of 4.9.

**Figure 4-35** displays the moment-plastic rotation relationship up to test termination. The plot shows that GGSS-1 had a plastic rotation of 0.0371 rad at the 5% drift ratio, before excessive strength reduction.

### 4.3.1.3 Cumulative Energy Dissipation

The cumulative hysteretic energy versus drift ratio is plotted in **Figure 4-36**. There was an increase in energy dissipation with an increase in the drift ratio as the specimen underwent inelastic performance. The cumulative hysteretic energy was found to be 218 in-kip

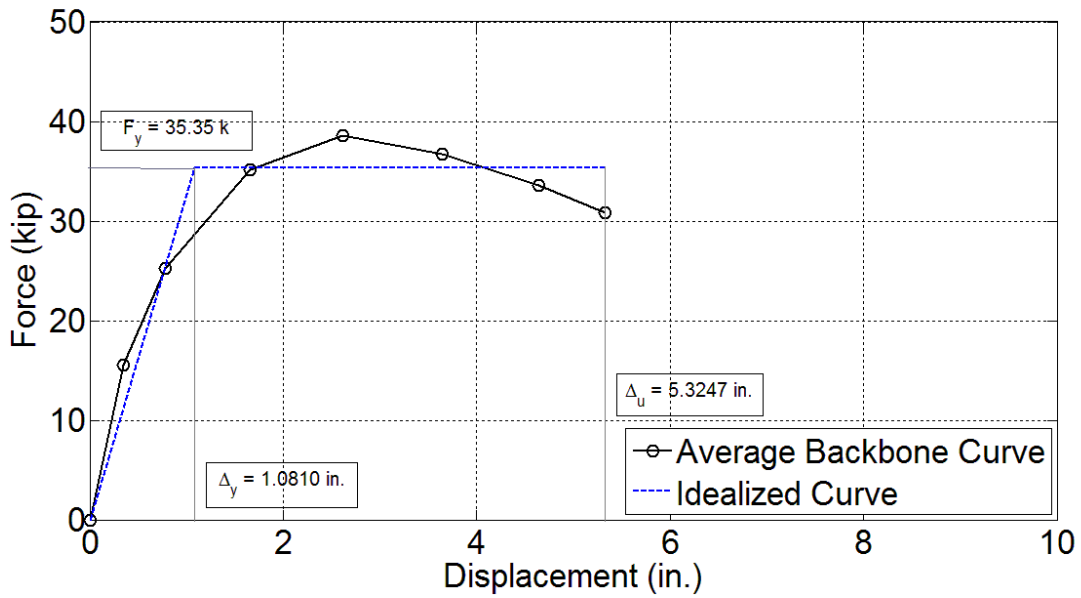


Figure 4-34. Average backbone curve and displacement ductility for FGSS-1.

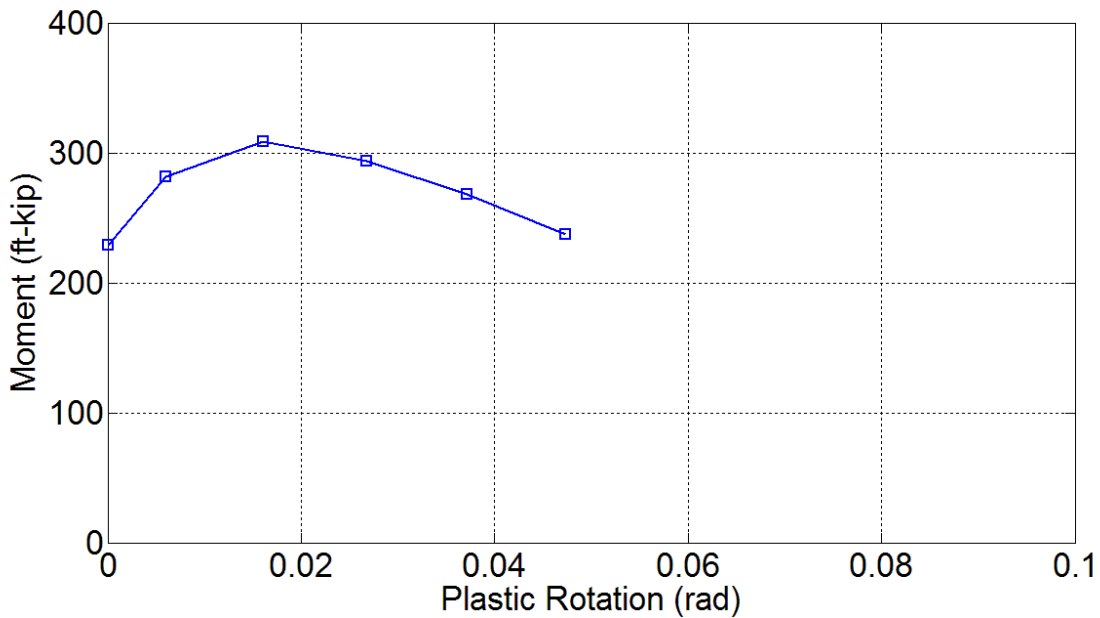


Figure 4-35. Plastic rotation capacity for FGSS-1.

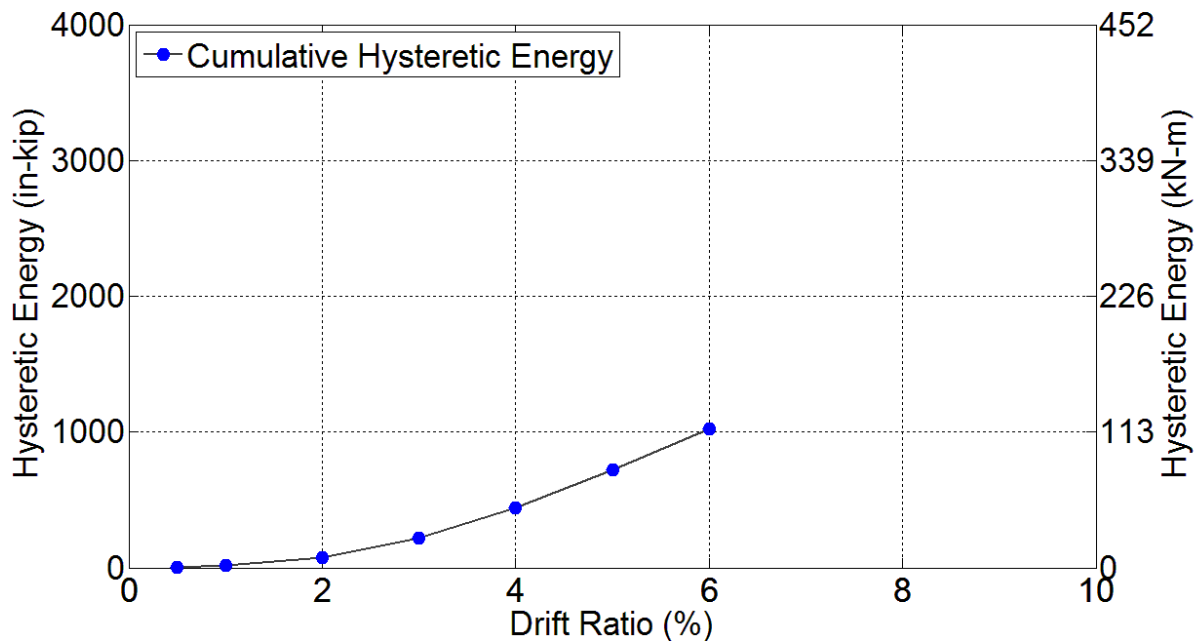


Figure 4-36. Energy dissipation capacity of FGSS-1.

and 1021 in- kip at 3% and 6% drift ratio, respectively.

#### 4.3.1.4 Column Curvature Profile

The normalized curvature distribution along the column base is shown in **Figure 4-37**. The curvature profile indicated that the curvature capacity is a minimum over the FGSS region and flexural action was concentrated at sections above and below the FGSS. An examination of this curvature profile revealed that the column rebar did not develop considerable stresses for the portion that was embedded in the FGSS. The asymmetric curvature profile of the FGSS-1 could be attributed to an early bond deterioration of the east cap beam dowels inside the connectors. Considering the force-displacement response of this test specimen which was shown in **Figure 4-32**, a drastic strength drop is noted after the 3% drift ratio. This implies a gradual strength deterioration as a result of severe bond deterioration which caused a more pronounced rocking behavior than bending and thus, smaller curvature values when the column was in pull direction.

Strain gauges located on the extreme longitudinal bars, in the column base and within the joint core, covered an area with a depth of 7 in. into the cap beam and 16 ¼ in. up above the column base. These strain gauges showed that both extreme bars yielded over the whole range

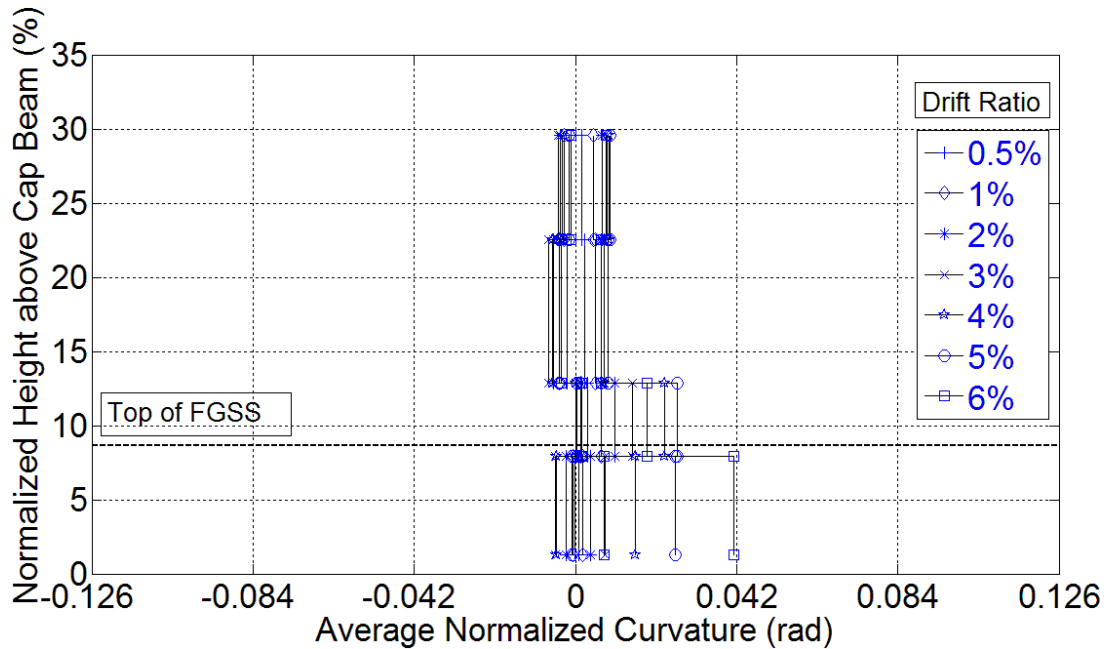


Figure 4-37. Normalized curvature distribution for FGSS-1.

covered by strain gauges, except for the initial 5-in. portion of the field dowels which was embedded and confined inside the FGSS.

#### 4.3.2 FGSS-2 Results

##### 4.3.2.1 Experimental Observations and Damage States

**Figure 4-38** depicts the lateral force-displacement performance of FGSS-2 including three damage states which were: (1) crack formation and initiation of concrete spalling, (2) fracture of rebar, and (3) rebar pull-out as a result of bond-slip. Hysteresis loops were relatively wide and stable compared to FGSS-1, without any considerable strength degradation before the rebar fracture or pull-out, in the last drift ratio. The peak lateral force of 34.7 kip and 36.3 kip occurred at the 4% and 5% drift ratio, in the push and pull direction, respectively. The column west rebar fractured in the first cycle of the 7% drift ratio, while column east bars underwent excessive slippage that resulted in a considerable strength reduction. Ultimately, test termination was enforced after completion of the 7% drift ratio, because a strength drop of 42% and 45% occurred in the lateral force capacity, as a result of east rebar fracture and west rebar pull-out.

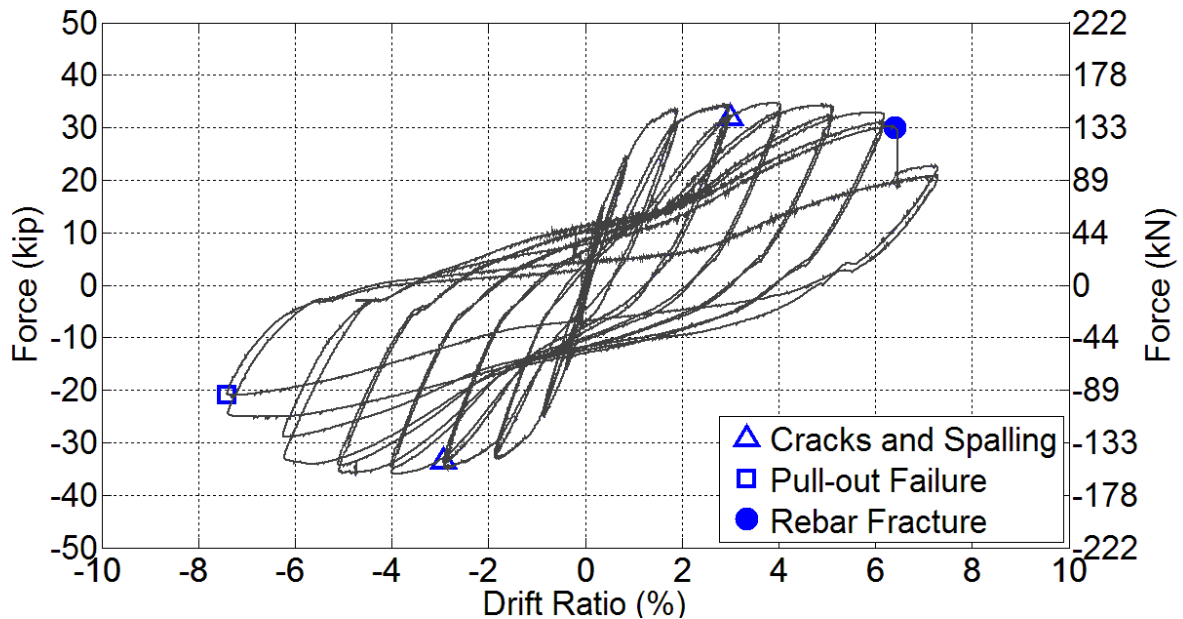


Figure 4-38. Hysteresis response of FGSS-2 with damage states.

This was a unique failure mode because it contained both a ductile failure and a bond-slip failure. The gap closure phenomenon described for the FGSS-1 test specimen was observed for this specimen too, an indication of excessive rebar slip at the 4% drift ratio.

A hairline flexural crack formed at a section 12 in. above the column base during the 0.5% drift ratio. During the next drift ratio of 1%, this crack had a width of 0.002 in. Two more flexural cracks developed at 20 in. and 28 in. above the column end, in the same drift ratio.

More cracks developed during the 2% and 3% drift ratio including one at the bed grout. There were overall seven major flexural cracks that formed along the column by the end of the 3% drift ratio. The width of the crack that was formed during the 2% drift ratio at a section 8 in. from the column base, measured 0.03 in. at the end of the 3% drift ratio. Concrete cover spalling initiated during this drift ratio with a height of 8 in. on the column east side. Cracks opened further and concrete spalling intensified after the 3% drift ratio up to test termination. Flexure-shear cracks formed on the north and south side of the column during the 5% drift ratio, while the representative crack at 8 in. above the column base had a width of 0.04 in. Spalling became deeper and wider during the 6% drift ratio and a considerable strength reduction was noted at the

end of the second cycle in the push direction. This was attributed to the bond deterioration between the grout and the embedded column dowel.

The column extreme west bar broke at the end of the first cycle of the 7% drift ratio, whereas the east bar did not fracture; however, the drop in the lateral force capacity for the pull direction implied that a bond-related phenomenon had caused a sudden reduction in strength. Post-test observations showed that the spiral became exposed near the column end, and the largest flexural crack which was found 4 in. above the column base measured 0.06 in. The location of the rebar fracture was spotted 1 in. above the column base, right below the spiral. Similar to the previous test specimens, low cycle fatigue was the cause of rebar fracture, as a result of successive bending and re-straightening of the column extreme bars. A permanent gap with a depth of 0.125 in. and 0.0625 in. remained at the bed grout section, on the east and west side of the column, respectively. **Figure 4-39** shows the damage state at the 3% and 7% drift ratio.

#### *4.3.2.2 Displacement Ductility Capacity and Plastic Rotation Capacity*

A displacement ductility of 5.8 was obtained for this test specimen using the standard procedure described in **Section 4.1.2**, as shown in **Figure 4-40**. The idealized curve was constructed to achieve all parameters required to compute the displacement ductility capacity. The ultimate displacement of 6.50 in. was associated with a 20% drop in the lateral force capacity of this test specimen. Effective yield strength and yield displacement were obtained as 33.29 kip and 1.11 in., respectively.

**Figure 4-41** displays the moment-plastic rotation relationship up to test termination. The plot shows that FGSS-2 had a plastic rotation of 0.0505 rad occurred at the 6% drift ratio. This was associated with a condition of negligible strength degradation.



(a) Damage state at 3% drift ratio: cracks and spalling.



(b) Damage state at 7% drift ratio: cracks, spalling, and exposed spiral.

Figure 4-39. FGSS-2 visual observations.

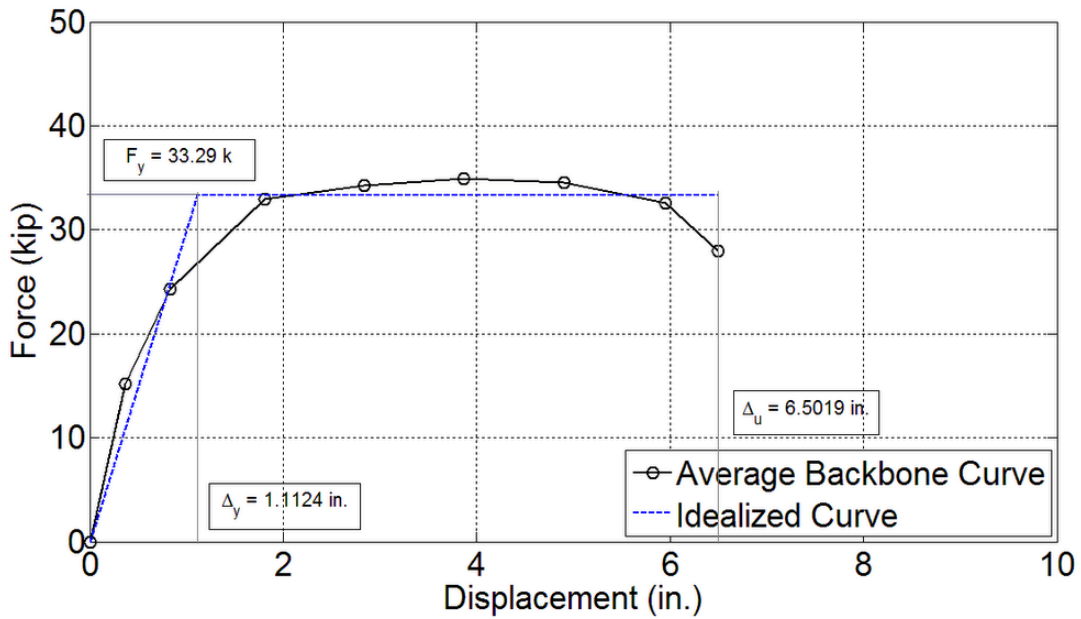


Figure 4-40. Average backbone curve and displacement ductility of FGSS-2.

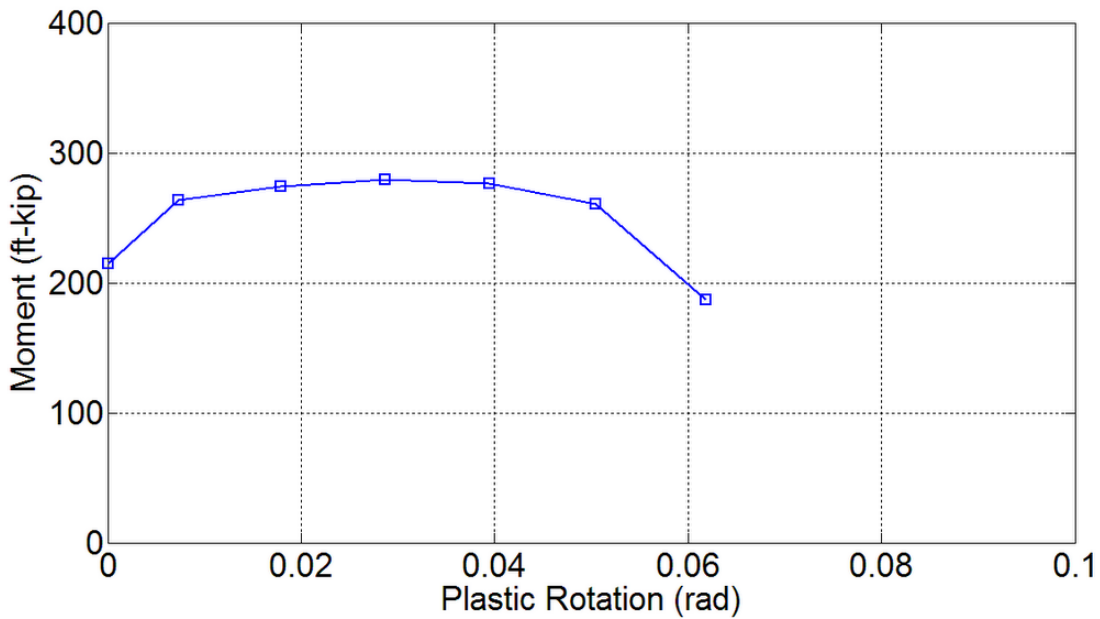


Figure 4-41. Plastic rotation capacity for FGSS-2.

#### 4.3.2.3 Cumulative Energy Dissipation

**Figure 4-42** shows the cumulative hysteretic energy per drift ratio. FGSS-2 dissipated energy continuously, up to the end of the 6% drift ratio. In the 7% drift ratio a slightly lower

dissipation rate was achieved because of the west rebar fracture and pull-out of the east rebar. The cumulative hysteretic energy was found to be 241 in-kip and 1859 in-kip for the 3% and 7% drift ratio, respectively.

#### *4.3.2.4 Column Curvature Profile*

Without the presence of the FGSSs in the column base, a very good curvature distribution was achieved for this test specimen, as presented in **Figure 4-43**. This is similar to the curvature distribution which commonly exists in cast-in-place construction with either well-detailed standard lapped splices or a monolithic construction, in which no disruption is introduced to the natural stress transfer between the adjoining components. Neglecting the asymmetric curvature distribution for the push and pull direction, this curvature profile resembles an acceptable distribution of curvature demand along the column plastic hinge region, with the highest curvature values at the column base where moment is also a maximum, and a gradual decrease in curvature values when moving towards the top of the column.

The asymmetric curvature distribution started during the 3% drift ratio, as seen in the curvature profile. This was mainly because of a movement of one of the LVDT fixtures located on the column east side, as a result of a damage occurred in the plastic hinge zone during the 3% drift ratio. The movement of this LVDT fixture caused an error in the readings of the two bottom LVDTs on the east side of the column, resulting in a minor error in the curvature values of the first two curvature segments.

Strain gauges located on the extreme longitudinal bars, in the column base and within the joint core, covered an area with a depth of 13 in. into the cap beam and 18 in. up above the column end. These strain gauges showed that the extreme column dowels yielded starting at 5 in. from the tip of the column dowel bars which was confined within the FGSS connectors, or in other words, 2 in. into the cap beam from the column-to-cap beam interface. On the contrary, the cap beam dowel bars did not perform inelastically and strain values remained below the rebar yield strength.

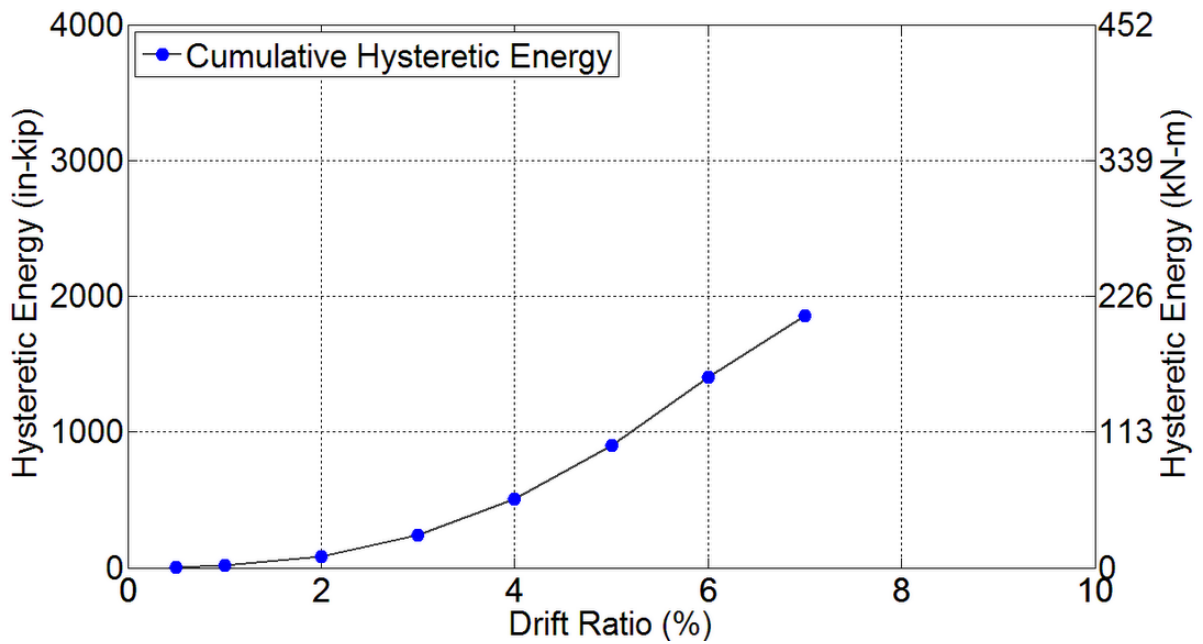


Figure 4-42. Energy dissipation capacity of FGSS-2.

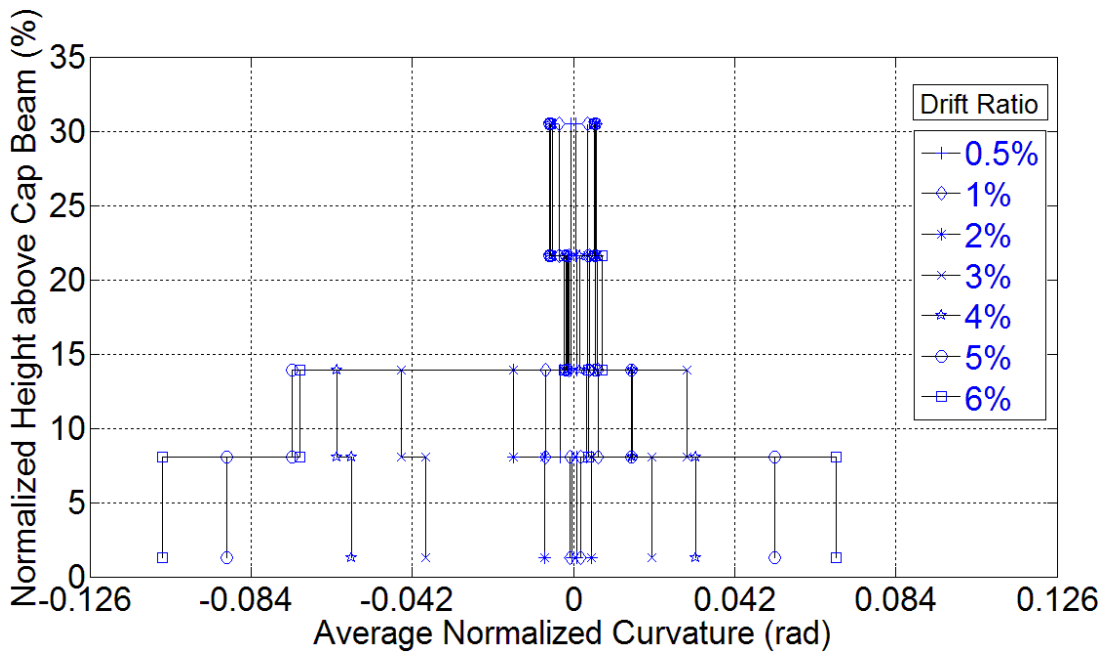


Figure 4-43. Normalized curvature distribution for FGSS-2.

### 4.3.3 FGSS-3 Results

#### *4.3.3.1 Experimental Observations and Damage States*

Prior to the application of the loading protocol to FGSS-3, an incident occurred in which the column head was accidentally pushed 1.6 in. monotonically. This pre-test condition led to exceeding the predicted yield displacement of the column, and caused a few crack formations within the plastic hinge zone, along with minor concrete cover spalling at the column corners on the east side only. **Figure 4-44** shows the state of damage before the intended test protocol was implemented; five flexural cracks developed including the crack formed in the bed grout at the interface. These cracks were either hairline or smaller than 0.009 in. The concrete spalling had a maximum vertical dimension of 4 in. at the corners and 2 in. elsewhere. The lateral force-displacement plot, displayed in **Figure 4-45**, indicates that the hysteretic performance was affected by the pre-test condition especially for the push direction in which the tension bars had partially performed beyond their yield point. This is evident in terms of both the lateral force capacity and hysteresis loops for the push direction as compared to the pull direction. It was noted that the maximum lateral force capacity, which occurred at 4% drift ratio, was 37.2 kip and 44.8 kip for the push and pull direction, respectively. The hysteresis loops had a superior condition in the pull direction than the push direction, implying a higher dissipation



Figure 4-44. Pre-test condition of FGSS-3.

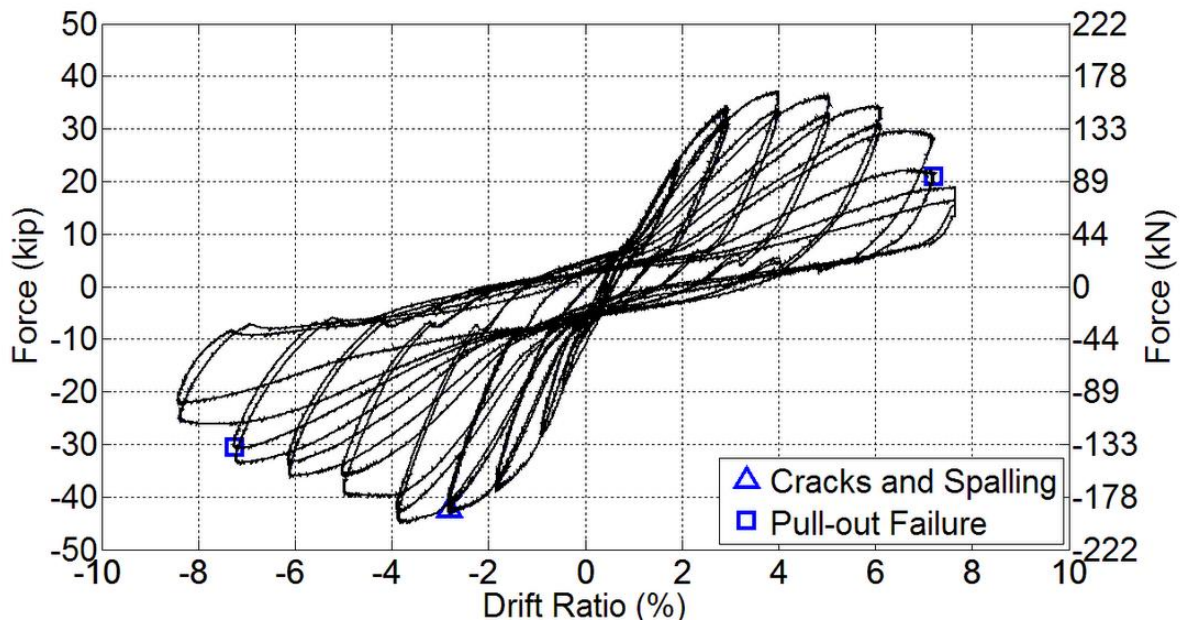


Figure 4-45. Hysteresis response of FGSS-3 with damage states.

capacity for the pull direction as the column tension bars were less affected by the incident. The gap closure that was noted for the previous two precast column-to-cap beam specimens appeared in the hysteresis plot during the unloading portion of the 2% drift ratio for the push direction, and the 3% drift ratio for the pull direction.

Cyclic strength degradation occurred when the strength peaked at 4% drift ratio. This was associated with the gradual bond deterioration within the FGSS and the consequent rebar slip. At the end of the 7% drift ratio, the reduction in the lateral force capacity was more than 20%, hence the specimen was considered to have failed. However, testing continued for one more drift ratio to observe the consequences of severe bond failure.

Visual observations were made at the end of each drift ratio to document the damage progression introduced to the test specimen. Because of the pre-test condition, no new damage was inflicted on the column base, until the 2% drift ratio, which was the first drift ratio to exceed the 1.6-in. pre-test accidental monotonic displacement. That is, the size of the crack or spalling (on the damaged side) did not increase by the end of the 2% drift ratio. Superficial spalling—on the undamaged column side—initiated at the 3% drift ratio at the corners of the octagonal column. In addition, diagonal hairline cracks formed in the joint area of the cap beam. During the

4% drift ratio, spalled concrete cover became larger on the west side and a crack width equal to 0.01 in. was documented for a crack previously developed 14 in. above the column base. The state of damage at the end of the 4% drift ratio is presented in **Figure 4-46**.

The expelled grout cone at the opening of the FGSS became visible when the column head was at peak displacement in the 5% drift ratio. An in-cycle sudden force drop was noted simultaneously suggesting that the cap beam dowel bars started to pull out from the FGSS. The transverse reinforcement became exposed at the end of the 6% drift ratio, while the grout cones were visible at the peak displacement of the 7% drift ratio. Considering that the size of the cracks remained unchanged during the last few cycles along with the excessive rebar slip in the FGSS, a rocking mechanism was more pronounced than bending action. This could be noted in **Figure 4-47** that presents the column at the maximum pull displacement during the 8% drift ratio when the extreme east cap beam dowel is visible at the interface and the grout cone for the intermediate cap beam dowel is exposed.



Figure 4-46. Damage state for FGSS-3 at 4% drift ratio.

The test was terminated at the end of the 8% drift ratio after a noticeable reduction in lateral force capacity. The crack at 14 in. above the column base had a width of 0.014 in., and the permanent gap at the interface measured between 1/16 in. and 5/16 in.; the height of the spalled region was 8 in. on both sides of the column. **Figure 4-48** shows the damage state at the end of the 8% drift ratio.

The cap beam performed in the elastic range of the response and without major damage. The test-day compressive strength of the concrete and grout was 8.2 ksi and 11.7 ksi, respectively.

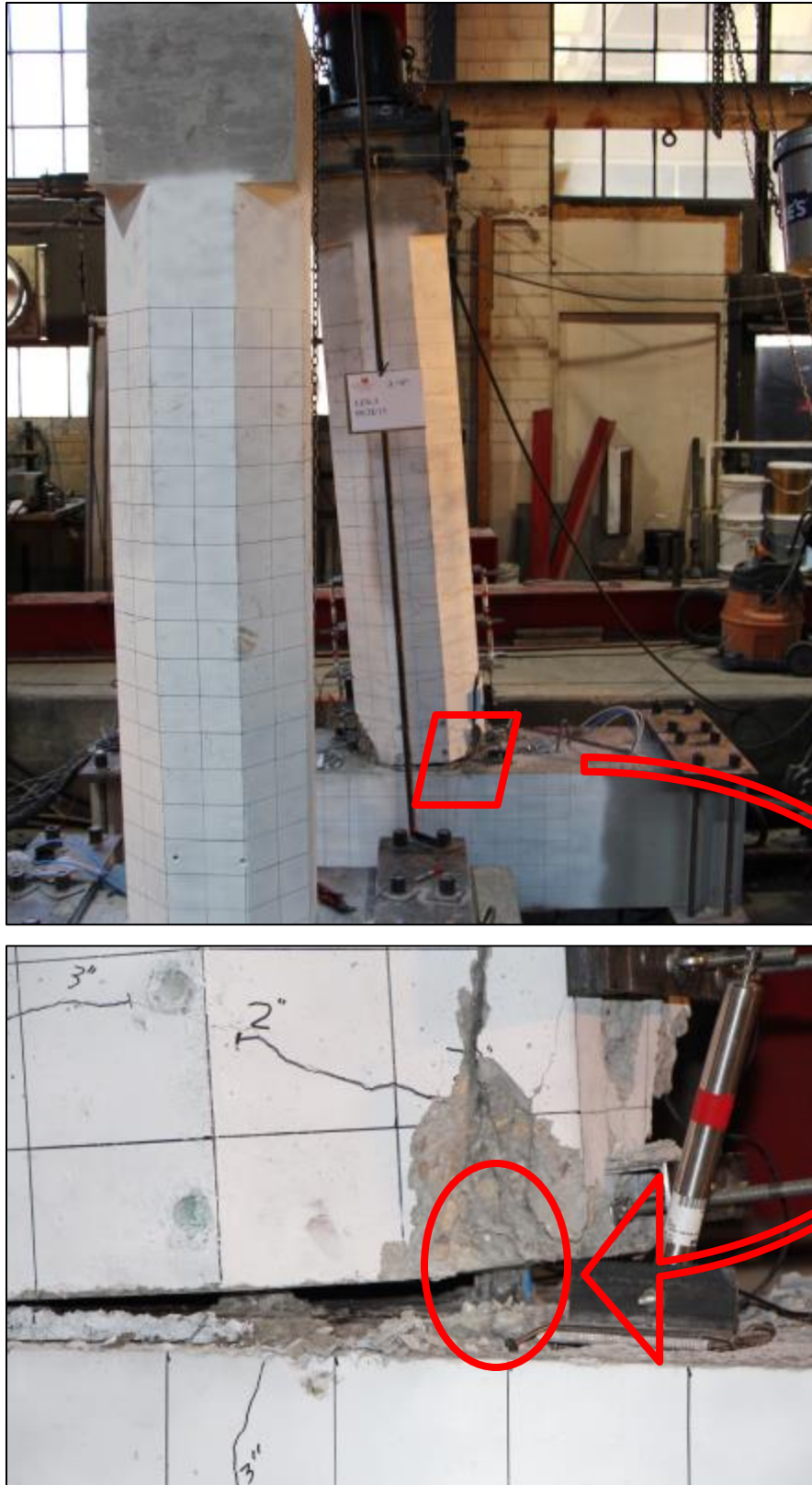


Figure 4-47. FGSS-3 cap beam dowel pull-out at 8% drift ratio.



Figure 4-48. Damage state for FGSS-3 at end of test: cracks and spalling, permanent gap.

#### 4.3.3.2 Displacement Ductility Capacity and Plastic Rotation Capacity

The average backbone curve was obtained to construct the cyclic envelope of the hysteretic response of FGSS-3. The idealized elasto-plastic curve was superimposed to obtain the ductility capacity using the effective yield properties of the column and the ultimate displacement corresponding to a lateral force equal to 80% of the maximum strength. The effective yield displacement was 2.08 in., the effective yield force was obtained as 36.82 kip, and the ultimate displacement was found to be 6.47 in. The yield displacement is obviously larger than anticipated because of the accidental monotonic displacement. As a consequence of this, a displacement ductility equal to only 3.1 was achieved for this test specimen. **Figure 4-49** shows both curves on the same graph.

**Figure 4-50** shows the moment-plastic rotation relationship up to test termination. The graph shows that FGSS-3 had a plastic rotation of 0.0396 rad which occurred at the 6% drift ratio, prior to a noticeable strength reduction that occurred during the 7% drift ratio.

#### 4.3.3.3 Cumulative Energy Dissipation

Similar to the other column-to-cap beam test specimens, FGSS-3 dissipated considerable amount of energy through inelastic response to the simulated seismic forces. Although this specimen underwent a pre-test damage condition, FGSS-3 had a regular cyclic response by dissipating energy with an increasing rate up to the 6% drift ratio. Beyond this level the hysteretic energy capacity reduced as a result of a successive rebar slip and gradual pull-out from

the FGSS that was embedded in the column end. This test specimen had a cumulative dissipated energy of 185 in-kip, 992 in-kip, and 1561 in-kip at 3%, 6%, and 8% drift ratio, respectively.

**Figure 4-51** shows the cumulative hysteretic energy per drift ratio.

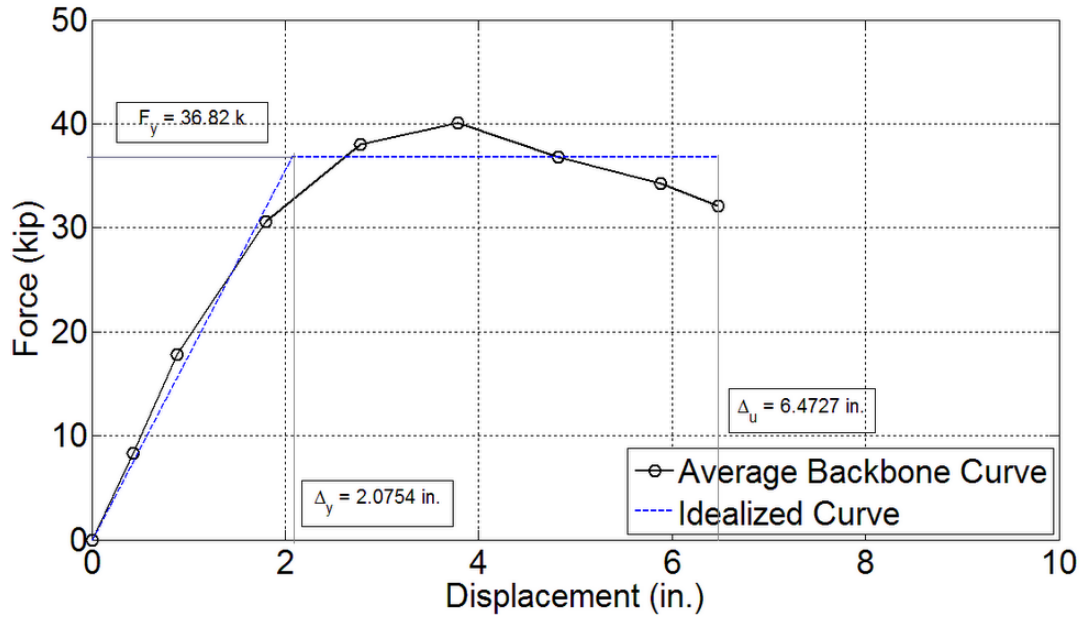


Figure 4-49. Average backbone curve and displacement ductility of FGSS-3.

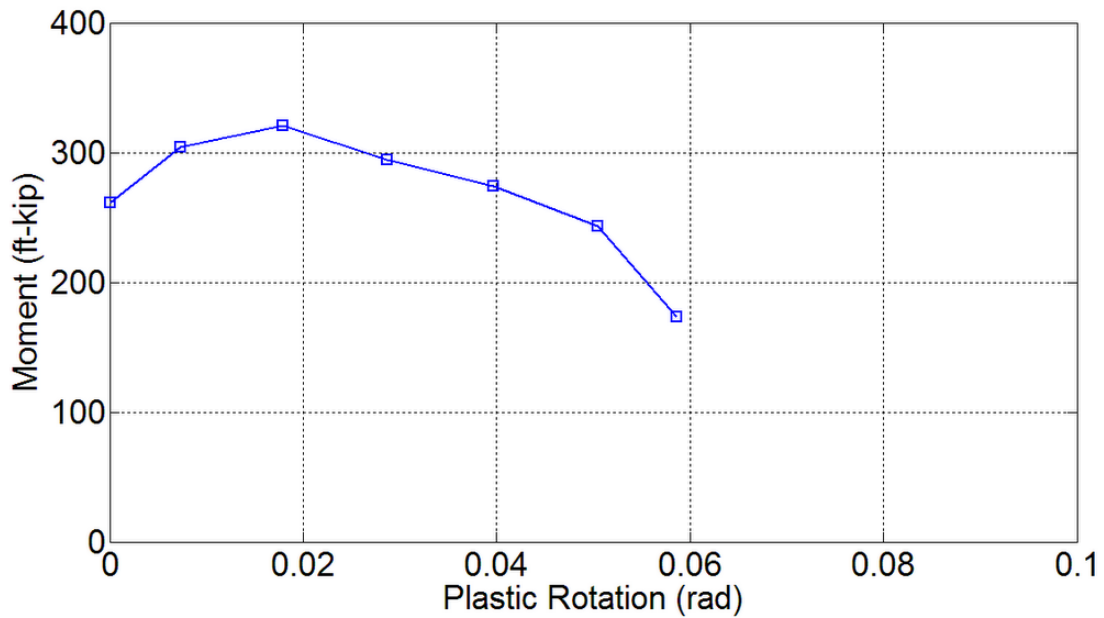


Figure 4-50. Plastic rotation capacity for FGSS-3.

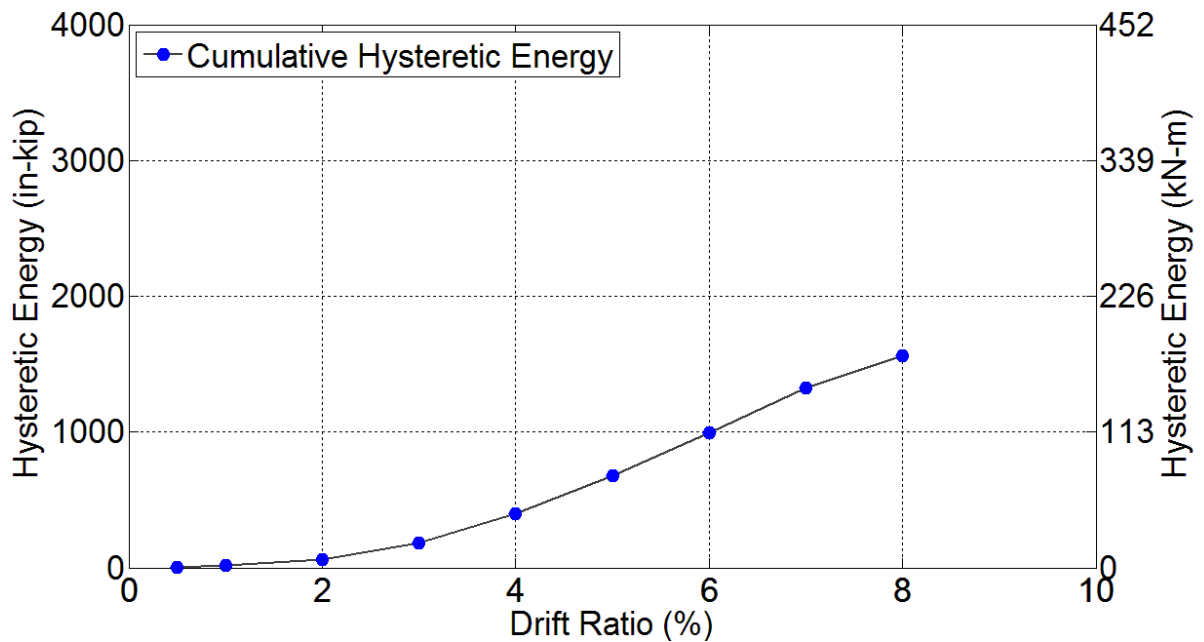


Figure 4-51. Energy dissipation capacity for FGSS-3.

#### 4.3.3.4 Column Curvature Profile

The normalized curvature distribution along the FGSS-3 column base is displayed in **Figure 4-52**. Similar to the curvature profile observed for FGSS-1, it is apparent that bending action is concentrated at two sections above and below the FGSS. Curvature capacity is a minimum along the FGSS implying that this region had a higher rigidity compared to the remainder of the column.

Strain gauges located on the extreme longitudinal bars, in the column base and within the joint core, covered an area with a depth of 9 ½ in. into the cap beam and 16 in. up above the column base. These strain gauges showed that both extreme bars yielded over the whole range covered by strain gauges, except for the initial 5-in. portion of the field dowels which was embedded and confined inside the FGSS.

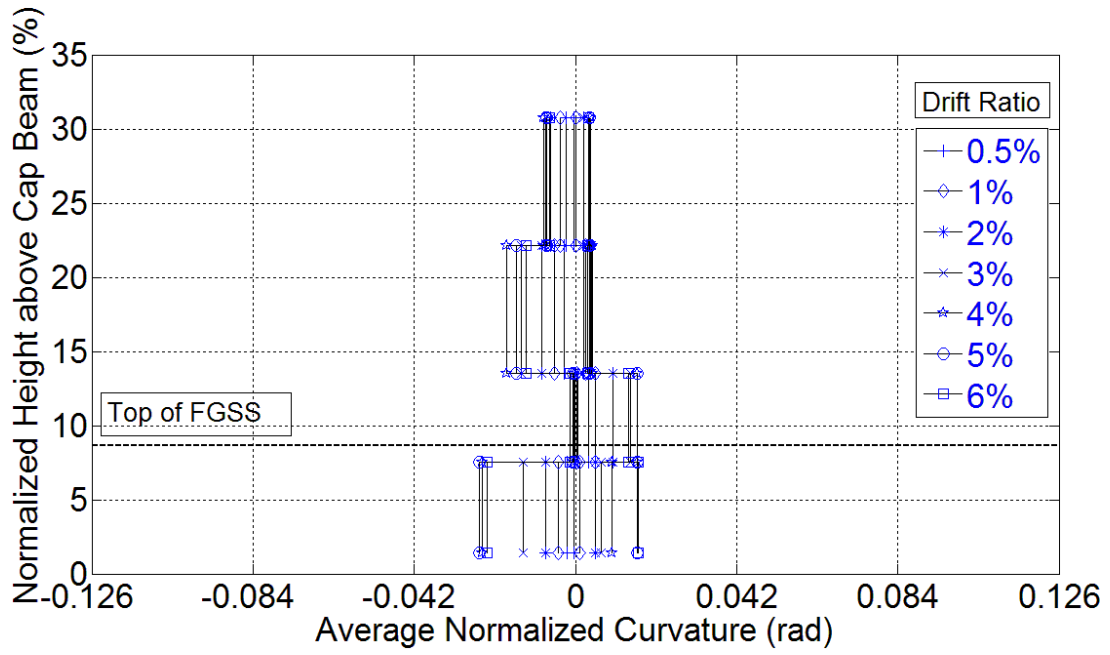


Figure 4-52. Normalized curvature distribution for FGSS-3.

#### 4.3.4 FGSS-CIP Results

##### 4.3.4.1 Experimental Observations and Damage States

The hysteretic response of this test specimen is presented in **Figure 4-53**, in addition to damage states corresponding to: (1) end of major crack formation and beginning of spalling, (2) observation of yield penetration, and (3) rebar fracture. The overall response was satisfactory as a result of the wide and stable hysteresis loops that implied a relatively high energy dissipation capacity. This desirable performance represented a ductile response of a well-detailed reinforced concrete flexural component, under both axial and lateral loading. The lateral load peaked at 37.75 kip during the 2% drift ratio and 33.93 kip during the 3% drift ratio for the push and pull direction, respectively.

This test was terminated at the end of the 10% drift ratio due to the fracture of both extreme east and west column longitudinal column bars. The west rebar fractured when the column top was close to the peak displacement during the first cycle. Subsequently, the bar on the opposite side of the column fractured, during the first pull.

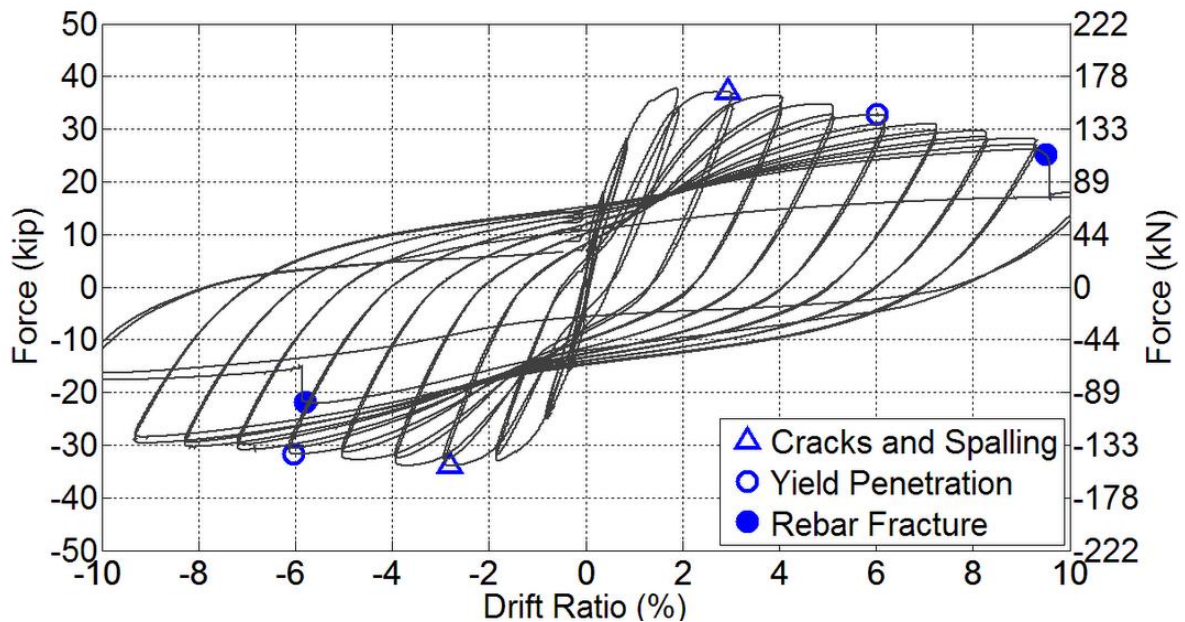


Figure 4-53. Hysteresis response of FGSS-CIP with damage states.

A few hairline flexural cracks appeared as early as the end of the 1/2% drift ratio over a 40-in. long region up from the column base. More hairline flexural cracks developed during the 1% drift ratio, up to 60 in. above the column base. Those cracks which had formed within the lowermost 12-in. portion of the column grew larger in width, during the 2% drift ratio. Also, a relatively large crack, with a width of 0.03 in., formed at the interface of the column-to-cap beam connection. The crack at 12 in. up from the column base had a width of 0.005 in. at the end of this drift ratio. Similar to the precast test specimens, all major flexural cracks developed by the end of the 3% drift ratio and concrete cover spalling began at the corners of the octagonal column. The crack at the interface remained unchanged while the crack at 12 in. up from the column base was 0.01 in. **Figure 4-54** displays the damage state at the end of the 3% drift ratio.

Inclined cracks formed on the north and south side of the column base in the 4% drift ratio. **Figure 4-55** shows the three existing largest cracks within the column plastic hinge region, at the peak displacement condition of the 4% drift ratio. These cracks measured 0.04 in., 0.06 in., and 0.013 in. for the crack at the interface, 6 in. from the column base, and 12 in. from the column base, respectively, when the column returned to the stationary condition.



Figure 4-54. Damage state for FGSS-CIP at 3% drift ratio.

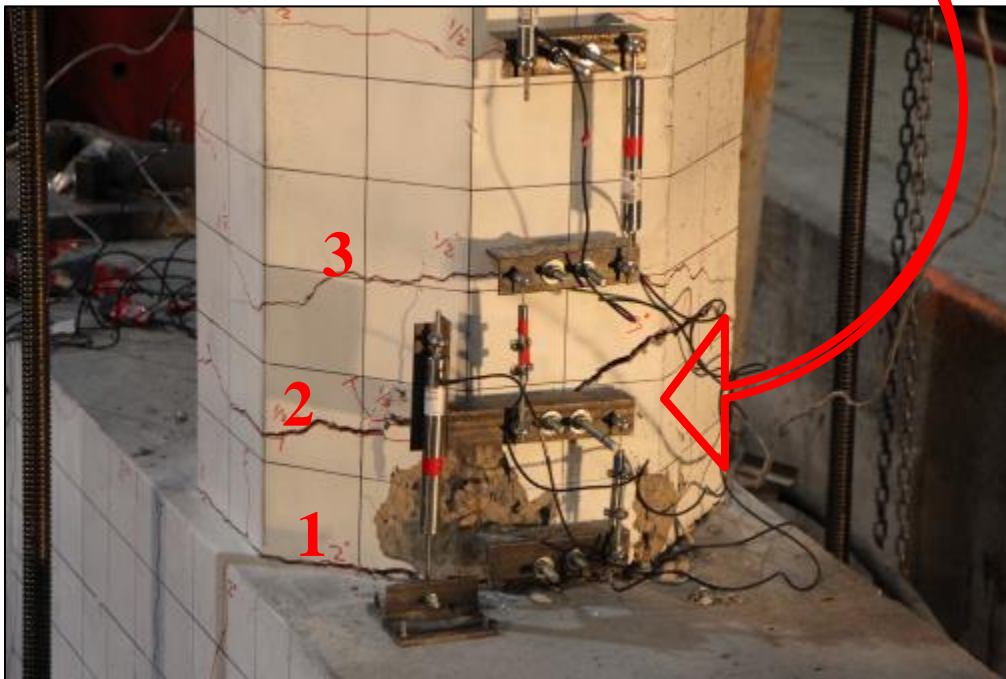
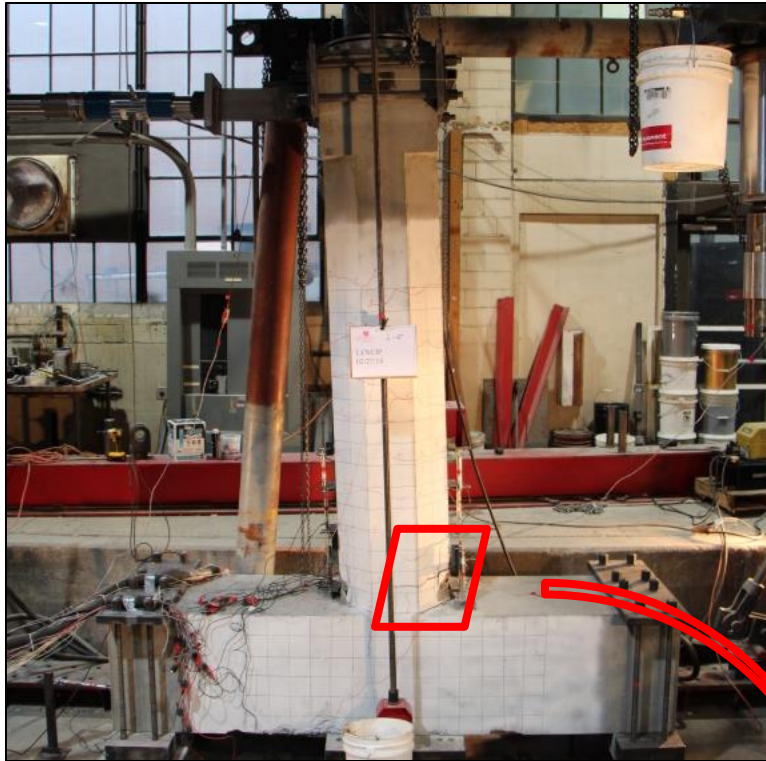


Figure 4-55. FGSS-CIP at peak displacement during 4% drift ratio; largest three cracks.

Yield penetration was noted around the two column extreme bars at the end of the 6% drift ratio. Spalling became wider and deeper, covering the crack developed during the previous cycles. **Figure 4-56** shows the state of damage to the column at the end of the 6% drift ratio. In the 7% drift ratio, the column spiral became visible and the depth of yield penetration increased to 1 1/8 in. The column extreme longitudinal rebar was visible during the 8% drift ratio implying that the concrete cover was completely crushed which led to buckling of the rebar during the next drift ratio.

Low cycle fatigue caused fracture of the column extreme bars on both opposite sides, in the first cycle of the 10% drift ratio. The west column bar fractured in the push direction first, and then the east column bar fractured in the pull direction. Post-test investigation indicated that the fracture of the rebar occurred at 1 in. and 1 1/2 in. above the cap beam, for the west and east column bars, respectively. The spalled region had an effective width of 21 in. and height of 8 in., although the maximum height of the spalled area was 16 in. and 20 in. for the east and west column side, respectively. The cap beam horizontal rebar was revealed as a result of continuous yield penetration of the column rebar. **Figure 4-57** shows the damage state for this test specimen at the end of the test.

The cap beam remained intact with only two minor cracks developed in the joint region during the 2% drift ratio. The test-day compressive strength of the concrete was found to be 6.7 ksi.



Figure 4-56. Damage state for FGSS-CIP at 6% drift ratio: cracks and spalling, yield penetration.



Figure 4-57. Damage state for FGSS-CIP at end of test: cracks and spalling, rebar buckling and fracture.

#### 4.3.4.2 Displacement Ductility Capacity and Plastic Rotation Capacity

The average backbone curve superimposed with the idealized elasto-plastic curve is presented in **Figure 4-58**. The effective yield strength and yield displacement of the FGSS-CIP was 32.33 kip and 0.90 in., respectively, and the ultimate displacement, associated with strength equal to 80% of the peak lateral force, was 8.96 in. Therefore, the displacement ductility of this test specimen was obtained to be 9.9—the most ductile performance among all test specimens.

A plastic rotation of 0.0837 rad was achieved for FGSS-CIP at 9% drift ratio, prior to the sudden strength reduction which was because of rebar fracture. **Figure 4-59** shows the moment-plastic rotation plot for this test specimen.

#### 4.3.4.3 Cumulative Energy Dissipation

The cumulative energy dissipation per drift ratio is presented in **Figure 4-60** which implies an acceptable performance in terms of energy dissipation capacity. This specimen dissipated more energy with an increase in drift ratios up to the 9% drift ratio after which there was a sudden reduction when the column longitudinal bars fractured. The cumulative hysteretic

energy was 276 in-kip, 1549 in-kip, and 4788 in-kip at the end of the 3%, 6%, and 10% drift ratio.

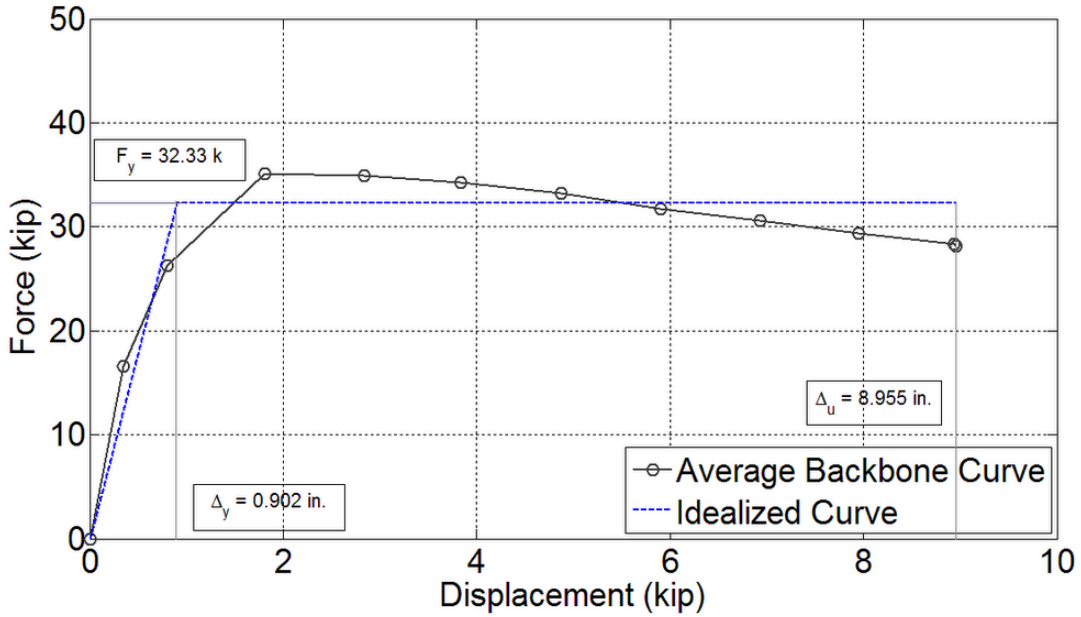


Figure 4-58. Average backbone curve and displacement ductility of FGSS-CIP.

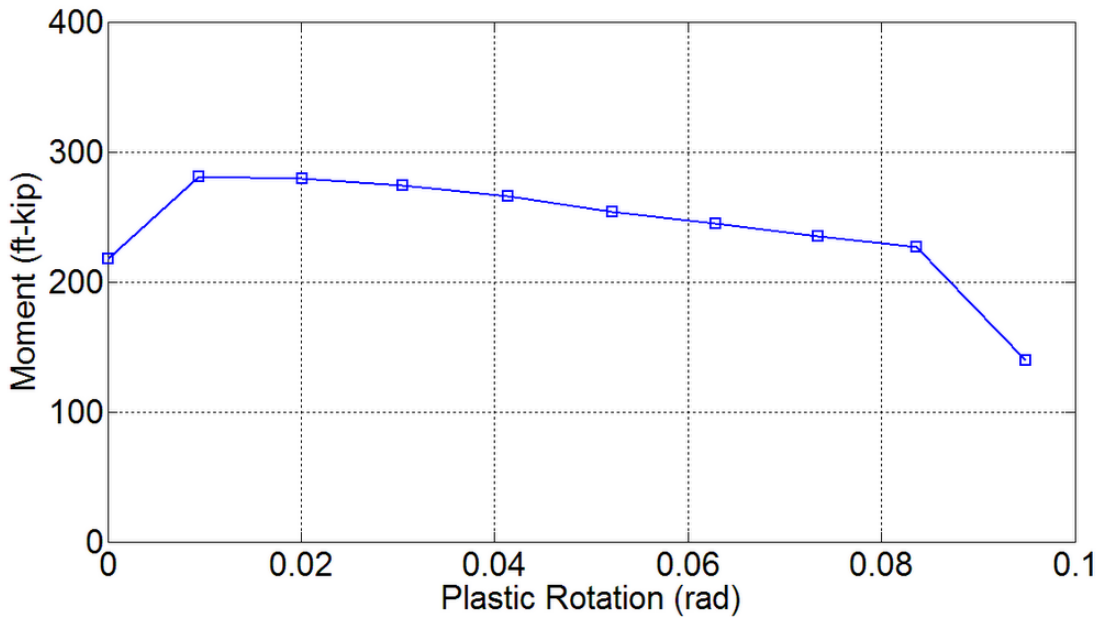


Figure 4-59. Plastic rotation capacity for FGSS-CIP.

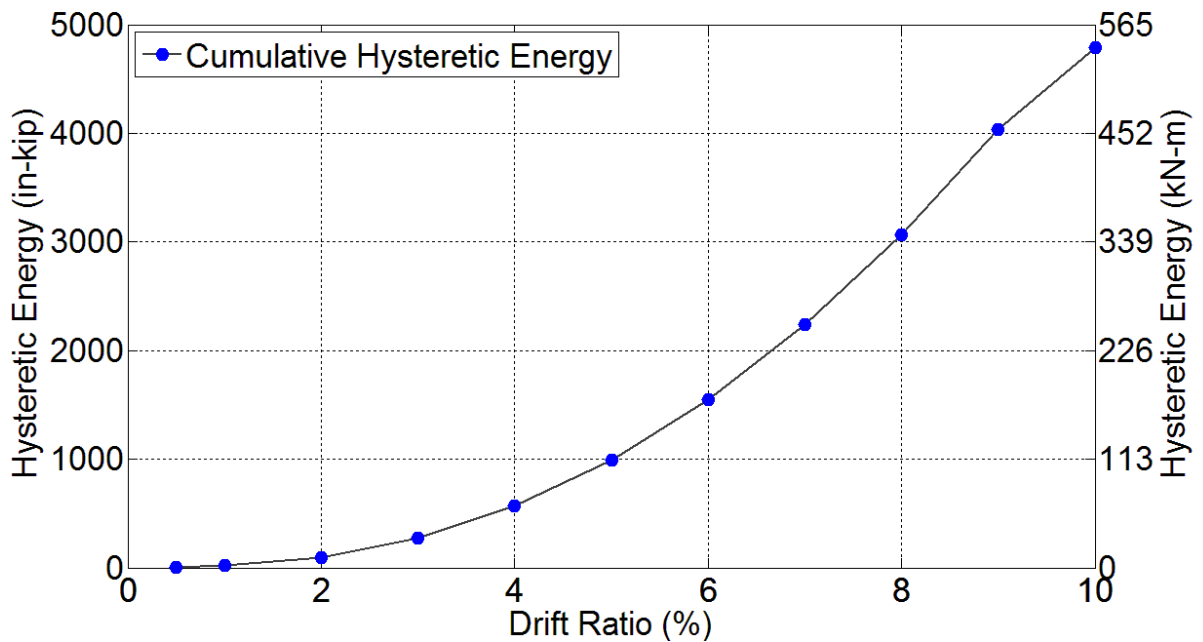


Figure 4-60. Energy dissipation capacity for FGSS-CIP.

#### 4.3.4.4 Column Curvature Profile

Specimen FGSS-CIP had a desirable curvature distribution along the column base. This was attributed to the well-detailed column plastic hinge region without the presence of the FGSS for splicing the dowel bars. The curvature demand increased towards the column end with an increase in the moment for a cantilever condition, as shown in **Figure 4-61**. This curvature profile was similar to the curvature profile for the FGSS-2 since the FGSS were inside the cap beam and, similar to FGSS-CIP, there were no sleeves inside the column.

Strain gauges located on the extreme longitudinal bars, in the column end and within the joint core, covered an area with a depth of 9 ½ in. into the cap beam and 38 in. up above the column end. These strain gauges showed that both extreme column bars yielded within this instrumented region.

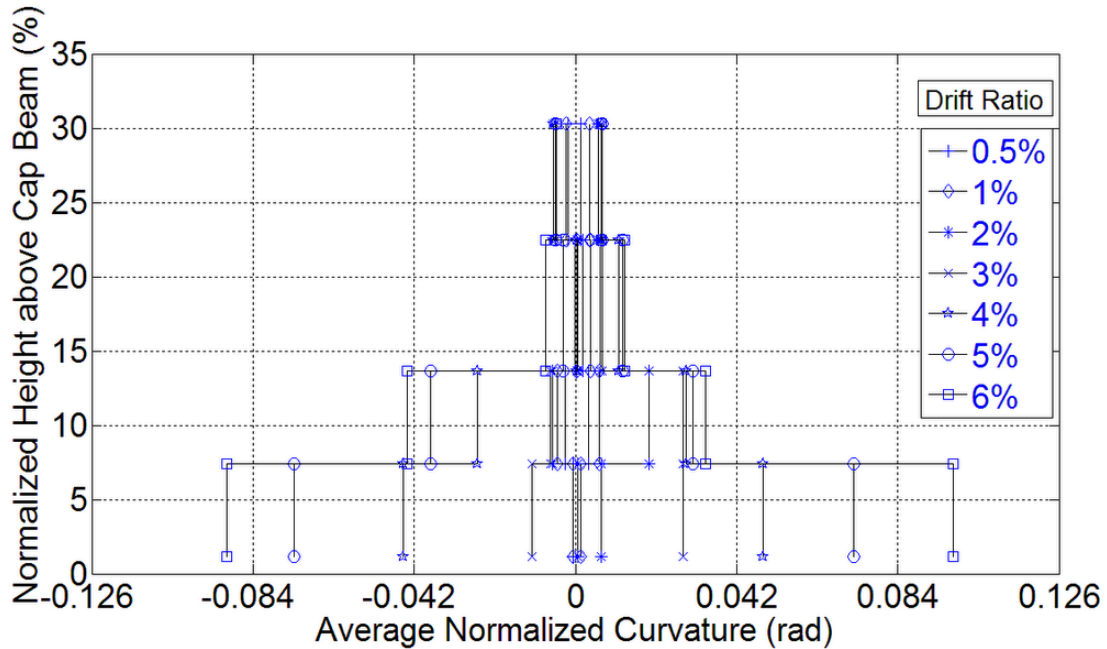


Figure 4-61. Normalized curvature distribution for FGSS-CIP.

#### 4.3.5 Comparative Study of Column-to-Cap Beam Connections

To compare the results from the experiments in this category of test specimens, it is essential to know the material properties for the rebar, concrete, and grout. Tension tests on reinforcing bars along with compression tests on concrete cylinders and grout cubes were performed for each test specimen. The results of tension tests on reinforcing bars for the column-to-cap beam specimens are presented in **Table 4-4**. It is observed that the cap beam dowel bars had different material properties than the column dowel bars, for the precast test alternatives.

**Table 4-5** contains the compression test results for the concrete and the grout utilized in the

Table 4-4. Rebar properties for column-to-cap beam test specimens.

Specimen	Column Rebar				Cap Beam Rebar			
	Longitudinal (NO. 8)		Transverse (NO. 4)		Dowel Bar (NO. 8)		Transverse (NO. 4)	
	Yield	Ultimate	Yield	Ultimate	Yield	Ultimate	Yield	Ultimate
FGSS-1	77	102	63	103	68	93	63	103
FGSS-2	68	93	63	103	77	102	63	103
FGSS-3	77	102	63	103	68	93	63	103
FGSS-CIP	68	93	63	103	68	93	63	103

Table 4-5. Concrete and grout properties for column-to-cap beam test specimens.

Specimen	Concrete		Grout	
	28-day	Test day	28-day	Test day
FGSS-1	5.3	6.2	12.5	13.3
FGSS-2	3.9	5.2	10.3	10.3
FGSS-3	6.7	8.2	10.6	11.7
FGSS-CIP	5.2	6.7	NA	NA

construction of the column-to-cap beam test specimens.

#### 4.3.5.1 Force-Displacement Response

In the previous sections, the ductility capacity of each test specimen was obtained based upon the hysteretic response to the simulated seismic loads. The displacement ductility capacity of all specimens in this category is shown in **Table 4-6**, in addition to the parameters used to perform the calculations. It is noted that FGSS-1 had a displacement ductility capacity of 4.9, FGSS-2 had an improved displacement ductility value of 5.8, and the displacement ductility for FGSS-3 was only 3.1 due to the unintentional pre-test damage that was introduced to this test specimen. It was anticipated to achieve an enhanced displacement ductility capacity for the FGSS-3 by providing the debonded rebar; however, this improvement would not have been drastically different than FGSS-1 as the cap beam dowel bars pulled out from the FGSS, i.e. no rebar fracture would have been achieved. The specimen FGSS-CIP had a displacement ductility of 9.9 which indicates a highly ductile response under the quasi-static loading protocol. The

Table 4-6. Effective yield properties and displacement ductility for column-to-cap beam test specimens.

Specimen	Last Drift Ratio (%)	$F_y$ (kip)	$\Delta_y$ (in.)	$\Delta_u$ (in.)	$K_{eff}$ (kip/in)	$\mu_\Delta$
FGSS-1	6	35.35	1.08	5.32	32.70	4.9
FGSS-2	7	33.29	1.11	6.50	29.92	5.8
FGSS-3	7	36.82	2.08	6.47	17.74	3.1*
FGSS-CIP	10	32.33	0.90	8.95	35.84	9.9

\*The value is unnaturally low due to testing error

displacement ductility capacities obtained for all precast test specimens exceeded the minimum displacement ductility capacity of 3 for ductile components as specified in Caltrans Seismic Design Criteria (SDC) [17]. According to the AASHTO-Seismic provisions, the local ductility demand for ductile members in high-seismic zones is limited to 5 and 6 for single-column bents and multiple-column bents, respectively [16].

The force-displacement response of the column-to-cap beam test specimens revealed a noticeable distinction between the precast FGSS specimens and the FGSS-CIP. The FGSS-CIP failed due to rebar fracture of the column longitudinal bars, as a result of low cycle fatigue; however, all precast test alternatives in this category failed because of the excessive bond-slip and consequent pull out of rebar. FGSS-2 was the only precast test specimen with one rebar fracture along with a subsequent rebar pull out for the opposite bar during the 7% drift ratio.

The backbone curve, or the so-called cyclic envelope, was constructed by joining the peak values of the first cycle for each drift ratio. **Figure 4-62** shows the cyclic envelopes for all column-to-cap beam test specimens. It is observed that the response of the FGSS-3 was affected in terms of lateral force capacity and initial stiffness; however, the overall force-displacement performance of all other test specimens is similar up to the 0.5% drift ratio. Specimens FGSS-1

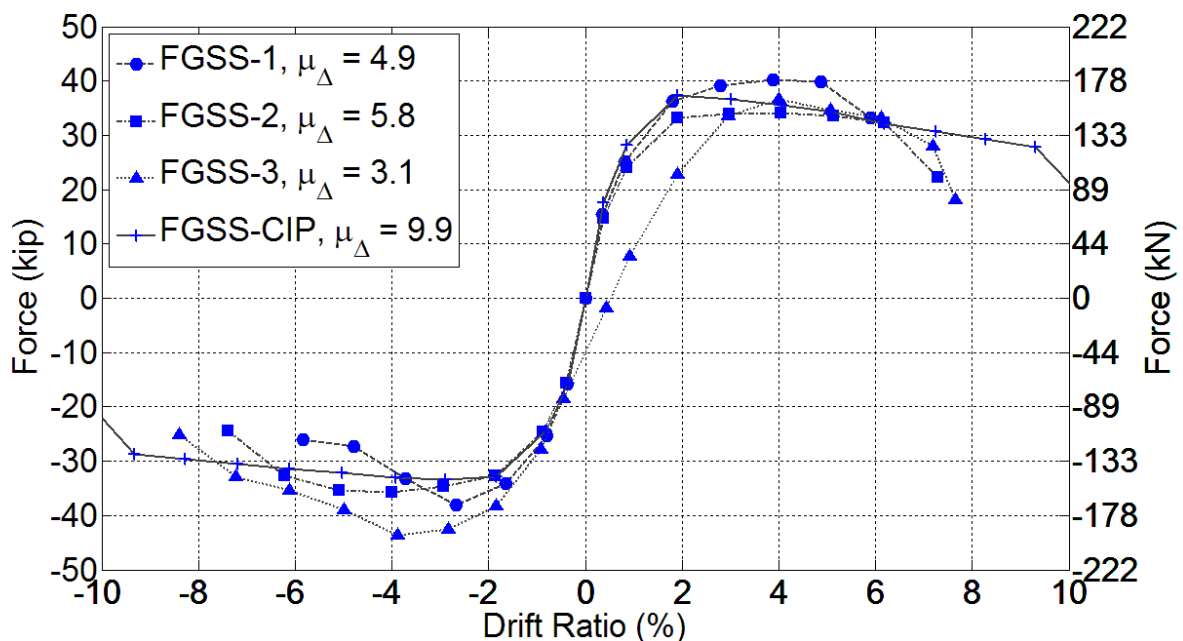


Figure 4-62. Force-displacement response of column-to-cap beam test specimens.

and FGSS-3 (even though FGSS-3 was pre-damaged) had the greatest strength capacities among all specimens. This was mainly attributed to the presence of the FGSS in the column base which led to a partial transition of the flexural action to the section right above the FGSS. However, a higher axial load was applied to FGSS-1 unintentionally which resulted in a larger lateral force capacity for this test specimen. This axial load was 40% larger than the axial load applied to FGSS-3, including the different concrete compressive strengths used for the two specimens. The lateral force capacity of FGSS-1 was 11% greater than that of the FGSS-CIP, including the effect of both a higher axial load along with the presence of the FGSS in the column base.

#### 4.3.5.2 Stiffness Degradation

The effective stiffness was calculated in each cycle using the peak displacement values and corresponding forces. The average of the stiffness values was then obtained for both cycles at each drift ratio. **Figure 4-63** displays the average effective stiffness at each drift ratio for all specimens. A similar trend was noted in the stiffness reduction per drift ratio for all specimens, except for FGSS-3. The initial stiffness of FGSS-3 was considerably reduced because of the pre-existing condition; however, the stiffness deterioration of this specimen became very similar to all other test specimens starting at the 2% drift ratio. The stiffness degradation graph indicates

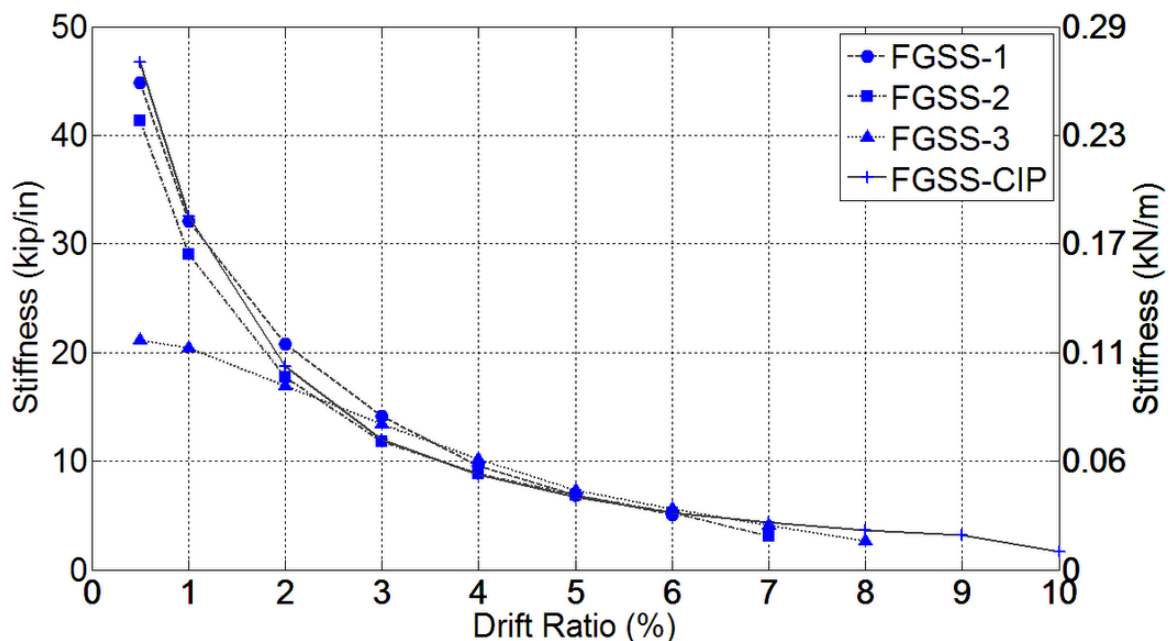


Figure 4-63. Stiffness degradation for column-to-cap beam test specimens.

that the precast test specimens had similar average component stiffness characteristics, and suggests that using the FGSS connectors in the column base or cap beam did not change the overall stiffness degradation rate.

#### 4.3.5.3 Energy Dissipation Capacity

The cumulative hysteretic energy capacity for all column-to-cap beam test specimens is shown in **Figure 4-64**. As observed, the rate of this quantity which is directly associated with the area under the hysteretic loops increases with an increase in the drift ratio up to the failure drift ratio, for all test specimens. **Figure 4-64** shows that all four test specimens had a very similar hysteretic energy dissipation capacity up to the 3% drift ratio, after which FGSS-CIP and FGSS-2 had a slightly better performance. This implies that FGSS-2 which had the FGSS connectors inside the cap beam had wider and more stable hysteresis loops that compared well with the cast-in-place specimen, i.e. FGSS-CIP. The hysteretic energy capacity of FGSS-1 and FGSS-3 was similar up to failure, indicating similar bond-slip characteristics and the resulting lower energy dissipation that was associated with a pinched hysteretic response. **Figure 4-64** also shows the superior hysteretic energy capacity of the cast-in-place test specimen which performed very well up to the 10% drift ratio.

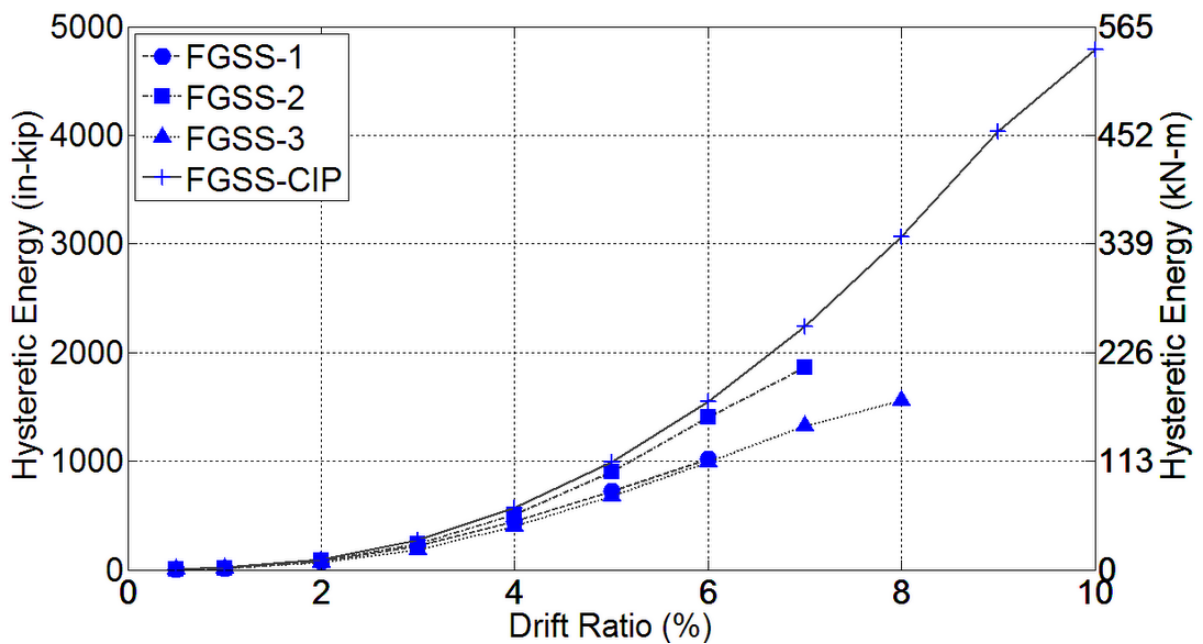


Figure 4-64. Cumulative hysteretic energy for column-to-cap beam test specimens.

The equivalent viscous damping ( $\xi_{eq}$ ) at each drift ratio was computed for each test specimen in this category as shown in **Section 4.2.5.3** for the column-to-footing test alternatives. **Figure 4-65** shows the  $\xi_{eq}$  variation during the test for each test specimen. The increasing trend of the  $\xi_{eq}$  is evident for all test alternatives which implies a better hysteretic performance with an increase in drift ratio. This graph suggests that FGSS-2 had the closest hysteretic performance to FGSS-CIP, and that FGSS-1 and FGSS-3 had a similar response. The FGSS-CIP specimen had a  $\xi_{eq}$  of 35% at the 10% drift ratio which is a desirable value for a ductile component. The equivalent viscous damping ratio at 6% drift ratio was 14%, 22%, 13%, and 24 % for the FGSS-1, FGSS-2, FGSS-3, and FGSS-CIP, respectively. This implies that the hysteretic response was improved when the FGSS was located inside the cap beam because of a reduced level of flexural demand over the FGSS region.

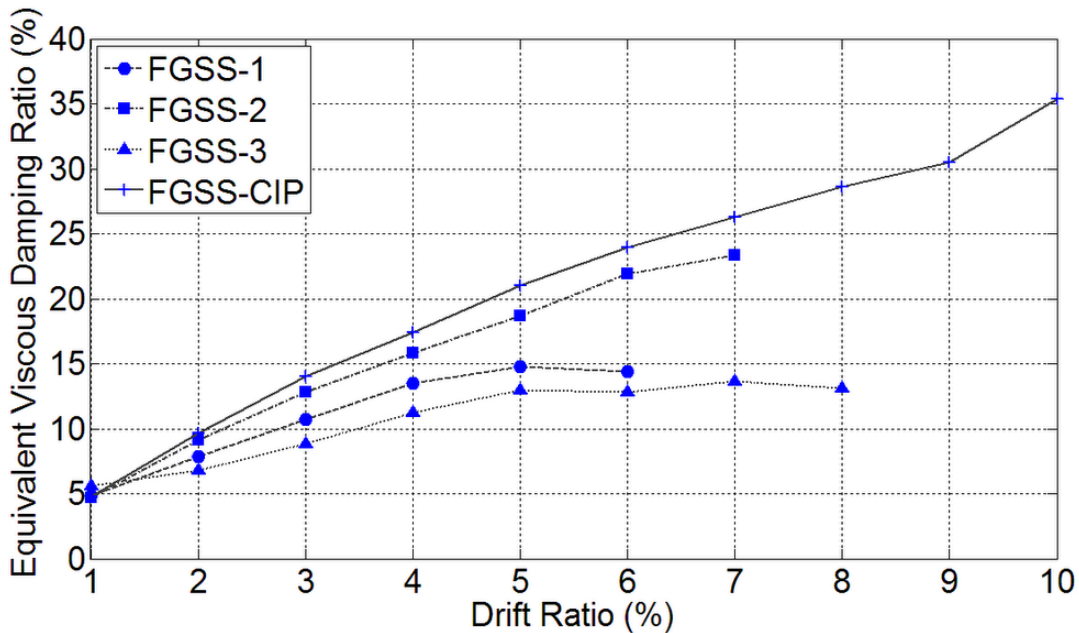


Figure 4-65. Equivalent viscous damping for column-to-cap beam test specimens.

## **5.0 CONCLUSIONS**

### **5.1 Summary**

The grouted splice sleeve connection was studied for Accelerated Bridge Construction in high-seismic regions. There is limited information on the true performance of such a connection type under simulated seismic loads, even though there have been a few experimental research studies evaluating the grouted splice sleeve connections in terms of strength properties or hysteretic performance. The research program described in this report was geared to ascertain the overall performance of two proprietary grouted splice sleeves available to be implemented in actual bridge construction. This report has presented the design, construction, test procedure, and experimental results of two categories of splice sleeve connectors using half-scale test specimens. Category-I test specimens were half-scale models corresponding to column-to-footing connections, in which a grouted splice sleeve called GGSS was incorporated to splice the vertical reinforcing bars. Both dowel bars were grouted inside the GGSS when connecting the precast column to the precast footing. Category-II test specimens were half-scale models of column-to-cap beam connections, in which a grouted splice sleeve called FGSS was utilized to complete the connection. One rebar was fastened to the threaded end of this type of grouted splice sleeve, whereas the other rebar was grouted inside the opposite side of the sleeve.

Three precast alternatives in addition to one conventional cast-in-place test model were constructed for each category of test specimens. The grouted splice sleeves were placed in the column base or column top in the first alternative. The location of the sleeves changed to the top of footing and bottom of cap beam to study the performance of the components when the sleeves were outside the plastic hinge zone of the column. The dowel bars in the footing and the cap beam were debonded over a length equal to eight times the rebar diameter ( $8d_b$ ) for the third precast test alternative in both categories; grouted splice sleeves were embedded in the column base for these two half-scale specimens, similar to the first test alternative. The last specimen type was the control component in which neither grouted splice sleeves nor even lap splices of the dowel bars were used. Continuous bars protruding out from the footing and cap beam were used to build the columns.

The performance of all test specimens was evaluated by analyzing the experimental results obtained from the instrumentation which was used to monitor the response under the quasi-static cyclic displacement history implemented in the tests.

Tests results indicated that all precast test specimens had a similar performance to the control specimens in terms of strength properties; however, the hysteretic performance, ductility capacity, and failure modes were found to be different. The research also demonstrated the necessary steps required to achieve an improved performance for the precast components. It was noted that a more ductile response could be achieved by placing the grouted splice sleeves in the footing or cap beam. On the other hand, a debonded rebar zone in the footing or cap beam enhanced the ductility capacity when the grouted splice sleeves were located in the column.

## **5.2 Findings**

The experimental data analysis provided both qualitative and quantitative measures to study the performance of each individual test specimen under quasi-static lateral cyclic loads. The summary of the findings from the experimental data analysis is presented separately for each category of test models, as follows.

### **5.2.1 Column-to-Footing Connections**

- 1) Cast-in-place specimen GGSS-CIP had a desirable ductile performance including a very good hysteretic response and ductile failure, i.e. rebar fracture on both opposite sides of the column. This test specimen had a displacement ductility of 8.9 and the hysteresis loops were wide and stable implying a good energy dissipation capacity.
- 2) Well-distributed flexural cracks formed along the column height of the GGSS-CIP, and the concrete cover spalled completely at the column base. The overall performance of the GGSS-CIP was dominated by flexural action and formation of a plastic hinge at the column base.
- 3) More localized damage was observed for the precast test specimens with the GGSS in the column base, i.e. GGSS-1 and GGSS-3. This involves fewer flexural cracks along the

column height compared to the case of the GGSS-CIP. The spalled region was also smaller than that of the GGSS-CIP as a result of the presence of the GGSS at the column base.

- 4) GGSS-2 had a damage state similar to the GGSS-CIP specimen, because there were no sleeves in the column base. Hence, more flexural cracks formed along the column, and the spalled regions in both specimens had a similar height, width, and depth.
- 5) GGSS-1 and GGSS-3 had a greater lateral force capacity than the GGSS-CIP specimen. This was mainly attributed to the presence of the GGSS in the column base which led to a partial transition of the flexural action to the section right above the GGSS. In addition, the cast-iron sleeves located in the column base of the GGSS-1 and GGSS-3 provided a compression reaction component at the interface which was believed to contribute to a higher lateral force capacity.
- 6) Rebar fracture occurred in all column-to-footing test alternatives which indicated that the tensile strength of the connection bars was developed when GGSS connectors were utilized to splice the dowel bars. The fracture of reinforcing bars in the GGSS-CIP specimen was due to low cycle fatigue. For all precast test specimens, rebar fracture occurred earlier than the GGSS-CIP specimen. This implies that a premature rebar fracture was present for all precast test specimens which was because of higher strains concentrated in the rebar at the interface of the column and footing.
- 7) A displacement ductility of 6.1 was achieved for specimen GGSS-2 in which the GGSS connectors were inside the footing. Compared to the case of specimen GGSS-1 with a displacement ductility of 5.4, a more ductile response was obtained by placing the GGSS connectors in the footing, along with a better hysteretic performance.
- 8) The eight bar diameter ( $8d_b$ ) debonded rebar zone for the footing dowel bars which was implemented for specimen GGSS-3 resulted in a displacement ductility equal to 6.8 which indicated a postponed rebar fracture condition because of a better strain distribution at the interface into the footing.

- 9) The distribution of inelasticity in the column base of specimen GGSS-2 was very similar to specimen GGSS-CIP, as there was no disruption of the natural stress transfer in the column base of GGSS-2. For the case of specimens GGSS-1 and GGSS-3, however, a different distribution of inelasticity was observed. This was attributed to the presence of the GGSS connectors in the column base in which the inelastic actions were shifted to locations at the bottom and top of the GGSS connectors.
- 10) Strain gauge data revealed that both dowel bars developed the yield strength of the rebar for specimens GGSS-1 and GGSS-3; however, the bottom dowel bar (factory dowel) did not yield for the case of specimen GGSS-2.
- 11) The displacement ductility obtained for all test alternatives exceeded the minimum component displacement ductility of 3 specified in the Caltrans SDC. In addition, the displacement ductility values were greater than the maximum displacement ductility of 5 which was specified in the AASHTO Seismic Guide for single-column bridge bents.

#### 5.2.2 Column-to-Cap Beam Connections

- 1) Cast-in-place specimen FGSS-CIP had a desirable ductile performance including a very good hysteretic response and a ductile failure, i.e. rebar fracture on both opposite sides of the column. This test specimen had a displacement ductility of 9.9 and the hysteresis loops were wide and stable implying a good energy dissipation capacity.
- 2) Well-distributed flexural cracks formed along the column height of specimen FGSS-CIP, and the concrete cover spalled completely at the column base. The overall performance of specimen FGSS-CIP was dominated by flexural action and formation of a plastic hinge at the column base.
- 3) More localized damage was observed for the precast test specimens with the FGSS connectors in the column end, i.e. FGSS-1 and FGSS-3. This involved fewer flexural cracks along the column height compared to the case of specimen FGSS-CIP. The spalled region was also smaller than that of specimen FGSS-CIP as a result of the presence of the FGSS connectors in the column.

- 4) Specimen FGSS-2 had a damage state similar to the cast-in-place specimen FGSS-CIP, because there were no sleeves in the column. Hence, more flexural cracks formed along the column, and the spalled regions in both specimens had a similar height, width, and depth.
- 5) Specimens FGSS-1 and FGSS-3 had a greater lateral force capacity than specimen FGSS-CIP. This was mainly attributed to the presence of the FGSS in the column which led to a partial transition of the flexural action to the section right above the FGSS. In addition, the cast-iron sleeves located in the column of specimens FGSS-1 and FGSS-3 provided a compression reaction component at the interface which was believed to contribute to a higher lateral force capacity.
- 6) Rebar fracture occurred in the cast-in-place specimen FGSS-CIP at a 10% drift ratio due to low cycle fatigue. A premature rebar fracture occurred in the west column bar of the FGSS-2 at a 7% drift ratio proceeded by the pull out failure of the opposite extreme bar. Specimens FGSS-1 and FGSS-3 failed because of rebar pull out due to an excessive bond-slip.
- 7) A displacement ductility of 5.8 was achieved for specimen FGSS-2 in which the FGSS connectors were inside the cap beam. Compared to the case of specimen FGSS-1 with a displacement ductility of 4.9, a more ductile response was obtained by placing the FGSS connectors in the cap beam, along with a better hysteretic performance.
- 8) The eight bar diameter ( $8d_b$ ) debonded rebar zone for the cap beam dowel bars which was implemented for specimen FGSS-3 was expected to result in a slightly postponed failure of the test specimen, although the maximum contribution of the debonded rebar would have been anticipated for the condition in which excessive bond-slip behavior is inhibited.
- 9) The distribution of inelasticity at the column end for specimen FGSS-2 was very similar to specimen FGSS-CIP, as there was no disruption of the natural stress transfer in the column end of FGSS-2. For the case of specimens FGSS-1 and FGSS-3, however, a different distribution of inelasticity was observed. This was attributed to the presence of the FGSS connectors in the column end in which the inelastic action was shifted to locations at the bottom and top of the FGSS connectors.

- 10) Strain gauge data revealed that both dowel bars developed the yield strength of the rebar for specimens FGSS-1 and FGSS-3; however, the bottom dowel bar (factory dowel) did not yield for the case of specimen FGSS-2.
- 11) The displacement ductility obtained for all test alternatives exceeded the minimum component displacement ductility of 3.0 specified in the Caltrans SDC even though specimen FGSS-3 had undergone a pre-test unintentional damage. In addition, the displacement ductility obtained for specimen FGSS-2 was greater than the maximum displacement ductility of 5.0 which was specified in the AASHTO Seismic Guide for single-column bridge bents.

### **5.3 Future Research**

- 1) More experimental research is needed to effectively assess the influence of changes in the debonded length of rebar used in the present research.
- 2) More experimental research studies are needed to study another test alternative in which the GGSS connectors are located inside the footing and a debonded rebar zone is incorporated in the column base.
- 3) Experimental research studies should be conducted to investigate the application of GGSS connections to splice high-strength reinforcing bars.
- 4) The application of the GGSS connection could be investigated in a hybrid setting. That is, mild steel is spliced by means of GGSS connectors while high-strength bars or tendons are utilized to achieve self-centering effects to reduce the residual drift and damage levels.

## **6.0 DESIGN RECOMMENDATIONS**

The design recommendations noted herein are based upon the observations made during the design, construction, and testing of the half-scale test alternatives described in the previous sections. The experimental data analysis demonstrated the strengths and weaknesses that existed in each test specimen. It is noted that the following design recommendations are only pertinent to flexural-dominant precast reinforced concrete components with similar aspect ratio. In addition, proper seismic detailing needs to be considered along with a well-confined plastic hinge region, as implemented for the half-scale test specimens in this research study. It is also of note that very few column bars were utilized in the construction of the half-scale columns which inflicted an extreme failure condition as a result of a pull out or rebar fracture of only one reinforcing bar. In actual construction a higher safety margin is usually considered by incorporating more column reinforcing bars distributed evenly over the column cross section. The design recommendations are as follows:

- 1) Transverse reinforcement should be utilized over the grouted splice sleeve region in such a way as to prevent the shifting of the sleeves in the column, footing, or the cap beam.
- 2) In case of using spirals with different diameter, one over the grouted splice sleeve and the other for the rest of the column, a splice length of two extra turns was found satisfactory.
- 3) The FGSS connectors were found to be promising for ABC applications in moderate-seismic regions if the reduced displacement ductility capacity is accounted for in the design.
- 4) An improvement to displacement ductility capacity is achievable by placing the FGSS connectors in the cap beam. This requires more effort during the construction phase to avoid spatial conflict.
- 5) The GGSS connectors were found to be viable for ABC applications in high-seismic regions if the reduced displacement ductility capacity is considered in the design.

- 6) An improvement to displacement ductility capacity is achievable by placing the GGSS connectors in the footing. This requires more effort during the construction phase to avoid spatial conflict.
- 7) A superior improvement to the displacement ductility capacity will be achieved when GGSS connectors are incorporated in the column base along with a debonded rebar region at top of the footing.

## REFERENCES

- [1] M. Tazarv and M. Saiidi, "Emulative Moment-Resistant RC Bridge Column-Footing Connection for Accelerated Bridge Construction in High Seismic Zone," in *Seventh National Seismic Conference on Bridges & Highways*, Oakland, 2013.
- [2] J. I. Restrepo, M. J. Tobolsky and E. E. Matsumoto, "Development of a Precast Bent Cap System for Seismic Regions," NCHRP Report 681, Washington, D.C., 2011.
- [3] M. L. Marsh, M. Wernly, B. E. Garrett, J. F. Stanton, M. O. Eberhard and M. D. Weinert, "Application of Accelerated Bridge Construction Connections in Moderate-to-High Seismic Regions," NCHRP Report 698, Washington, D.C., 2011.
- [4] B. Khaleghi, E. Schultz, S. Seguirant, L. Marsh, O. Haraldsson, M. Eberhard and J. Stanton, "Accelerated bridge construction in Washington State: From research to practice," *PCI Journal*, vol. 57, no. 4, 2012.
- [5] O. Haraldsson, M. J. Schoettler, G. Finnsson, P. M. Davis, J. Stanton and M. Eberhard, "Seismic Resistance of Precast Concrete Bridge Columns Made with Unbonded Pre-Tensioning and Hybrid Fiber Reinforced Concrete," *Seventh National Seismic Conference on Bridges & Highways*, Oakland, CA, 2013.
- [6] M. Tazarv and M. S. Saiidi, "NEXT GENERATION OF BRIDGE COLUMNS FOR ACCELERATED BRIDGE CONSTRUCTION IN HIGH SEISMIC ZONES," Center for Civil Engineering Earthquake Research, University of Nevada, Reno, 2014.
- [7] Z. B. Haber, M. S. Saiidi and D. H. Sanders, "Seismic Performance of Precast Columns with Mechanically Spliced Column-Footing Connections," *ACI Structural Journal*, vol. 111, no. 3, 2014.
- [8] Z. B. Haber, M. S. Saiidi and D. H. Sanders, "PRECAST COLUMN-FOOTING CONNECTIONS FOR ACCELERATED BRIDGE CONSTRUCTION IN SEISMIC ZONES," Center for Civil Engineering Earthquake Research, Department of Civil and Environmental Engineering, University of Nevada, Reno, 2013.
- [9] P. O. Jansson, "Evaluation of Grout-Filled Mechanical Splices for Precast Concrete Construction," Michigan Department of Transportation, Lansing, MI, 2008.

- [10] American Association of State Highway and Transportation Officials (AASHTO), "AASHTO LRFD Bridge Design Specifications," Washington, D.C., 2012.
- [11] ACI-ASCE Committee 550, Guide to Emulating Cast-in-Place Detailing for Seismic Design of Precast Concrete Structures, Farmington Hills, MI: American Concrete Institute, 2009, p. 17.
- [12] H. Aida, Y. Tanimura, T. Tadokoro and K. Takimoto, "Cyclic Loading Experiment of Precast Columns of Railway Rigid-Frame Viaduct Installed with NMB Splice Sleeves," in *Proceedings of the Japan Concrete Institute*, 2005.
- [13] T. Yoshino, K. Kobayashi and M. Ase, "Intensive Shear Reinforcing Method for PCA Members with Splice Sleeve Joint," Eleventh World Conference on Earthquake Engineering, Acapulco, Mexico, 1996.
- [14] Splice Sleeve Japan, LTD, "Tests on Re-Bar Splices in Reinforced Concrete Columns Using NMB Splice Sleeves," NPD-024.
- [15] Y. Matsuzaki and et al., "Effects of Sleeves on Member Properties, Study on the Behavior of Reinforced Concrete Beams with Grout-Filled Steel Splice Sleeves," Architectural Institute of Japan, 1987.
- [16] American Association of State Highway and Transportation Officials (AASHTO), AASHTO Guide Specifications for LRFD Seismic Bridge Design, Washington D.C.: AASHTO, 2011.
- [17] California Department of Transportation, Seismic Design Criteria, CA: Division of Engineering Services, 2010.
- [18] ASTM Standard C39, Standard Test Method for Compressive Strength of Cylindrical Concrete Specimens, West Conshohocken, PA: ASTM International, 2012.
- [19] ASTM Standard C109, Standard Test Method for Compressive Strength of Hydraulic Cement Mortars (Using 2-in. or [50-mm] Cube Specimens), West Conshohocken, PA: ASTM International, 2012.
- [20] ACI Committee 374, Guide for Testing Reinforced Concrete Structural Elements Under Slowly Applied Simulated Seismic Loads, Farmington Hills, MI: American Concrete Institute, 2013.

- [21] R. Park, "Evaluation of Ductility of Structures and Structural Assemblages from Laboratory Testing," *Bulletin of the New Zealand National Society for Earthquake Engineering*, vol. 22, no. 3, pp. 155-166, 1989.
- [22] M. Priestley and R. Park, "Strength and Ductility of Concrete Bridge Columns Under Seismic Loading," *ACI Structural Journal*, vol. 84, no. 1, pp. 61-76, 1987.
- [23] A. K. Chopra, *Dynamics of Structures, Theory and Applications to Earthquake Engineering*, NJ: Pearson Prentice Hall, 2007.